USING DEFECTS IN ANION EXCESS RHENIUM TRIOXIDE TYPE FLUORIDES TO CONTROL THERMAL EXPANSION; YTTERBIUM ZIRCONIUM FLUORIDE AS A CASE STUDY

A Dissertation
Presented to
The Academic Faculty

by

John Owen Ticknor

In Partial Fulfillment
of the Requirements for the Degree
Bachelor of Science (Research Option) in the
School of Chemistry and Biochemistry

Georgia Institute of Technology
May 2017

USING DEFECTS IN ANION EXCESS RHENIUM TRIOXIDE TYPE FLUORIDES TO CONTROL THERMAL EXPANSION; YTTERBIUM ZIRCONIUM FLUORIDE AS A CASE STUDY

Approved by:

Professor Angus P. Wilkinson, Advisor
School of Chemistry and Biochemistry
Georgia Institute of Technology

Professor Z. John Zhang
School of Chemistry and Biochemistry
Georgia Institute of Technology

Date Approved: May 5, 2017

ACKNOWLEDGEMENTS

This thesis describes the results of a two year endeavor (2015 – 2017) in undergraduate solid state chemistry research. More broadly, it represents the culmination of my four years at Georgia Tech as part of the School of Chemistry and Biochemistry. As I reflect on the time that has passed, I could not have asked for a more educationally enriching experience. Words cannot describe the respect and admiration I have gained for my institution and department. This demands recognition of the individuals who have enabled this. Although similar sentiments have been reiterated ceaselessly in every published thesis, I must stress that the support of those accredited was truly valued in every way imaginable. Collectively, these individuals have positively influenced my path during these four years in ways neither they nor I may ever fully realize. For this, I declare to all of them my utmost gratitude.

If it were not for the incredible guidance of both my parents, Wendy Henning and Kirk Ticknor, I may have never pursued the sciences. I will always fondly recall them encouraging my curiosity at a young age in constructive ways. They were here for me at each and every point during my time at Georgia Tech. I will forever be grateful for their love and commitment towards my wellbeing. I must also extend appreciation to my stepfather, Kevin Henning, and stepmother, Cindy Ticknor. Whenever I am in their company, they are always interested in my pursuits. Their care and support has further complemented that from my biological parents. My brother, Bobby Ticknor, has provided a constant source of joy in my life. I will always treasure him as the best brother I could ever ask for. This gratitude extends to his wife, Brianna Ticknor, who was constantly

interested in what I was involved in at Georgia Tech. My extended family appears to grow year after year, and if I were to name them all, these acknowledgements would span many more pages. I would want them all to know that I sincerely hold dear their support.

For the last four years, Georgia Tech has offered me a character-building challenge. Throughout this time, I have been extremely fortunate to be surrounded by numerous caring friends. They have each assisted me in my journey in unique ways. It would be an understatement to say that I am thankful for the support of best friend, Jasper Davis. His long-term loyalty and friendship has constantly improved who I am. I am also grateful for my other best friend, Ryan Dickmann. In his company, there is never a dull moment thanks to his sense of humor and uplifting demeanor. I must also thank my best friend in Sweden, Nicole Mothander, for her consistent inspiration and motivation that has made me a better person over the years. I also immensely appreciate the support and friendship of Daniel Shaffer, Catherine Galloway, Parker Pitisci, Victoria Joh, and Rishav Bose. I would want them all to know that my four year experience was dramatically improved by each and every one of them.

Four years ago, I was finalizing my senior project under the direction of Dr. Rosa Williams of Columbus State University. I am grateful for her mentorship, as she provided me an initial glimpse of what modern scientific research involves. I also recognize the guidance and inspiration that I have gained from several outstanding professors at Georgia Tech. They include: Dr. Kimberly Schurmeier, Dr. Michael Evans, Dr. David Sherrill, Dr. Cameron Tyson, Dr. William Baron, Dr. Kenneth Brown, Dr. Malavika Shetty, and Dr. Justin Biddle. I was humbled by their outstanding dedication and

engagement with their students, such as myself. They make Georgia Tech a truly incredible institution of learning.

Three graduate students, in particular, were instrumental during my undergraduate research. Brett Hester served as my primary mentor, from beginning to end. I am extremely thankful for his commitment towards my success. Most of the essential skills that I gained were a consequence of Brett's mentorship. He was also crucial towards collecting a large portion of the data presented in this work. I additionally credit Samuel Baxter for his efforts in obtaining density measurements, as well as the helpful laboratory assistance of Anthony Lloyd.

I am grateful for Dr. Z. John Zhang for serving as my secondary thesis committee member. Finally, I must acknowledge my undergraduate research mentor, Dr. Angus Wilkinson. Throughout the last two years, I have gained enormous respect for his dedication as a research faculty member. I will never cease to be impressed by his knowledge and expertise. Four years ago, I likely could not have imagined myself becoming so engaged with this branch of chemistry. Through his mentorship, I have become fascinated by the discipline. I am extremely appreciative for his unwavering engagement and support in everything I have been involved with. The entirety of this work was made possible through his phenomenal efforts. I will forever be thankful for him improving my abilities as a scientist and for providing me a strong foundation for my future research career.

This work was additionally supported by the staff members of the Advanced Photon Source (17-BM) at Argonne National Laboratory, under proposal ID 46274. Funding for this work was provided by the National Science Foundation grant DMR-1607316.

TABLE OF CONTENTS

LIST OF TABLES

LIST OF FIGURES

LIST OF ABBREVIATIONS

CTE	Coefficient of Thermal Expansion
LCTE	Linear Coefficient of Thermal Expansion
VCTE	Volumetric Coefficient of Thermal Expansion
PTE	Positive Thermal Expansion
NTE	Negative Thermal Expansion
ZTE	Zero Thermal Expansion
XRD	X-Ray Diffraction
PXRD	Powder X-Ray Diffraction
SCXRD	Single Crystal X-Ray Diffraction
SXRD	Synchrotron X-Ray Diffraction
APS	Advanced Photon Source
ANKA	Angströmquelle Karlsruhe
GSAS	General Structure Analysis System
CIF	Crystallographic Information File
ICP-AES	Inductively Coupled Plasma Atomic Emission Spectroscopy
DAC	Diamond Anvil Cell
TGA	Thermogravimetric Analysis

SUMMARY

The vast majority of technologically and industrially relevant materials expand on heating. This behavior is referred to as positive thermal expansion. This is occasionally of concern, as it can introduce damaging thermal stresses and fractures. An anomalous collection of materials instead contract on heating, which is commonly referred to as negative thermal expansion. Abundant scientific pursuits have been dedicated towards the synthesis, characterization, and application of negative thermal expansion materials. There is also substantial interest in materials which maintain zero thermal expansion, as this can impart thermal shock resistance and possible use in precision optics. These can potentially be produced through composites of positively and negatively thermally expanding materials in appropriate proportion. Alternatively, thermal expansion may be deliberately controlled by altering a material's composition or structure.

Rhenium trioxide (ReO_3) related materials have shown an attractive range of low and negative thermal expansion behavior. Mechanistically, this has been attributed to the thermally induced coupled rocking of corner-sharing octahedra, such that the cation centers are shifted inwards. Several of these ReO_3-type materials have been extensively studied. These include NbO_2F, TaO_2F, ScF_3, $CaZrF_6$, $CaNbF_6$, and $MgZrF_6$. Fluoride-based materials have received significant attention. In part, this is due to their optical infrared transparency. Additionally, the highly ionic bonding in fluorides favors the cubic structure, which promotes negative thermal expansion. The exploitation of defects in the ReO_3-type structure as a means to control expansion behavior has remained largely unexplored. It has been proposed that for cubic $YbZrF_7$, a ReO_3-type material, the

presence of an additional fluoride anion may allow the polyhedra to transform from corner-sharing to edge-sharing. This may inhibit the thermally induced rocking of the polyhedra such that the negative thermal expansion would be reduced towards zero thermal expansion.

Cubic $YbZrF_7$ was synthesized by heating stoichiometric amounts of YbF_3 and ZrF_4 starting materials to 1000 °C, followed by a fast quench to 0 °C. Powder x-ray diffraction measurements enabled quantification of its expansion behavior in terms of a volumetric coefficient of thermal expansion. Near zero thermal expansion was noted close to room temperature following an initial heating to 500 K, while negative thermal expansion was observed below 300 K. The expansion of cubic $YbZrF_7$ also displayed a thermal history dependence. When the material is first heated above 300 K, it undergoes a local structural change likely associated with the migration of fluoride anions. This is revealed by a sharp decrease in lattice constant between 310 and 350 K. In composites, the constituent components are frequently subject to stresses. Thus, the behavior of cubic $YbZrF_7$ was also examined on compression. Two striking features were observed: an abrupt order to disorder transition at approximately 0.9 GPa and a pressure-induced softening below 0.9 GPa, although the latter phenomenon has been predicted to occur in ReO_3-type materials. The isothermal bulk modulus (at 300 K) was calculated to be ~ 55 GPa, which is in close alignment with bulk moduli of similar materials. Above 700 °C in dry nitrogen, cubic $YbZrF_7$ begins to decompose to form solid YbF_3 and sublimated ZrF_4. Thermogravimetric analysis and powder x-ray diffraction measurements have indicated that cubic $YbZrF_7$ can be handled in air for at least 24 hours. Above 300 °C, it readily exhibits hydrolysis in moist air.

CHAPTER 1

INTRODUCTION

1.1 Importance of Thermal Expansion

Thermal expansion constitutes a material's change in dimensions according to an increase or decrease in temperature. It is extremely important to note that the dimension involved can encompass linear, areal, or volumetric domains. Such events can occur in isolation or in conjunction with one another. For example, a substance's overall change in volume necessarily imparts change in both area and linear regimes. Conversely, linear transformation may not inherently correspond to the volumetric component. This may be noted in anisotropic expansion, where differing expansion rates occur for separate axes [1]. Thus, by only examining volume as a function of temperature, critical information regarding the system of interest may be overlooked. Thus, it is worth considering all aspects of expansion in a material. Although any state of matter can undergo thermal expansion, the solid state will primarily be focused on.

Thermal expansion has gained tremendous interdisciplinary scientific, technological, and industrial interest. A clear illustration of this stems from the investigation of thermal expansion in various steel types [2]. Industrial applications of steel for a wide range of temperatures may demand knowledge of the expansion behavior for steel alloys. This is abundantly evident in the case of continuously welded steel railway track, where expansion caused buckling presents a potentially costly challenge [3]. Preparatory efforts in civil engineering are frequently implemented to avoid detrimental effects of thermal

stress in bridges, to include the usage of counteracting expansion joints [4-5]. Other problems in materials engineering can commonly arise, such as thermal shock. This can take place when a temperature gradient is introduced which results in incongruent expansion for different segments of the material [6]. This can lead to material damage or failure, especially in ceramics [7]. If an entire material neither expands nor contracts over a selected temperature range, the concern of thermal shock may be circumvented.

There exists an immense variety of available applications in understanding and characterizing thermal expansion in materials, including areas of study that may not be commonly associated with traditional materials science and engineering. In nuclear engineering, reactor design can be enhanced by improving graphite's dimensional stability upon exposure to radiation. Over the years, graphite has been phased out as a material for nuclear reactor moderators, although there are still about 30 active uses globally [8]. Another area where effective control of thermal expansion is important is precision optics. Even relatively small degrees of expansion in optical materials can generate substantial effects in the intended operation of the device, such as alteration of refractive index [9]. Assembled mirrors within space telescopes cannot be readily modified by technicians and thus, rigorous attention towards their expansion behavior must be adhered to [10-11]. Within the framework of geology, measurements of thermal expansion for a wide range of various minerals has allowed for elucidation of the prominent driving mechanisms of thermal expansion [12-14]. In cryopreservation biology, thermal expansion of living systems has also been investigated, as in the case of blood vessels [15]. Comprehensive understanding of thermal expansion can enormously contribute towards future research and innovation.

1.2 General Physical Mechanisms of Thermal Expansion

The physical origin of thermal expansion in materials has been a profoundly studied topic. Description of the surrounding physics allows for a clearer picture of the underlying phenomena. For simplicity, the gas phase will initially be considered as various complications can arise in the solid state. This may best be supported by envisioning a well-known diatomic molecule where the bond thermally expands, such as hydrogen fluoride (HF). HF consists of hydrogen covalently bonded to fluorine (**Figure 1.1**) in a highly polar manner such that most of the electron density is localized around the fluorine atom [16].

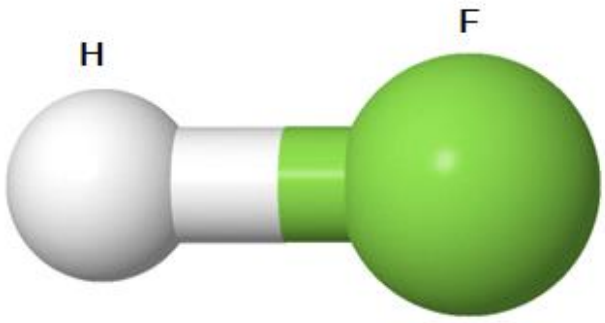

Figure 1.1: In hydrogen fluoride, a hydrogen atom is covalently bonded to the larger fluorine atom (model generated by JMol) [17]

When a bond between hydrogen and fluorine forms, the atoms involved will tend to move to an interatomic separation distance of the lowest possible energy state. This is deemed the ideal bond-distance or equilibrium bond length [18]. Suppose these atoms are forced closer to one another. The potential energy of the system will increase as their

electron cloud repulsion begins to dominate and oppose this motion. In contrast, if the atoms are brought further away from each other, their potential energy will again increase as their electrostatic attraction decreases. At a certain point, the bond will break. An anharmonic oscillator model can aptly illustrate the energetics of this situation, in which the individual atoms can be thought of as balls connected by a spring that does not perfectly obey Hooke's law. The Morse potential-energy curve (**Figure 1.2**) exhibits this [19].

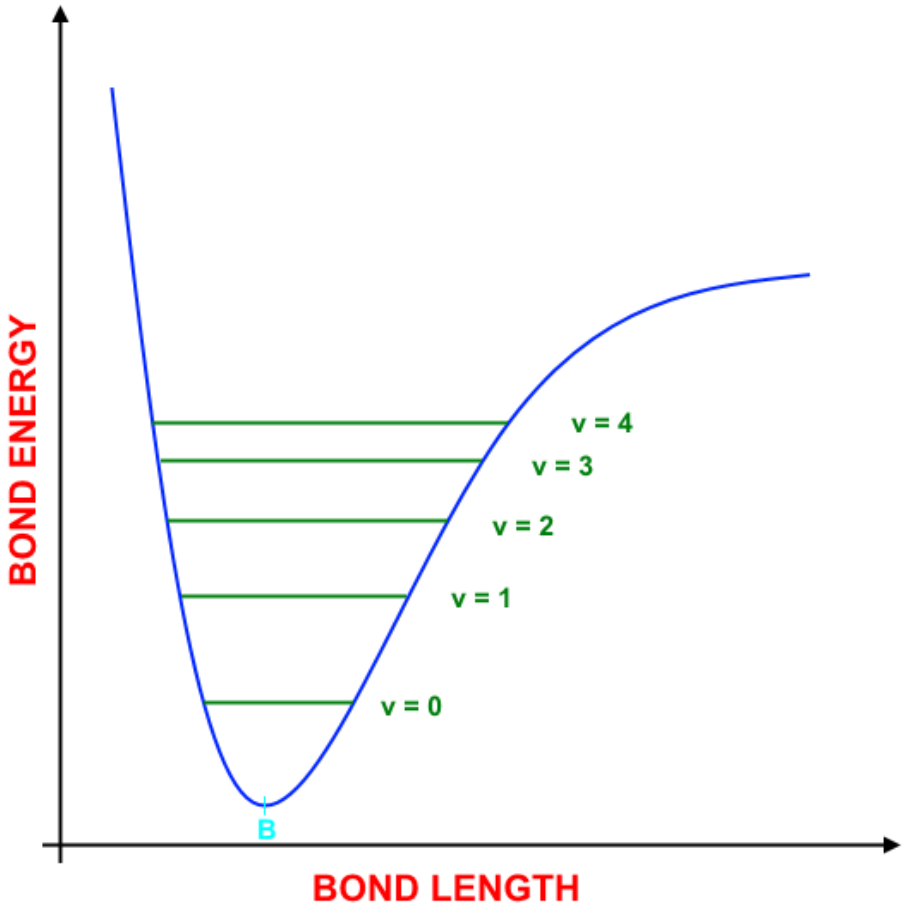

Figure 1.2: In a typical Morse potential energy curve, the molecule's equilibrium bond length is increased above the zero point bond length (B) when the molecule is at higher vibrational levels. The vibrational levels approaching v_{max} are not shown.

In addition to translational and rotational motion that an HF gas molecule can readily engage in, constant vibrational motion occurs along the bond axis. Population of higher energy vibrational states (v) is promoted by a temperature increase. At higher energy vibrational states, the range of possible interatomic distances is expanded. The asymmetric profile of the potential curve allows for this, although to a greater extent than for a harmonic oscillator [20]. The most important consequence of this is the increased average bond distance when in higher energy vibrational states, which underlies the expansion of the molecule. Thus, by increasing the temperature, the molecule expands in length. In strongly bonded systems, only the region of the potential energy curve that is approximately harmonic can be accessed so thermal expansion is small. If these were the only mechanisms responsible for thermal expansion, all materials might be expected to expand as the temperature is increased. As it happens, this is not the sole factor that influences how a material expands or contracts in response to a temperature change. Complications and exceptions will be discussed in **Section 1.4**, especially in relation to the solid state.

1.3 Quantification and Measurement of Thermal Expansion

Thermal expansion can be quantified in several different ways. One of the most relevant avenues involves the coefficient of thermal expansion (CTE), which applies for constant pressure conditions. Equations that calculate the CTE are adopted for linear, areal, and volumetric expansion. These are listed below, respectively in **Equations 1.1 – 1.3**.

$$\alpha_L = \frac{1}{L}\left(\frac{\partial L}{\partial T}\right)_P \approx \frac{L - L_0}{L(T - T_0)} \qquad \mathbf{1.1}$$

$$\alpha_A = \frac{1}{A}\left(\frac{\partial A}{\partial T}\right)_P \approx \frac{A - A_0}{A(T - T_0)} \qquad \mathbf{1.2}$$

$$\alpha_V = \frac{1}{V}\left(\frac{\partial V}{\partial T}\right)_P \approx \frac{V - V_0}{V(T - T_0)} \qquad \mathbf{1.3}$$

The terms above are denoted by the coefficients of linear (α_L), areal (α_A), and volumetric (α_V) thermal expansion. The exact form of each equation involves infinitesimal linear (∂L), areal (∂A), and volumetric (∂V) changes with respect to an infinitesimal change in temperature (∂T). In practice, these coefficients are often approximated by observing initial and final states for a selected temperature increment. This effectively allows for the CTE of a particular dimension to be estimated for a particular temperature [1,21-22]. The CTE for a given material can also be calculated from first principles.

Unless otherwise noted, the linear coefficient of thermal expansion will be referred to as LCTE (α_L) while the volumetric coefficient of thermal expansion will be abbreviated as VCTE (α_V). Areal expansion coefficients will not be emphasized, as the other two metrics are more useful for the purposes of this investigation. Materials can display a wide variation of CTE values, even in an ambient environment. Several substances and their estimated CTE values (atmospheric pressure) are shown in **Table 1.1**.

Table 1.1: Selected Solid-State Materials and Their Approximate Expansion Coefficients

Material	Temperature(s) (K)	Average α_L (ppm K^{-1})	α_V (ppm K^{-1})	Reference
Al	298	23.1	---	[23]
Cu	298	16.5	---	[23]
Fe	298	11.8	---	[23]
Ti	298	8.6	---	[23]
Si	300	2.526	---	[23]
WC (a-axis)	293	5.2	---	[24]
WC (c-axis)	293	7.3	---	[24]
PVC	298	80	---	[25]
H_2O	250	---	- 0.0006	[26]
NaCl	300	39.86	---	[27]
$Y_2Mo_3O_{12}$	298 – 1073	- 9.36	---	[28]
α-ZrW_2O_8	0.3 – 448	- 9.1	---	[29]
β-ZrW_2O_8	450 – 1050	- 5.0	---	[29]

There are numerous possible approaches that allow experimental measurement of thermal expansion. The technique of dilatometry has often been applied, which involves a macroscopic measurement of a material's expansion behavior. In general, the material of interest is heated or cooled in a controlled manner. A precisely monitored change in the overall specified dimension can be identified by several different methods. In a simple liquid-based volume dilatometry setup, a capillary tube is filled with solid sample of known mass. Calibrated volume changes can be determined when the sample expands or contracts within a non-volatile confining liquid, which is often mercury. By examining the height change of mercury within the capillary and through a series of subsequent calculations, sample volume change as a function of applied temperature can ultimately be acquired [30]. In push-rod dilatometers, a sample is constrained in a fixed volume by what is known as a push rod. Relative displacement of the rod upon temperature change can be accurately measured as the sample expands to force the rod outward [31]. Modern optical techniques can also be exploited for dilatometry. In one case, a Michelson-Type interferometer was adapted to directly detect temperature dependent expansion from an interference pattern, which was formed by the recombination of beam paths reflected from two separate samples [32]. In another example, charge-coupled device cameras have produced highly resolved and reproducible data representative of changes in sample length of the order of 1 μm [33]. Additional advantages to optical dilatometry include high temperature capabilities.

Dilatometry analyzes thermal expansion on a macroscopic level, although this alone may not fully describe a material's expansion, due to internal inhomogenities [34]. This can be overcome by x-ray and neutron diffraction experiments, as these permit microscopic-

level measurement of thermal expansion for crystalline materials. X-ray diffraction will be discussed in-depth in **Section 1.9**.

1.4 Negative Thermal Expansion and Low Thermal Expansion

The vast majority of common materials, including silicon, iron, aluminum, titanium, sodium chloride, silica, steel, and polystyrene, expand in response to a temperature increase, a condition known as positive thermal expansion (PTE) [2,23,35-37]. A thought provoking question arises as to why an anomalous collection of materials would contract upon heating instead, as this may seem contradictory to what was presented in **Section 1.2**. This phenomenon is labeled negative thermal expansion (NTE). This is an extremely well-documented and explored area of scientific research. During the past 20 years, there has been an increase in efforts towards synthesizing and characterizing materials which sustain NTE behavior [29]. Some examples of materials which display NTE include $Y_2Mo_3O_{12}$, α-ZrW_2O_8, and β-ZrW_2O_8 (**Table 1.1**), although there are many others [38]. The possibility of using these materials in a broad range of applications has driven more fundamental interest. Additionally, there has been substantial improvement in endeavors that not only identify NTE materials, but also elucidate the underlying physical mechanisms.

Thermal expansion can also be thought of in terms of entropy. For PTE to occur, an increase in volume must lead to an increase in entropy. Conversely, NTE demands a decrease in entropy for an isothermal increase in volume [39]. This follows Maxwell's thermodynamic relation (**Equation 1.4**), as the compressibility factor (κ) is positive except in very specific cases [40].

$$\alpha_V = \kappa \left(\frac{\partial S}{\partial V} \right)_T \qquad \mathbf{1.4}$$

Extensive searches for NTE materials have highlighted their rarity. Three major classes of mechanism for NTE have been identified: flexible (structural) network, atomic radius contraction, and magnetovolume effect [41]. The first mechanism will be described in detail in **Section 1.5**, as it is the primary focus of this work. The essential criteria of an atomic radius contraction model involves thermally influenced electron transfer (also known as charge transfer), whereby an increase in temperature stimulates contraction of an electron donating atom and simultaneously expansion of the electron accepting atom. Overall, the magnitude of ion contraction must greatly exceed the degree of ion expansion in order for significant NTE to take place. Evidence of this mechanism has been demonstrated in both perovskite oxides and $Sm_{2.75}C_{60}$ [42-45]. The magnetovolume mechanism relies on the dependence of volume to magnetic moment amplitude. Essentially, the presence of ordered magnetic moments in a material tends to favor a greater volume [41,46-47]. This is displayed in the alloy Invar, which exhibits an extremely low thermal expansion coefficient below its Curie temperature. It has been proposed that this NTE or low thermal expansion is associated with magnetovolume coupling, where anharmonic expansion is overwhelmed by thermal activation of a ferromagnetic system of reduced volume [41,48].

NTE materials are heavily sought after due to their wide range of potential applications, not the least of which relates to appropriately combining NTE and PTE materials such that near zero thermal expansion (ZTE) can be achieved [49]. This would introduce dimensional stability, which has large consequences in addressing resistance to thermal

shock and precision optical considerations. The feature of tunable NTE enhances the feasibility of developing NTE-PTE composite materials [50]. This has been accomplished, albeit not to a large extent, by defect insertion and intentional adjustment of stoichiometry [51-53].

1.5 Expansion Characteristics of ReO_3 Type Solids

The rhenium trioxide (ReO_3) structure consists of corner sharing ReO_6 octahedra, as shown in **Figure 1.3** [54]. Under ambient conditions the material is cubic, but it is known to adopt other structures, particularly on compression [55]. Note the corner-sharing octahedral pattern of oxygen anions (in red), which gives rise to a cubic unit cell.

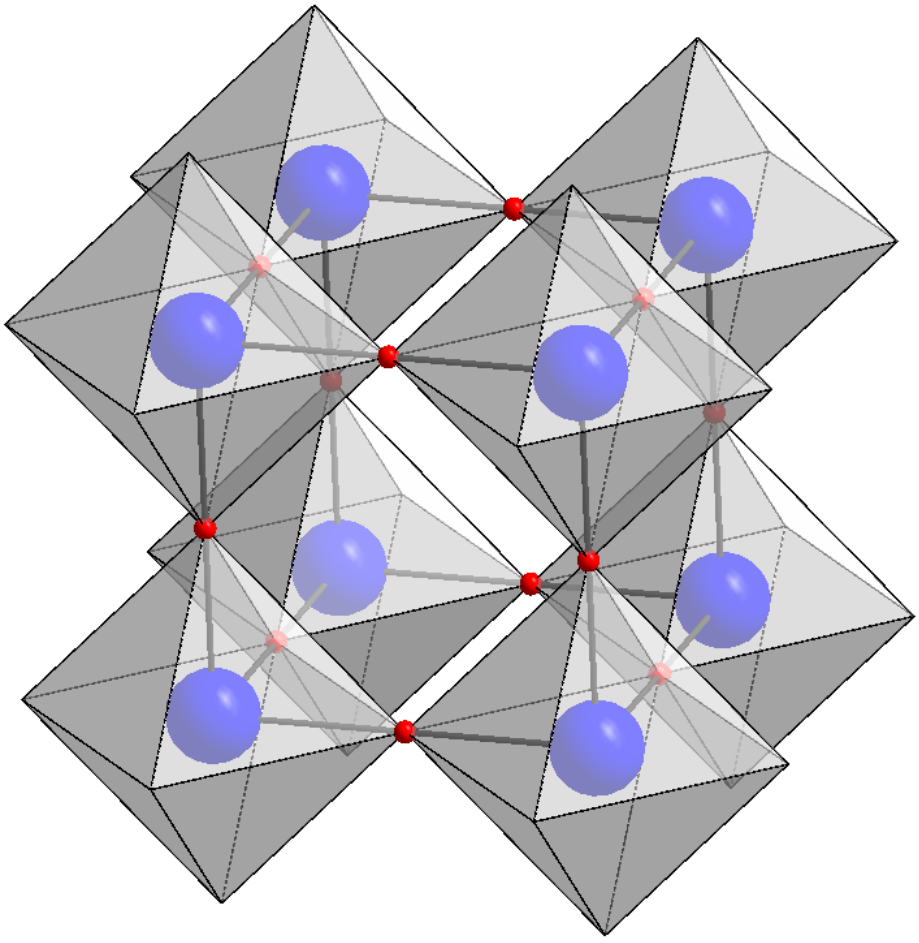

Figure 1.3: The general cubic (Pm – 3m) ReO_3 structure can be represented by eight corner-sharing octahedrons, colored in grey. The rhenium cations (shown in blue) are each bonded to six surrounding oxygen anions (shown in red), but note that not all of the oxygen anions are depicted. This graphic was generated by Diamond [56].

This ReO_3 structure is associated with a class of NTE mechanisms known as the flexible network designation. In this mechanism, the presence of extremely strong bonds impedes the expansion of bonds due to vibrational motion. This reduces the PTE as the thermally accessible region of the bonding potential energy curve (**Figure 1.2**) becomes less anharmonic. In order for NTE to occur, an increase in temperature must simultaneously reduce expansion of the unit cell and allow available interior void space to be filled [41]. In the case of the ReO_3-type structure, thermally induced coupled-rocking of corner sharing octahedra effectively force the cation centers inward. This results in an overall volume decrease, as shown in **Figure 1.4** [57]. Rigid unit mode vibrational motion characterizes this behavior, where the octahedra are allowed to move without distorting.

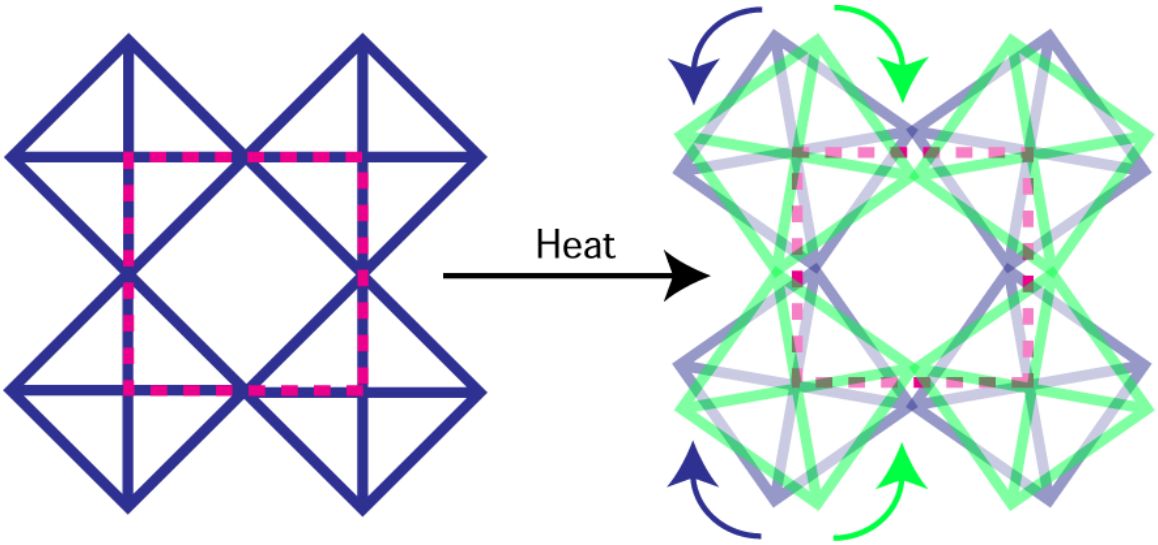

Figure 1.4: In the cubic ReO_3-type structure, the rigid unit mode vibrational motion of corner sharing octahedra allows the cations to be shifted inward on heating. Reprinted with permission from B. K. Greve et al. *J. Am. Chem. Soc.,* 132 (44):15496-15498, 2010. Copyright 2010, American Chemical Society [57].

A highly varied collection of materials have been documented to display NTE according to the flexible network mechanism, including (but not limited to) α-ZrW_2O_8, β-ZrW_2O_8, ZrV_2O_7, ZnF_2, $Cd(CN)_2$, $Zn(CN)_2$, $CaZrF_6$, $CaNbF_6$, ScF_3, and ReO_3 itself [29,57-62]. These materials and their expansion coefficients are listed in **Table 1.2**. Materials highlighted in red can adopt a cubic ReO_3-type structure.

Table 1.2: Assorted Flexible Network Negative Thermal Expansion Materials and Their Measured Expansion Coefficients

Material	α_L (ppm K^{-1})	α_V (ppm K^{-1})	Temperature (K)	Reference
α-ZrW_2O_8	- 9.1	---	0.3 – 448	[29]
β-ZrW_2O_8	- 5.0	---	450 – 1050	[29]
ZrV_2O_7	- 7 to - 10	---	375 – 1075	[29]
$Cd(CN)_2$	- 20.4	---	150 – 375	[27]
$Zn(CN)_2$	- 16.9	---	25 – 375	[27]
$CaZrF_6$	~ - 18	---	100	[61]
$CaNbF_6$	---	~ - 36	300	[62]
ScF_3	~ - 5	---	400	[57]
ReO_3	~ - 0.7	---	10 – 200	[58]

1.6 Defect Chemistry of ReO_3 Type Fluorides

The cubic ReO_3 structure consists of corner sharing octahedra, where the metal cations are located at the center of each octahedron and the anions (located at the corners of each octahedron) serve as links to adjacent octahedra. This holds true for all materials which adopt the cubic ReO_3-type structure, such as $CaZrF_6$, $CaNbF_6$, and ScF_3. For example, in $CaZrF_6$, the octahedra centers consist of alternating calcium and zirconium, each surrounded by six fluoride anions. This is such that cubic Fm – 3m space group symmetry is preserved, as shown in **Figure 1.5**.

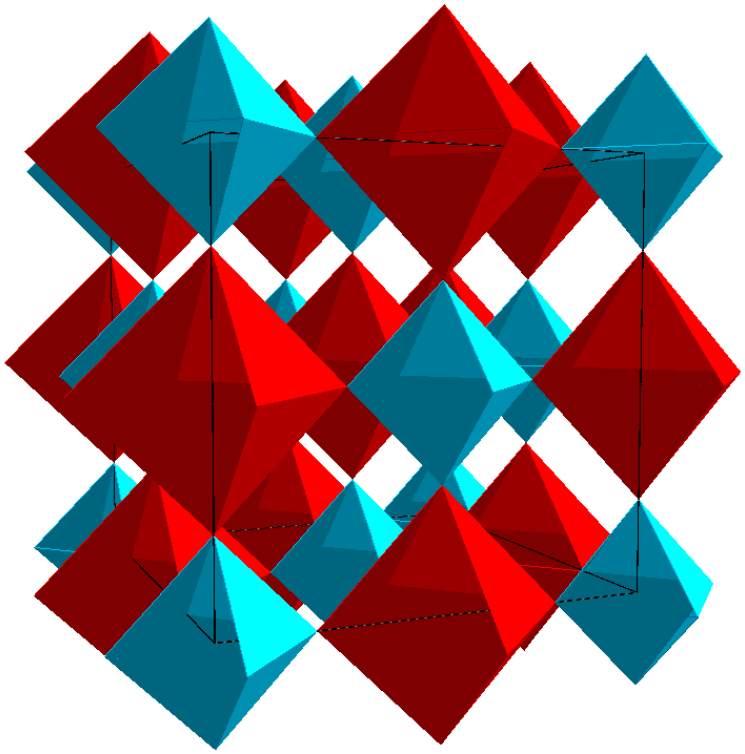

Figure 1.5: The cubic $CaZrF_6$ structure is represented by an ordered arrangement of calcium and zirconium cations, which are centered in the blue and red octahedra. These octahedra are linked at the corners by six fluoride anions, which are not shown. This graphic was generated by Diamond [56].

One may consider the insertion of crystallographic defects and how the ReO_3-type structure accommodates them. In addition, if the original material maintained NTE behavior, it may be worthwhile to better understand how the presence of these defects impacts said NTE. Ultimately, it may be desirable to take advantage of defects in order to control the thermal expansion of the material.

A wide variety of possible defects could be introduced into ReO_3-type fluoride structures. Fluorides are of particular interest due to their potential applicability in infrared transparent optics. In ScF_3, for example, the NTE behavior can be intentionally adjusted by the insertion of zirconium. What actually takes place is a removal of scandium cations (Sc^{3+}) in exchange for zirconium cations (Zr^{4+}), along with the appropriate amount of added fluoride anions (F^-) to preserve charge balance. The non-stoichiometric compound could therefore be represented by $Sc_{1-x}Zr_xF_{3+\delta}$. The process of incorporating different amounts of zirconium into ScF_3 effectively allowed for the tuning of its thermal expansion behavior. NTE could be gradually reduced in magnitude until near ZTE behavior arose for a specific scandium: zirconium ratio [63].

Anion disorder has also been recognized as a possible defect in ReO_3-type materials, as in the case of NbO_2F and TaO_2F [64-65]. The properties of NbO_2F have been reported to display a thermal history dependence; its expansion does not replicate on different heating and cooling processes. For instance, the observed CTE may be completely different on cooling as opposed to heating. Concurrently, TaO_2F has been shown to sustain near ZTE as opposed to NTE. These unexpected occurrences have been attributed to deviations of the local structure. The anion disorder effectively alters the bonding that exists in the idealized ReO_3 local structure. This can dramatically influence expansion

behavior. Hence, the local structure can potentially provide crucial insight regarding unusual expansion characteristics.

Insertion of excess anions as defects has also been considered for ReO_3-type fluorides, although it has not been extensively investigated in the context of thermal expansion studies. $PrZr_2F_{11}$ was identified to be structurally related to anion excess ReO_3-type materials (in relation to its β-ZrF_4 counterpart), where anion insertion transformed trigonal prismatic polyhedra to square antiprismatic polyhedra [66]. This curious notion of transforming polyhedra as a result of defect incorporation motivated further studies. A high pressure phase of zirconium tetrafluoride (γ-ZrF_4) was described as an anion-excess ReO_{3+x} type material. In this case, however, the polyhedra are linked by both corner and edge sharing components. By inserting an additional fluoride ion, the corner-sharing octahedra shift to a pentagonal bipyramidal geometry (**Figure 1.6**) in order to locally adjust to the additional anion. The metal to metal distances are also reduced [67]. Attention to how these structural changes may influence the thermal expansion in ReO_3-type fluorides is of interest.

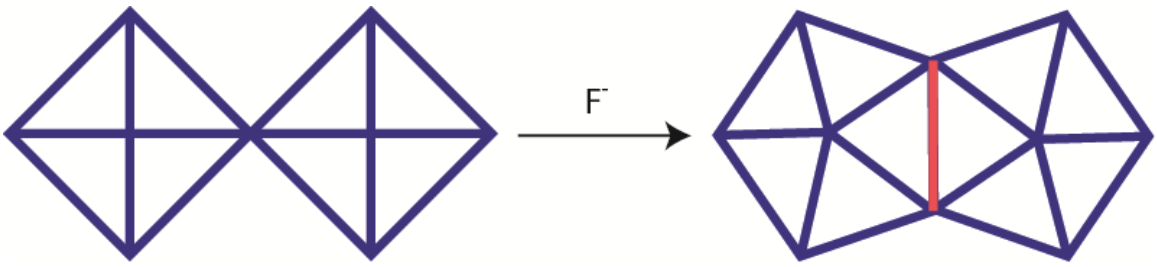

Figure 1.6: When an additional fluoride anion is inserted into corner-sharing polyhedra, it is proposed that these polyhedra are transformed to edge-sharing.

1.7 Review of $LnZrF_7$ Chemistry

One class of fluoride excess ReO_3 related materials is the lanthanide fluorozirconates of the form $LnZrF_7$. Fluorozirconates have long attracted attention due to their potential applicability in fiber optic technology, primarily as a consequence of their optimal physical properties such infrared transparency. It has been proposed that they can be utilized in an extremely wide range of different optical devices. This has ramifications towards improving the capabilities of telecommunication and information processing [68]. These efforts have also guided ultra-purification methods of starting materials in order to avoid the presence of optically absorbent particles in the final product [69].

$LnZrF_7$ (Ln = La, Ce, Pr, Nd, Sm, Eu, Gd, Tb, Dy, Ho, Er, Tm, Yb, and Lu) materials have previously been synthesized and characterized [70]. Their anion excess structure is often described as consisting of interstitial anions being inserted into available void space between the polyhedra. In $LnZrF_7$, 1:1 stoichiometry between LnF_3 and ZrF_4 is preserved. The thermodynamic product for $LnZrF_7$ has been reported to adopt a monoclinic space group $P2_{1/c}$, although other polymorphs have been identified [71]. For instance, cubic $YbZrF_7$ has previously been synthesized by a rapid quench from high temperature [72]. This approach has also produced cubic $LuZrF_7$ and $TmZrF_7$ [73]. Although the monoclinic form may not intuitively appear associated to the ReO_3-type structure, evidence has suggested otherwise. For $SmZrF_7$, it has been proposed that samarium cations are each coordinated to six fluoride anions while zirconium cations are coordinated to eight fluoride anions, where the polyhedra are corner-linked [74]. This appears reasonable, as zirconium can readily accommodate increased coordination of fluoride anions [75].

$YbZrF_7$ is of interest in terms of how the interstitial fluoride defects influence thermal expansion relative to other ReO_3-type fluorides. By converting corner-sharing octahedra to edge-sharing polyhedra, it is hypothesized that the coupled rocking of the polyhedra will be inhibited. Given that these structural motions are associated with NTE behavior of ReO_3-type fluorides, it is proposed that the NTE behavior could be controlled or reduced in magnitude such that ZTE could be achieved. Although any lanthanum fluoride which can adopt a cubic ReO_3 related structure could be selected for thermal expansion study, $YbZrF_7$ has been chosen primarily due to its ease of synthesis (**Section 1.8**) and available crystallographic data for the purposes of characterization described in **Section 1.9**.

1.8 High Temperature Solid State Synthetic Methods for Fluorides

Solid state inorganic fluorides can be synthesized by a variety of methods, each with their respective advantages and disadvantages. Procedural modifications can be performed in order to optimize the quality of the final product. A universal consideration involves avoiding undesirable production of hydrofluoric acid, as this can occur when either the reactants or products are exposed to moisture [76]. Oxide contamination must be avoided, especially for materials with optics applicability. As with most solid state syntheses, purification is either unrealistic or unmanageable. Aside from strict atmosphere control, other synthesis parameters can be quite flexible. It must be stressed that no single method will consistently be performed, as there are of course constraints on available equipment, personnel, time, and cost.

Perhaps the most encountered synthesis route involves the ceramic method [27,61-62,72]. In essentially every case, the common elements include thoroughly mixed and ground

high purity (> 99 %) reactants, relatively high reaction temperatures (300 – 1200 °C), and inert atmosphere (often N_2 or Ar) reaction conditions. It may be also be valuable to assess the purity of the starting materials through characterization techniques to be discussed in **Section 1.9**. Abundant modifications to the general outlined approach have proven viable, and some efforts have shown higher degrees of success than others. For example, pelletizing the reagents may reduce the ion diffusion barrier necessary for allowing the desired product to form. If pelletizing is neglected, the diffusion barrier may perhaps instead be overcome by increased synthesis temperature or duration. The choice of container often defers to both synthesis temperature (copper melts at 1085 °C whereas nickel melts at 1455 °C) and reactivity with starting materials [23]. Assuming the equipment is available, the ease of this technique is its primary advantage, although expensive reagent and operational costs may motivate alternatives.

Hydrothermal methods can provide a milder route to rare-earth fluorides. Sufficient amounts of ammonium fluoride (NH_4F) can be added to nitric acid (HNO_3) solutions containing a rare-earth oxide. The resulting mixture could then be transferred to a sealed vessel. It can then be heated for less duration and at lower temperature, although this could not circumvent the production of hydroxides [77]. This situation also appeared when NbO_2F was prepared by both aqueous (Nb_2O_5 added to HF and evaporated) and traditional solid state (NbF_5 combined with Nb_2O_5) syntheses, where differently synthesized products were reported to behave differently on cooling and heating based on the possible insertion of hydroxide when an aqueous synthesis was used [65]. In contrast, nanocrystalline syntheses have frequently seen success through hydrothermal techniques

[78]. Overall, they may lessen the amount of time required, although they are often unable to prevent impurities as intended.

Improved quality crystalline products (as in the case of AlF_3 and CrF_3) have also been made through the utilization of flux techniques, where the reactants are dissolved in a suitable solvent such as lead fluoride (PbF_2) or lead chloride ($PbCl_2$) [79]. Sol-gel methods have also been implemented to produce a variety of fluoride-based materials, and these have exhibited a high degree of versatility. For example, fluorolytic sol-gel synthesis has produced MF_3 doped MgF_2, which could gain utility in catalytic processes [80]. Much like the presented hydrothermal methods, limitations persist in the ability to eliminate water derived impurities in the products [81]. In one case, however, it was reported that $LiYF_4$ and $LiGdF_4$ could be produced by a sol-gel method under a strictly dry F_2 atmosphere. This effectively prevented the incorporation of hydroxyl or organic impurities [82]. In sum, there appears to be no single synthesis technique which guarantees the highest degree of success in the case of inorganic fluorides. The influencing factors must be weighed according to what is most desired for a given synthesis.

1.9 X-Ray Diffraction

Once a synthesis of a ReO_3-type fluoride has been performed, one must immediately consider how to appropriately identify and characterize the material. In sharp contrast to the broad range of possible synthetic techniques, the most fundamental information regarding the material's atomic structure can be obtain using x-ray or neutron diffraction.

Consider a situation where electrons are accelerated by an extremely large potential difference. When these electrons collide with a metal anode such as copper (Cu) or molybdenum (Mo), the innermost atomic electrons can be ejected from their orbitals. In response, the electron vacancy is immediately occupied by an electron of the next highest energy level, and then this vacancy propagates to higher energy levels. These electronic transitions generate intense radiation of specific energy in the x-ray range of the electromagnetic spectrum. After the discovery of x-ray radiation in 1895 by William Röntgen, it was gradually revealed that this phenomenon could be enormously useful [83-85].

When x-ray radiation interacts with a crystalline material, there are multiple different processes that can occur. This includes elastic scattering, which is responsible for diffraction in crystals. X-ray radiation is restricted to wavelengths between 0.01 Å and 100 Å – four orders of magnitude. This is a highly convenient range, as it spans the length scales associated with interatomic distances for the vast majority of solid state crystalline materials [86]. For example, in potassium bromide (an important material for infrared spectroscopy), the cubic unit cell is approximately 6.6 Å in edge-length [87]. This means that the K–Br interatomic distances are well within the boundaries of the x-

ray wavelength range. Monumental discoveries (lead by Max von Laue) during the early twentieth century concluded that crystalline materials essentially serve as diffraction gratings for x-ray radiation. This is directly linked to the periodic arrangement of atoms in crystalline materials [88].

Consider monochromatic x-ray radiation traveling towards a crystalline system of interest at relatively low temperatures, such that atomic motion is minimized. This system consists of scattering objects in a periodic arrangement, as shown in **Figure 1.7**. Most importantly, the x-ray photons have a wavelength (λ) that is comparable to this interatomic spacing. One beam of radiation (denoted A) is allowed to strike an object on the first accessible layer, while a secondary parallel beam (denoted B) must traverse further into the interior of the crystal until it interacts with an object immediately below the first object. These two particular objects are separated by a distance, d. When both of these beams (A and B) strike their respective objects, one possible consequence is scattering, as illustrated in **Figure 1.7** [84].

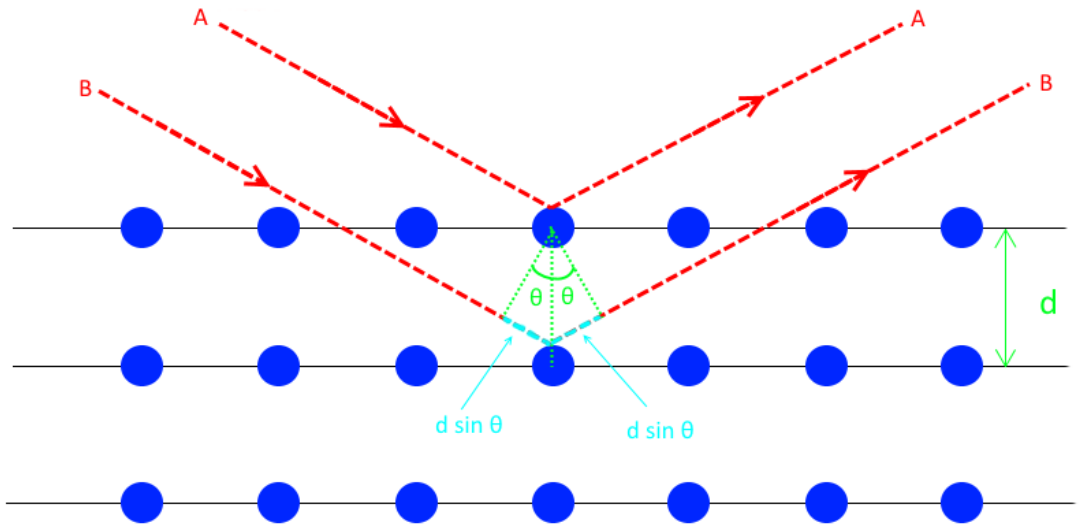

Figure 1.7: Bragg's law is visualized for a periodic arrangement of objects.

The criterion (also known as the Bragg condition) for scattering to be observed is that the rays S_A and S_B must constructively interfere with each other. This only occurs when the path lengths for the radiation differ by an integer multiple of the wavelength, nλ. It can be shown that the additional distance that the secondary beam (B) must traverse is equal to 2dsin(θ). Therefore, Bragg's Law (**Equation 1.5**) can be applied in this established scheme:

$$n\lambda = 2d\sin(\theta) \qquad \mathbf{1.5}$$

This is perhaps the most fundamental equation in x-ray crystallography. The equation can actually be written less formally as **Equation 1.6**. This is because the reflections of n = 1 and n = 2 cannot be discerned from each other [84].

$$\lambda = 2d\sin(\theta) \qquad \mathbf{1.6}$$

It is worthwhile to briefly describe in detail the precise meaning of the distance term in Bragg's Law, d. This actually corresponds to the distances between lattice planes responsible for a given Bragg reflection. These can be labeled with Miller indices, which are given as three integers: h, k, and l. This topic rapidly complicates, and thus explanation will apply purely for a cubic system. In a cubic unit cell, the largest possible d-spacing involves the (1, 0, 0) plane. This plane has a characteristic distance (d_{100}), where the unit cell lattice constants consist of a = b = c = d_{100} [84,89]. Other Miller indices can be formed, each with their unique d_{hkl} value. Note that if the wavelength of the monochromatic x-ray radiation remains constant, the only varying terms are d and θ. Mathematically, the largest value that can exist for d must stem from the lowest angle θ. Larger reflection angles correspond to smaller d values [84,90]. For an orthogonal unit cell, this unique d-spacing is formally expressed in **Equation 1.7**:

$$\frac{1}{d_{hkl}^2} = \frac{h^2}{a^2} + \frac{k^2}{b^2} + \frac{l^2}{c^2} \qquad \mathbf{1.7}$$

Upon detection of the scattered radiation which has fulfilled the Bragg condition, a series of peaks in diffraction intensity result which can ultimately be indexed to different Miller indices. By the application of **Equations 1.6** and **1.7**, unit cell constants (a, b, and c) can be extracted from the observed diffraction angle (θ) where the peak of intensity arises. Peak position (more commonly represented in terms of angle 2θ) is determined by the lattice. Peak intensities are related to atomic positions. The calculation of lattice constants based on peak position is most often computationally aided, especially for more complicated unit cells of (e.g. non-orthogonal) where **Equation 1.7** is no longer valid [84,91].

A plot of diffraction intensity as a function of scattered angle (2θ) represents a diffraction pattern. Each unique atomic arrangement of a crystalline solid (NaCl, KBr, Fe, BaO, ScF_3, $CaZrF_6$, etc.) generates a different x-ray diffraction pattern [62,92-96]. X-ray diffraction can thus be thought of as the "gold-standard" in characterization of crystalline materials. Over the course of nearly a century, an enormous database of different materials and their respective x-ray diffraction patterns has been developed. This information can be accessed through different sources, such as the Powder Diffraction File (PDF) of the International Center for Diffraction Data (ICDD) or the Inorganic Crystal Structure Database (ICSD) [97-99].

Experimentally, x-ray diffraction measurements can generally be performed using two different methods: powder or single crystal. In powder x-ray diffraction (PXRD), essentially every possible orientation of the crystal is accounted for, and thus the scattering occurs over an isotropic system. In single crystal x-ray diffraction (SCXRD), the scattering of only one crystallite is considered. Given that the single crystal is oriented in a specific manner, the measurement is said to be anisotropic. For both PXRD and SCXRD, the measuring instrument can only utilize a discrete set of wavelengths inherent to the anode material. Thus, these techniques are optimal for initial characterization of a material.

If more elaborate study of a material is desired, it may be appropriate to turn to synchrotron x-ray diffraction (SXRD). In SXRD, a continuous range of wavelengths is accessible, as the radiation no longer relies on a single anode source. Instead, x-ray radiation of high energy (and high intensity) is generated by accelerating electrons through the action of carefully placed magnetic devices. This radiation can be channeled

towards the crystalline system of interest. Synchrotron powder diffraction is often performed using area detectors, where an entire diffraction pattern is measured simultaneously. The conventional diffraction intensity versus 2θ pattern can be obtained by integration. Alternatively, diffraction intensity can be displayed as function of Q, as opposed to 2θ. This allows for a pattern to be represented independent of wavelength, as given in **Equation 1.8**.

$$Q = \frac{4\pi \sin(\theta)}{\lambda} \qquad \mathbf{1.8}$$

The advanced nature of synchrotron radiation usually entails extremely high construction and operation cost. This is why there are only a few facilities globally. Currently active sites include (but are not limited to) the Advanced Photon Source (APS) in the United States, MAX IV in Sweden, Angströmquelle Karlsruhe (ANKA) in Germany, and the European Synchrotron Radiation Facility in France [100-103].

The obtained diffraction data must be fit with a model in order to obtain meaningful structural information, such as lattice constants, atomic coordinates, atomic multiplicities, atomic occupancies, and atomic displacement parameters. The possibility of peak overlap, which arises commonly in powder diffraction, can often make this process quite difficult [84]. The Rietveld method of fitting is frequently applied to both conventional and synchrotron type x-ray diffraction data, although there are certainly other approaches [104-105]. A detailed view of Rietveld fitting and its complications extend beyond the scope of this thesis. Nonetheless, the fundamentals will be briefly discussed. Essentially, a linear combination of Gaussian and Lorentzian type functions are constructed and fit to

the diffraction pattern using a least squares refinement method. The generated fit maintains Gaussian and Lorentzian components of a specific ratio according to the shape of the diffraction peaks [106]. Despite limitations, it has been reported that this fitting technique serves reasonably well for fitting many diffraction patterns [107-108].

It is important to realize that changes in temperature can be reflected by alteration of a material's x-ray diffraction pattern. This is because a change in temperature can directly influence a material's structure. X-ray diffraction therefore provides a convenient method of elucidating a material's thermal expansion behavior. It stands in contrast to bulk measurement methods such as dilatometry due to its ability to characterize expansion at an atomic level. The unit cell and structure can be characterized at specific temperatures. This permits estimation of a material's CTE (linear or volumetric), as the appropriate dimensions for a unit cell can be directly extracted from an assembled fit to the x-ray diffraction data. Steps must often be taken to ensure that this data represents the actual sample and not an experimental artifact. Additionally, synchrotron x-ray radiation is often the most appealing type of source for these temperature dependent studies, primarily due to its versatility. Overall, the expansion properties of a crystalline solid (such as $YbZrF_7$) can be well understood through this technique [109].

1.10 Overview of Thesis

This thesis will focus on six major components related to $YbZrF_7$: synthesis, characterization, thermal expansion, behavior on compression, thermal decomposition, and moisture stability.

CHAPTER 2

SYNTHESIS OF $YbZrF_7$ AND INITIAL CHARACTERIZATION

2.1 Synthesis of Cubic $YbZrF_7$

Several different high temperature solid-state syntheses were performed to produce representative samples of cubic $YbZrF_7$, using a method adapted from Poulain, et. al [72]. Variations from synthesis to synthesis included length of reaction vessel, annealing temperature(s), reactant quantities, duration of heating, and cooling procedure. Additionally, different sources of the reagents (YbF_3 and ZrF_4) were employed. All other procedural steps were identical.

Nickel 200 tubing was cut and crushed at one end using a 3-jaw lathe chuck. This end was then completely sealed by arc-welding in an argon atmosphere. The nickel tube was then cleaned for at least five minutes using a 2:1 solution (1 M hydrochloric acid: distilled water) heated to 60 – 70 °C. It was then rinsed in distilled water and scrupulously dried in a 100 °C oven. A pressure controlled, inert nitrogen atmosphere glove box was utilized in order to handle the reagents, as many metal fluorides are known to react with water to produce hydrofluoric acid [110]. YbF_3 (230.05 g mol^{-1}) and ZrF_4 (167.22 g mol^{-1}) were weighed in stoichiometric quantities according to the following reaction scheme:

$$YbF_{3\ (s)} + ZrF_{4\ (s)} \rightarrow YbZrF_{7\ (s)}$$

Several syntheses (**A**-**H**) were performed for this investigation. The reagents used are specified in **Table 2.1** and **Table 2.2**. All future references to this set of cubic $YbZrF_7$ samples will follow this **A**-**G** designation. The two reactants were combined and thoroughly ground together using a mortar and pestle. The reagents were loaded into the nickel tube. The open end of the tube was closed using a hydraulic press and then sealed by arc-welding. The welded tube was sealed inside an evacuated fused-quartz ampule. The quartz tube was heated in a Lindberg Blue M programmable furnace. Heating and cooling parameters for each synthesis are shown in **Table 2.3**. The labeling convention for each synthesis is shown in **Table 2.1** and **Table 2.2**. The entire synthesis procedure is summarized in the images below.

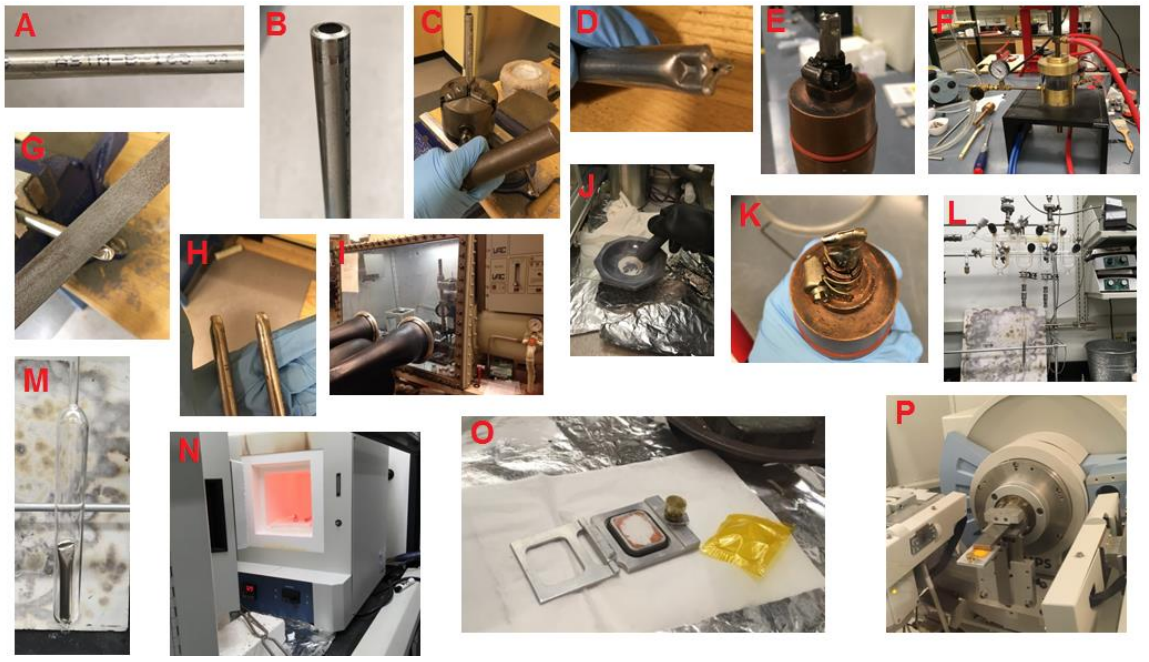

Figure 2.1: Laboratory synthesis components including: nickel tubes (A, B); crimped nickel tubes (C, D); welding setup (E, F); filed nickel tubes (G, H); glovebox (I); mortar and pestle with reagents (J); welded tubes (K); vacuum line (L); fused quartz vessel (M); furnace (N); x-ray diffraction container (O); laboratory x-ray diffractometer setup (P)

Table 2.1: Cubic $YbZrF_7$ Sample Preparation Information (Part I)

Sample ID	**Laboratory Notebook Notation**	**YbF_3 Mass (g)**	**ZrF_4 Mass (g)**	**$YbZrF_7$ Mass (g)**	**YbF_3 Supplier and Purity**	**ZrF_4 Supplier and Purity**
A	JT-01-09-1 $YbZrF_7$	0.300	0.218	0.518	Alfa Aesar (99.9 %)	Sigma Aldrich (99.9 %)
B	JT-01-09-2 $YbZrF_7$	0.600	0.436	1.036	Alfa Aesar (99.9 %)	Strem Chemicals (99.9 %)
C	JT-01-62-2 $YbZrF_7$ RH	0.600	0.436	1.036	Alfa Aesar (99.9 %)	Strem Chemicals (99.9 %)
D	JT-01-62-3 $YbZrF_7$	0.600	0.436	1.036	Alfa Aesar (99.9 %)	Strem Chemicals (99.9 %)
E	JT-01-74-1 $YbZrF_7$	2.606	1.894	4.500	Alfa Aesar (99.9 %)	Strem Chemicals (99.9 %)
F	JT-01-88-1 $YbZrF_7$	0.753	0.547	1.300	Alfa Aesar (99.9 %)	Strem Chemicals (99.9 %)

Table 2.2: Cubic $YbZrF_7$ Sample Preparation Information (Part II)

Sample ID	**Laboratory Notebook Notation**	**YbF_3 Mass (g)**	**ZrF_4 Mass (g)**	**$YbZrF_7$ Mass (g)**	**YbF_3 Supplier and Purity**	**ZrF_4 Supplier and Purity**
G	JT-01-112-1 $YbZrF_7$	0.898	0.652	1.550	Suzhou Putin (99.9 %)	Strem Chemicals (99.9 %)

Table 2.3: Heating and Cooling Schedules for Cubic $YbZrF_7$ Samples

Sample ID	1st Stage	2nd Stage	3rd Stage	4th Stage
A	RT → 1000 °C (2 hours)	1000 °C (48 hours)	Water quenched to RT	---
B	RT → 1000 °C (2 hours)	1000 °C (48 hours)	Water quenched to RT	---
C	RT → 1000 °C (3 hours)	1000 °C (72 hours)	Water quenched to RT	Repeat 1 - 3
D	RT → 1000 °C (3 hours)	1000 °C (72 hours)	1000 °C → RT (24 hours)	---
E	RT → 1000 °C (3 hours)	1000 °C (144 hours)	Water quenched to RT	---
F	RT → 1000 °C (3 hours)	1000 °C (72 hours)	Ice quenched to 0 °C	---
G	RT → 1000 °C (3 hours)	1000 °C (72 hours)	Ice quenched to 0 °C	---

2.2 Synthesis of Monoclinic $YbZrF_7$

The synthesis of monoclinic $YbZrF_7$ made use of the procedures described in **Section 2.1** for the steps prior to heat treatment. Additionally, the reagent amounts and sources differed. The primary details are outlined in **Table 2.4** and **Table 2.5**.

Table 2.4: Monoclinic $YbZrF_7$ Sample Preparation

Sample ID	Laboratory Notebook Notation	YbF_3 Mass (g)	ZrF_4 Mass (g)	$YbZrF_7$ Mass (g)	YbF_3 Supplier and Purity	ZrF_4 Supplier and Purity
H	JT-01-114-1 $YbZrF_7$ RH	0.579	0.421	1.000	Suzhou Putin (99.9 %)	Sigma Aldrich (99.9 %)

Table 2.5: Heating and Cooling Schedules for Monoclinic $YbZrF_7$ Sample

Sample ID	1st Stage	2nd Stage	3rd Stage	4th Stage
H	RT → 675 °C (3 hours)	675 °C (24 hours)	675 °C → RT (furnace switched off)	Repeat 1 - 3

2.3 Characterization by Laboratory PXRD

After the heat treatment, the nickel tubes were opened in a nitrogen-filled glove box and the $YbZrF_7$ was ground to a fine powder. All the samples had a uniform white appearance. Approximately 0.3 grams of cubic or monoclinic $YbZrF_7$ were used for laboratory PXRD measurements. Each sample was inserted into an aluminium sample holder and sealed under a thin Kapton film. These initial PXRD measurements were performed using a Phillips X'Pert MPD Powder Diffractometer (Cu $K_{\alpha1}/K_{\alpha2}$ radiation). Specific relevant parameters for all cubic and monoclinic $YbZrF_7$ sample analyses are given in **Table 2.6**, **Table A.1**, and **Table A.2**.

Table 2.6: Laboratory Powder X-Ray Diffractometer Measurement Parameters for $YbZrF_7$ Analyses

Sample ID	Scan Range (2θ)	Step Size (2θ) and Counting Time (s)	$K\alpha_1$ (Å)	$K\alpha_2$ (Å)	$K\alpha_2$ / $K\alpha_1$ Intensity Ratio
A	20.000 – 89.980	0.020, 1.50	1.540598	1.544426	0.50
B – H	15.000 – 120.000	0.020, 1.35	1.540598	1.544426	0.50

2.3.1 Analysis of the Laboratory PXRD Data for Cubic $YbZrF_7$

The resulting x-ray diffraction powder patterns were recorded in the form of simple (.xy) files, which contain diffraction intensity versus diffraction angle 2θ. These files were converted by the software program CMPR to General Structure Analysis System (GSAS) readable files (.gsas) [111]. GSAS acted as the primary agent for all subsequent PXRD data analysis [112]. EXPGUI, a graphical-user interface for GSAS, allowed for numerous parameters to be altered or refined in order to develop a model that reproduced the diffraction data [113].

A structural model (**Table 2.7**) was obtained from a crystallographic information file (CIF) based on neutron diffraction studies conducted by Poulain, et. al for cubic $YbZrF_7$ [72]. The information contained within this file included lattice constants, atomic fractional coordinates, site multiplicities, and atomic site occupancies. Two types of fluorine were present in this particular model, whereas only one type of both ytterbium and zirconium were involved. The Rietveld fitting method was utilized for all laboratory PXRD data analysis. Room temperature (approximately 22 °C) was consistently adhered to for all PXRD initial laboratory measurements. All employed model fitting parameters, refinements, and GSAS specific settings for each analyzed sample of cubic $YbZrF_7$ are given in **Tables A.3 – A.9**. In GSAS, fractional coordinates, occupancies, and atomic displacement parameters (U_{iso}) were not refined. Refinement of these parameters frequently resulted in complications, such as divergence. The unit cell constants from converged GSAS fits and graphics showing the fits are given in **Table 2.8** and **Figures 2.2 – 2.8** respectively.

As shown in **Figures 2.2 – 2.8**, the Rietveld fits to the laboratory PXRD data showed good agreement between observed and calculated peak position. However, peak intensity was not well described. All refined lattice constants (**Table 2.8**) deviated slightly from Poulain's original value (**Table 2.7**). a = 4.07 Å was reported in the original literature, compared to a refined lattice constant a = 4.10 Å [72]. Interestingly, a single sample (**G**) deviated to a lesser extent (a = 4.08 Å) compared to the other samples. This may be indicative of a lower degree of oxide contamination in the YbF_3 reagent, as this was the only variable which could have caused this. The samples **C-F** also showed impurity peaks which were determined to be a combination of unreacted YbF_3 and ZrF_4. Peak overlap of YbF_3 and ZrF_4 prevented an identification of which specific starting material was responsible for the highest intensity impurity peak. Synchrotron x-ray measurements (**Chapter 3**) qualitatively confirmed the presence of both YbF_3 and ZrF_4 impurities in these samples.

Table 2.7: Structural Model Reported By Poulain, et. al. for Cubic $YbZrF_7$ [72]

Pm – 3m	**Fractional Coordinate (x)**	**Fractional Coordinate (y)**	**Fractional Coordinate (z)**
Yb (1)	0.000	0.000	0.060 (14)
Zr (1)	0.000	0.000	0.060 (14)
F (1)	0.500	0.052 (3)	0.052
F (2)	0.500	0.289 (9)	0.064 (8)
	Multiplicity	**Occupancy**	**U_{iso} ($Å^2$)**
Yb (1)	6	0.0830	0.02166
Zr (1)	6	0.0830	0.02166
F (1)	12	0.2220	0.03926
F (2)	24	0.0330	0.03825
Lattice Constant (Å)		4.067	

Table 2.8: Unit Cell Constants for the Cubic $YbZrF_7$ Samples as Determined from Rietveld Fits to the Laboratory Powder X-Ray Diffraction Data

Sample ID	Lattice Constant (Å)	Unit Cell Volume ($Å^3$)	X^2 (GSAS Fit)
A	4.09713 (3)	68.777 (2)	2.844
B	4.10322 (4)	69.084 (2)	4.264
C	4.10596 (7)	69.222 (4)	24.51
D	4.09876 (8)	68.858 (4)	3.440
E	4.0977 (1)	68.807 (5)	6.637
F	4.10021 (6)	68.932 (3)	3.707
G	4.0816 (2)	68.000 (8)	2.942
AVERAGE	4.098 (8)	68.8 (4)	---

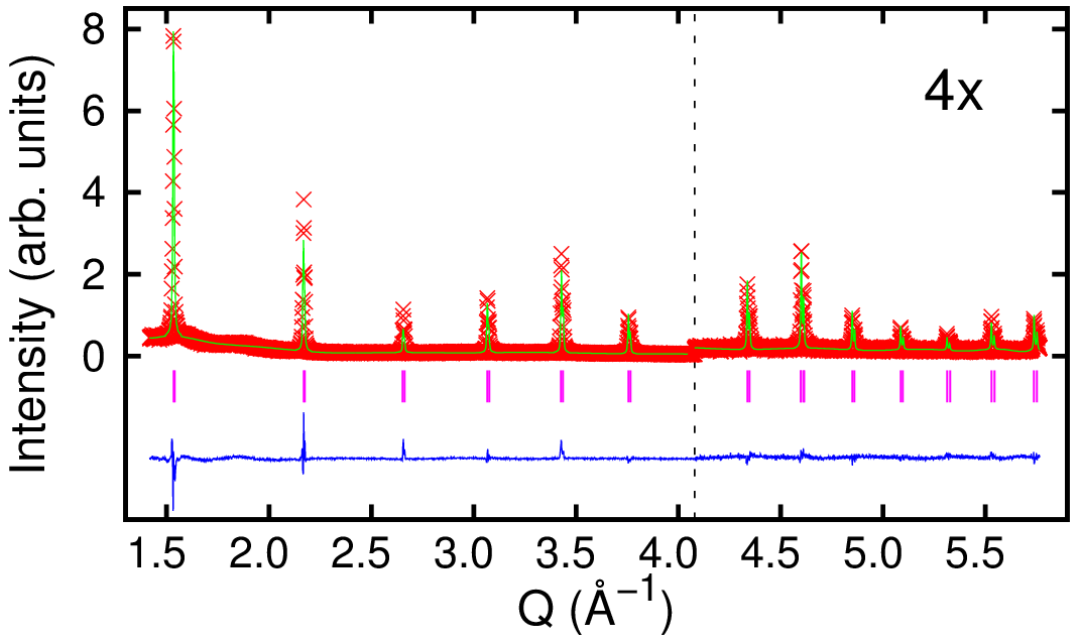

Figure 2.2: The Rietveld fit (green) for cubic $YbZrF_7$ (Sample **A**) is compared to the original data, in red. Peak markers are shown in pink. High angle intensities are magnified. A difference curve is shown in blue.

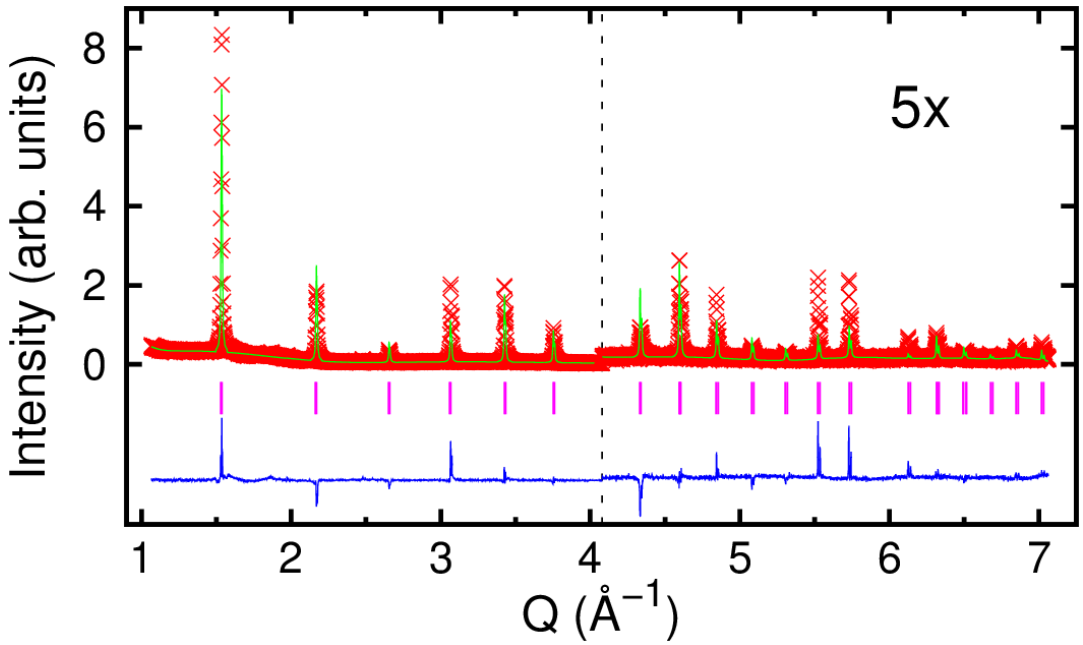

Figure 2.3: The Rietveld fit (green) for cubic $YbZrF_7$ (Sample **B**) is compared to the original data, in red. Peak markers are shown in pink. High angle intensities are magnified. A difference curve is shown in blue.

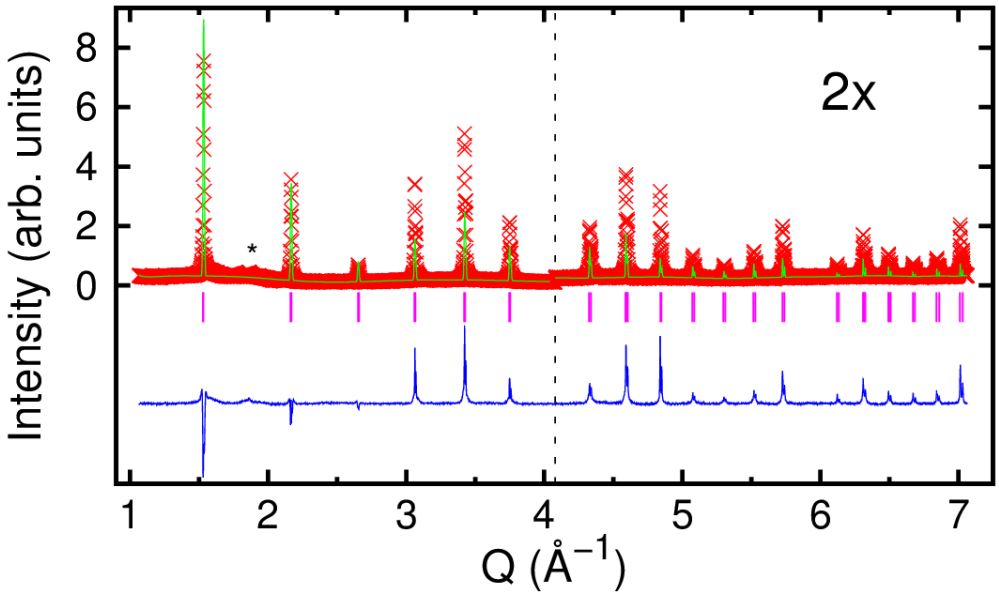

Figure 2.4: The Rietveld fit (green) for cubic $YbZrF_7$ (Sample **C**) is compared to the original data, in red. Peak markers are shown in pink. High angle intensities are magnified. YbF_3 and ZrF_4 impurities (*) are indicated. A difference curve is shown in blue.

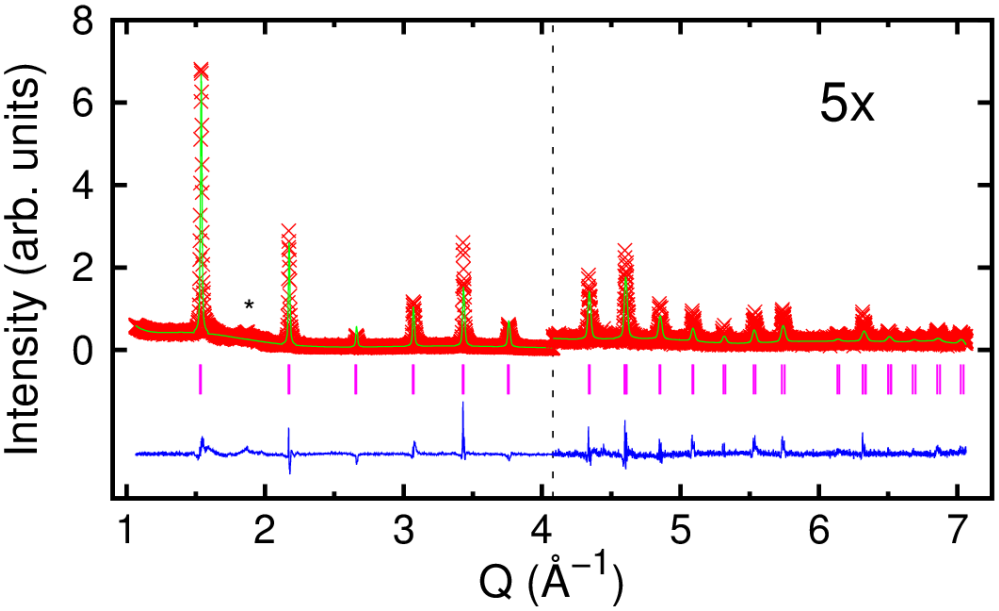

Figure 2.5: The Rietveld fit (green) for cubic $YbZrF_7$ (Sample **D**) is compared to the original data, in red. Peak markers are shown in pink. High angle intensities are magnified. YbF_3 and ZrF_4 impurities (*) are indicated. A difference curve is shown in blue.

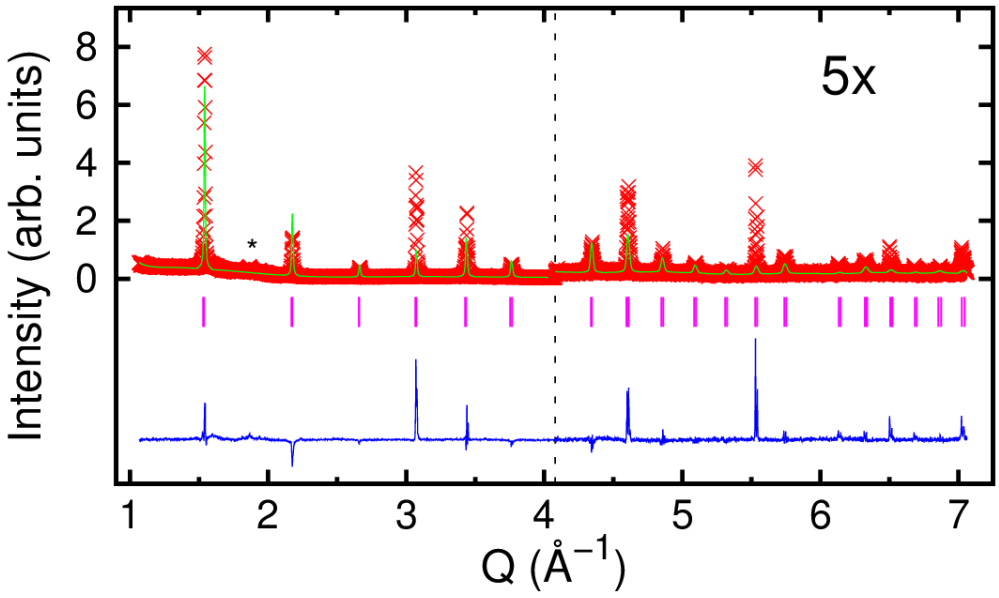

Figure 2.6: The Rietveld fit (green) for cubic $YbZrF_7$ (Sample **E**) is compared to the original data, in red. Peak markers are shown in pink. High angle intensities are magnified. YbF_3 and ZrF_4 impurities (*) are indicated. A difference curve is shown in blue.

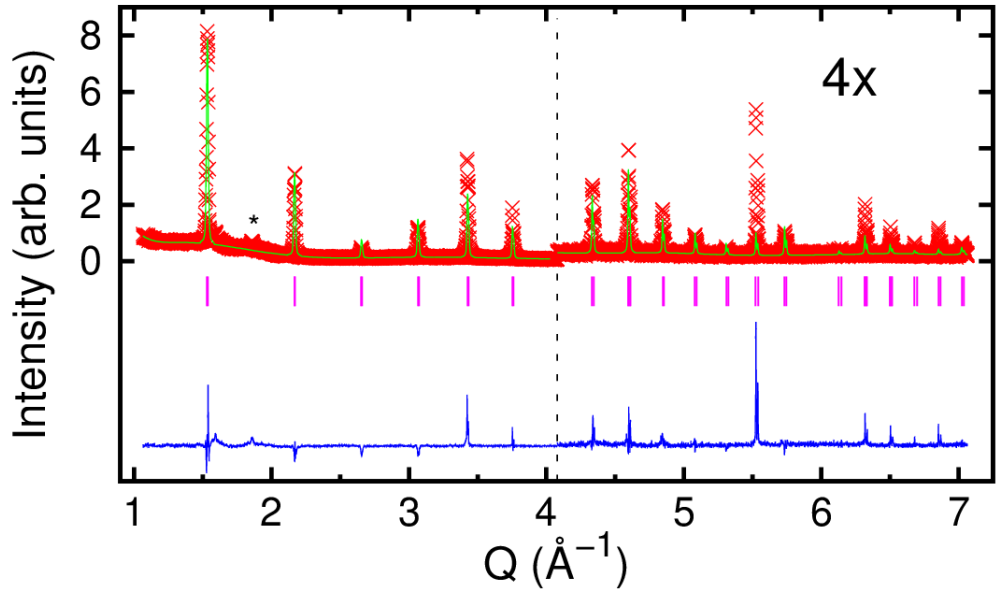

Figure 2.7: The Rietveld fit (green) for cubic $YbZrF_7$ (Sample **F**) is compared to the original data, in red. Peak markers are shown in pink. High angle intensities are magnified. YbF_3 and ZrF_4 impurities (*) are indicated. A difference curve is shown in blue.

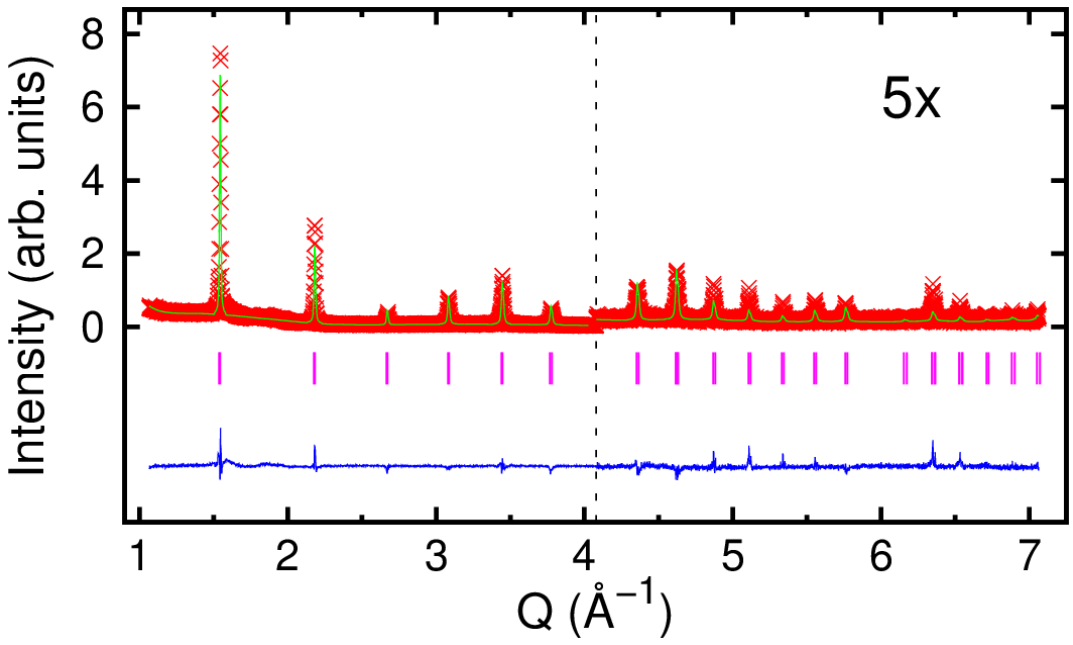

Figure 2.8: The Rietveld fit (green) for cubic $YbZrF_7$ (Sample **G**) is compared to the original data, in red. Peak markers are shown in pink. High angle intensities are magnified. A difference curve is shown in blue.

2.3.2 Analysis of Monoclinic $YbZrF_7$ Laboratory PXRD Data

Preliminary assessment of the diffraction pattern strongly suggested that a non-cubic material was formed. The generated PXRD pattern for (presumed) monoclinic $YbZrF_7$ was analyzed in an identical manner to cubic $YbZrF_7$. Essential details and adjustments are briefly discussed. The resulting diffraction pattern, which comprised intensity plotted as a function incident angle 2θ, was converted to a GSAS formatted file by CMPR [111-112]. The software program EXPGUI then applied the data file (.gsas) and instrument parameter file (.prm) to a histogram. A single phase model consisting of $YbZrF_7$ (space group $P2_1$ / n) was used. The initial structural model (**Tables A.10**, **A.11**) was developed by transforming the monoclinic lattice constants for $YbZrF_7$ ($P2_1$) published by Poulain, et. al. to a monoclinic structural model reported by Graudejus, et. al. for $SmZrF_7$ [70-71].

All subsequent attempts to fit the data were unsuccessful due to the presence of additional peaks that were not associated with monoclinic $YbZrF_7$. These additional peaks could not be definitively attributed to starting material or a different stoichiometry of ytterbium zirconium fluoride. This was a result of peak overlap at intermediate angles between starting material and the proposed monoclinic $YbZrF_7$. In sum, it was not confirmed that the sample contained pure monoclinic $YbZrF_7$. Despite these shortcomings, the obtained diffraction pattern is shown in **Figure 2.9**. The number of peaks observed exceed the number allowed in the structural model, which suggested impure monoclinic $YbZrF_7$. It is therefore a sample of little practical use, although it may be that the attempted reaction is simply incomplete.

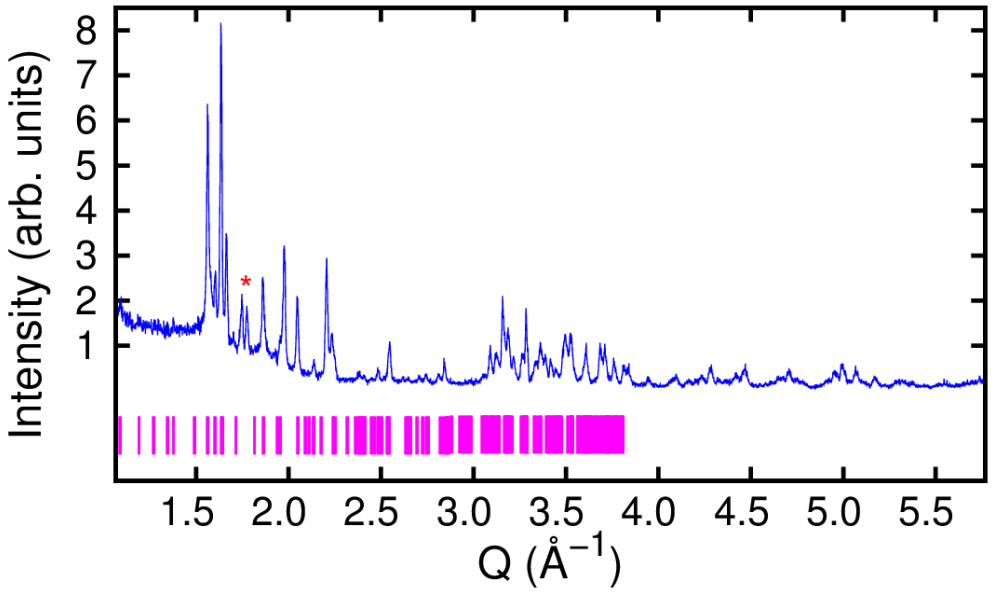

Figure 2.9: The laboratory x-ray diffraction pattern for an attempted synthesis of monoclinic $YbZrF_7$ is shown in blue. The expected peaks according to the developed structural model are labeled in pink. Two high-intensity peaks (*) could not be attributed to monoclinic $YbZrF_7$.

2.4 Elemental Analysis

Elemental analysis of cubic $YbZrF_7$ (sample **E**) was performed in order to confirm the proposed stoichiometry of the compound. For all cubic varieties of $YbZrF_7$ that were synthesized, theoretical fractional composition would consist of ytterbium and zirconium in equal proportions. Data was acquired at Galbraith Laboratories, Inc. (Knoxville, TN). The method used was known as ME-70, which involved inductively coupled plasma atomic emission spectroscopy (ICP-AES). The measurement of spectral intensities characteristic of each elemental component of interest permitted quantification. The instrument, an ICP-OES Optima 5300, maintained a quantification limit of 0.01 to 2 ppm and an approximate precision of ± 10 % relative standard deviation [114]. The sample amount used was 104.01 mg. The obtained laboratory report is shown in **Figure A.9**.

Table 2.9: Elemental Analysis for Cubic $YbZrF_7$ (Sample **E**)

Identified Element	Relative Percentage (Experimental)	Relative Percentage (Expected)	% Error	Amount of Element Measured (mg)
Yb	44.3	43.6	1.6	46.08
Zr	21.3	23.0	7.4	22.15
Ni	0.558	---	---	0.58

The elemental analysis identified a minor nickel impurity, which was not necessarily an unexpected finding. A small amount of nickel fragments originating from the reaction vessel likely contaminated the $YbZrF_7$ sample. This was to an extremely small extent as the impurity could not be detected in the laboratory x-ray diffraction pattern, as shown in **Figure 2.6**. For ytterbium and zirconium, the deviations from expected values error were within the allowed error claimed by Galbraith Laboratories [114].

2.5 Density Measurement

The density of cubic $YbZrF_7$ (sample **F**) was determined using a Micromeritics AccuPyc II 1340 gas pycnometer apparatus within a nitrogen filled (inert atmosphere) glove box. The internal temperature was adjusted to 24.5 °C. Supply gas was ultra-high purity helium.

Approximately 0.8190 (1) g of $YbZrF_7$ (**F**) was inserted into the internal pycnometer sample chamber. Upon sealing the chamber, a stabilized helium pressure (19.5 psi) was achieved, averaged over ten gas flow cycles. A sample volume (0.1691 (1) cm^3) was calculated according to the specific change in pressure induced by the $YbZrF_7$ sample relative to the system's internal reference. Thus, a density of 4.8433 (6) g cm^{-3} was experimentally established for cubic $YbZrF_7$. This compared reasonably well to both published theoretical data (4.87 g cm^{-3}) and to density calculated by GSAS from the initial laboratory PXRD data of sample **F** (4.77 g cm^{-3}) using the structural model outlined in **Table 2.7** and **Tables A.3 – A.9** [72].

CHAPTER 3

TEMPERATURE DEPENDENT BEHAVIOR OF $YbZrF_7$

3.1 Introduction

In order to characterize $YbZrF_7$ and its expansion behavior, variable temperature powder x-ray diffraction (PXRD) was used. In principal, this can be achieved by a variety of different techniques [27]. The approach employed involved incrementally altering the sample temperature. At a desired point, the temperature is held constant and a powder pattern is obtained. Once a fit to the powder pattern is produced, a unit cell volume can be determined. These temperature-resolved measurements of unit cell volume are aided by a high quality x-ray source. Therefore, high-intensity x-ray synchrotron radiation is ideal. Knowledge of both a unit cell volume change and its respective temperature change effectively allow for the expansion behavior to be quantified, as provided in **Equation 1.3**. The volumetric coefficient of thermal expansion (VCTE) can then be estimated on a point-by-point basis or averaged over a selected temperature range [61-62]. Quantitatively determining the expansion characteristics of $YbZrF_7$ is the primary area of exploration in this thesis. The most significant focus surrounds the role of interstitial fluoride anion excess and how it affects the expected negative thermal expansion (NTE) of the ReO_3 structure. It is hypothesized that if a corner to edge sharing structural transformation occurs, the coupled rocking of the octahedral in the ReO_3 structure will be impeded and NTE will be reduced.

3.2 Experimental Methods and Materials

Synchrotron x-ray diffraction data was acquired at Argonne National Laboratory, Advanced Photon Source (APS), sector 17-BM. High intensity x-rays of a selected wavelength were used to perform several different variable temperature experiments. Cubic $YbZrF_7$ was loaded into an epoxy-sealed Kapton capillary tube of 0.86 mm outer diameter. An Oxford Cryosystems Cryostream heated and cooled the sample over the temperature range 100 to 500 K. This equipment transported nitrogen gas (of known temperature) over the exterior of the Kapton tube. For future reference, CRYO will serve as the designation for measurements performed using this apparatus. In CRYO x-ray measurements, the sample was cooled from room temperature to 100 K, held at 100 K for 15 minutes, heated to 500 K at a rate of 180 K per hour, held constant at 500 K for 15 minutes, and cooled to 100 K at a rate of 180 K per hour. For temperatures above 500 K (denoted by FURN), a Kathanl A-1 type wire-bound furnace apparatus was employed, where a fused quartz capillary tube served as the sample container [115]. Temperature in the furnace environment was determined using a sheathed K-type thermocouple, Omega Engineering, Stamford, CT, USA. In each case, scattering intensity was recorded on a 2D amorphous silicon PerkinElmer x-ray detector. Specific experimental details are highlighted below (**Tables 3.1**, **3.2**) for associated synchrotron data. Note that uncalibrated temperatures will first be discussed and analyzed. The effect of introducing a temperature calibration will later be described.

For CRYO heating from 100 to 500 K, 134 temperature-resolved x-ray diffraction patterns were generated using GSAS-II for integration [112]. This was also true for CRYO cooling between 500 and 100 K. Thus, a total of 268 x-ray diffraction patterns

were collected for 268 respective temperatures in method α. Method β involved two separate cooling stages and two separate heating stages. The first cooling stage led to a set of 67 integrated diffraction patterns. 134 integrated diffraction patterns were obtained for the three subsequent heating and cooling stages. This resulted in a total of 469 x-ray patterns, each collected for a respective temperature. The temperature increment was approximately 3 K for all CRYO experiments.

Table 3.1: Variable Temperature Heating and Cooling Profiles

Method	Stage 1	Stage 2	Stage 3	Stage 4	Diffraction Patterns
α	100 K - 500 K	500 K - 100 K	---	---	268
β	299 K - 100 K	100 K - 500 K	500 K - 100 K	100 K - 500 K	469
γ	304 K – 1057 K	---	---	---	332

Following the data integration, all of the x-ray diffraction patterns (now converted to the format of .fxye files) were fit using a model adapted from the work of Poulain, et. al. that was previously applied to the laboratory x-ray diffraction data for cubic $YbZrF_7$ in **Section 2.3** [72]. The crucial details and modifications will be discussed in terms of each specific experiment performed. GSAS was employed for the analyses using the EXPGUI interface [113]. For CRYO-C_1 and CRYO-C_2, anomalous dispersion terms (**Table 3.3**)

specific to the experimental x-ray wavelength were used [116]. However, their usage had minimal impact on the quality of the initial Rietveld fit.

Table 3.2: Primary Variable Temperature Experimental Settings for Selected $YbZrF_7$ Samples

Sample ID	Experiment ID	Date	Beamline Sector	Temperature Profile	Internal Reference Material	Operating X-Ray λ (Å)
A	CRYO-A	April 2015	17-BM	Method α	None	0.72950
C	CRYO-C_1	April 2016	17-BM	Method α	Silicon	0.72768
C	CRYO-C_2	April 2016	17-BM	Method β	Silicon	0.72768
F	CRYO-F	December 2016	17-BM	Method α	Silicon	0.45336
D	FURN-D	April 2016	17-BM	Method γ	None	0.72768

Table 3.3: Anomalous Dispersion Terms Applied for CRYO-C_1 and CRYO-C_2

Atom	Δf’	Δf’’
Yb	- 0.434	5.807
Zr	- 2.380	0.587
F	0.018	0.011

For CRYO-A, an initial Rietveld fit was established for a non-calibrated temperature of 100 K, as shown in **Figure 3.1**. The unit cell parameter was refined to accommodate any expansion or contraction on cooling from room temperature. The atomic displacement parameters (U_{iso}) for each atom were also refined. Each atom's U_{iso} value was constrained to vary in the same way as that of the other atoms. The refined lattice constant, unit cell volume, and atomic displacement parameters from this initial Rietveld fit are listed in **Table 3.4**. Note that the fractional coordinates, multiplicities, and occupancies were not varied from their original values as given in **Table A.9** All other relevant refinements and GSAS settings employed in the initial fit at 100 K are given in **Table A.12**. For the profile parameters not refined, the default values were maintained. Following optimization of the initial Rietveld fit, a sequential series of GSAS fits was performed [117]. Each of the diffraction 267 diffraction patterns was fit sequentially. The Rietveld fit generated for this $YbZrF_7$ sample at 500 K is shown in **Figure 3.2**. The fits were conducted in consecutive order beginning at stage 1 and proceeding to stage 2, generating a set of 268 unit cell volumes for their respective temperatures (**Figure 3.3**), along with corresponding weighted R-factor values (**Figure A.10**) calculated by GSAS. Point by point VCTE values (**Equation 3.1**) were also calculated based on this volume versus temperature data, as shown in **Figure 3.4**.

$$\alpha_V \approx \frac{1}{V_{AVG_{a,b}}} \left(\frac{V_b - V_a}{T_b - T_a} \right) \quad \dots T_b > T_a \qquad \mathbf{3.1}$$

Point by point CTE values often result in zero CTE, as any non-change in volume anywhere along the heating or cooling curve guarantees a value of zero. Meaningful

insight can only be extracted from point by point CTE values when compared to their heating and cooling curves, as this provides a broader perspective of what is taking place.

The volume versus temperature measurements for CRYO-C_1 were collected in a similar fashion to CRYO-A, with a few notable exceptions. The $YbZrF_7$ sample was combined with a small amount of silicon, which served as an internal reference. The apparent behavior of unit cell volumes for silicon was used to identify problems, as silicon's thermal expansion is extremely well known [118]. The synchrotron wavelength was altered slightly (**Table 3.2**), while the heating and cooling schedule remained the same. The GSAS settings used in the case of CRYO-A were also adopted when modeling the data from CRYO-C_1. The second phase (silicon) was initially modeled using a structure reported by Többens, et. al [119]. The GSAS analysis approach remained consistent to what was performed for the CRYO-A data. Structural models from the Rietveld fit at 100 K were optimized for both $YbZrF_7$ (**Tables 3.5**, **A.13**) and silicon (**Tables 3.6**, **A.14**). A sequential GSAS refinement produced a collection of Rietveld fits (R-factors shown in **Figure A.11**), which subsequently allowed for the calculation of temperature-resolved unit cell volumes. These volumes were compared to their respective temperatures for both heating and cooling of $YbZrF_7$ (**Figure 3.6**) and silicon (**Figure 3.7**). The volumetric CTE was calculated for every third point for both $YbZrF_7$ (**Figure 3.8**) and silicon (**Figure 3.9**), where the volume was averaged over three points as opposed to two before. For the purposes of clarity, this metric will be further detailed. Each consecutive unit cell volume can be labeled: V_1, V_2, V_3 … V_n, where n represents the final unit cell volume. Each unit cell volume maintained a respective temperature labeled: T_1, T_2, T_3 … T_n. The average volume for the first three points was then the average of V_1, V_2, and V_3.

The volumetric CTE was then calculated according to **Equation 3.2**. This process next calculated the average volume of V_4, V_5, and V_6. It would proceed in the manner previously described. The unit cell volumes were plotted as a function of the average temperature of each of the three points. These third point by point CTE values were calculated for CRYO-C_1, CRYO-C_2, and CRYO-F.

$$\alpha_V \approx \frac{1}{V_{AVG_{1,2,3}}} \left(\frac{V_3 - V_1}{T_3 - T_1} \right) \qquad \mathbf{3.2}$$

Experimentally, the primary difference between CRYO-C_1 and CRYO-C_2 involved the heating and cooling schedule, where CRYO-C_2 was heated and cooled twice as shown in **Table 3.1**. For CRYO-C_2 variable temperature measurements, silicon also served as an internal reference. Structural models were refined using GSAS starting from a Rietveld fit at 299 K, as shown in **Figure 3.10**. $YbZrF_7$ was again fit using a model from that of Poulain, et. al. (T**ables 3.7**, **A.15**) while the silicon was fit using a model from Többens, et. al. (**Tables 3.8**, **A.16**) [72,119]. Following a sequential Rietveld fit to all subsequent powder patterns (R-factors shown in **Figure A.12**), heating and cooling curves representative of the unit cell volume dependence on temperature were obtained for $YbZrF_7$ (**Figure 3.11**) and silicon (**Figure 3.12**). Volumetric CTE values were again calculated based on every third temperature point for $YbZrF_7$ (**Figure 3.13**) and silicon (**Figure 3.14**).

CRYO-F was a replication of the CRYO-C_1 experiment in terms of all procedural steps. A Rietveld fit (**Figure 3.15**) at 100 K was performed using GSAS and models for $YbZrF_7$ (**Tables 3.9**, **A.17**) and silicon (**Tables 3.10**, **A.18**). A sequential GSAS refinement was

performed based on this initial Rietveld fit. The calculated R-factors for each fit are shown in **Figure A.13**. This allowed for an estimation of temperature-resolved unit cell volumes for $YbZrF_7$ (**Figure 3.16**) and silicon (**Figure 3.17**). At every third temperature point, the volumetric CTE was calculated for $YbZrF_7$ (**Figure 3.18**) and silicon (**Figure 3.19**) using the previously described scheme.

Temperature calibration was performed using a K-type thermocouple, which was inserted into the Kapton tube. The programmed heating and cooling schedule was implemented, and the temperature inside the tube was monitored by the thermocouple. The discrepancy between the programmed temperature and sample temperature could then be accounted for. The unit cell volumes ($YbZrF_7$ and silicon) were plotted versus the calibrated temperatures on both heating and cooling in **Figures A.14 – A.19**.

FURN-D was analyzed strictly on a qualitative basis according to a set of 332 temperature resolved diffraction patterns obtained between 304 and 1057 K.

3.3 Results and Discussion

In summary, five sets of $YbZrF_7$ variable temperature data were analyzed. Their heating and cooling schedules are listed in **Table 3.1**. The notation will follow what is given in **Table 3.2**. The data sets solely within the temperature range between 100 and 500 K are: CRYO-A, CRYO-C_1, CRYO-C_2, and CRYO-F.

Uncalibrated temperatures were initially used. The effect of applying a temperature calibration was minimal, as the resulting heating and cooling curves displayed essentially identical behavior. Thus, quantitative assessment of $YbZrF_7$ expansion behavior was

marginally affected by the temperature calibration. For completeness, temperature calibrated heating and cooling curves (unit cell volume) are shown in **Appendix-A**. Deviations between uncalibrated and calibrated temperatures were typically greatest near 100 K. Discussion of results, however, will be restricted to uncalibrated temperatures. This is in an effort to maintain consistency, as temperature calibrations were not used for all of the data sets.

3.3.1 Cryostream Enabled Synchrotron X-Ray Diffraction (100 – 500 K)

The Rietveld fits characterizing $YbZrF_7$ CRYO-A PXRD data at 100 K (**Figure 3.1**) and 500 K (**Figure 3.2**) were of high quality. This was especially true in comparison to the laboratory PXRD Rietveld fits shown in **Chapter 2**. $YbZrF_7$ was well described by the mode adapted from the work of Poulain, et. al. [72].

At 500 K, however, a small set of peaks appeared. This was most evident at low angles, Q = 1.5 – 2.0 Å, where these were not indicative of cubic $YbZrF_7$. Given that these low intensity peaks were not present at lower temperatures, they likely represented the beginning of a phase transition from cubic $YbZrF_7$ to monoclinic $YbZrF_7$. No monoclinic Reitveld fit was used to confirm this, as the peaks were of inadequate intensity. The obtained lattice constant (**Table 3.4**) was in reasonable agreement to the average lattice constant obtained for the laboratory PXRD data noted in **Table 2.8**. The behavior of $YbZrF_7$ depended on its thermal history, as shown in **Figure 3.3**. On heating, $YbZrF_7$ displayed highly erratic expansion behavior. On cooling, it sustained a more symmetric volumetric expansion. Approaching 500 K, the cooling and heating curves overlapped. Most interestingly, $YbZrF_7$ was observed to display a near zero volumetric CTE at

approximately room temperature (300 K) on both heating and cooling, as shown in **Figure 3.4**.

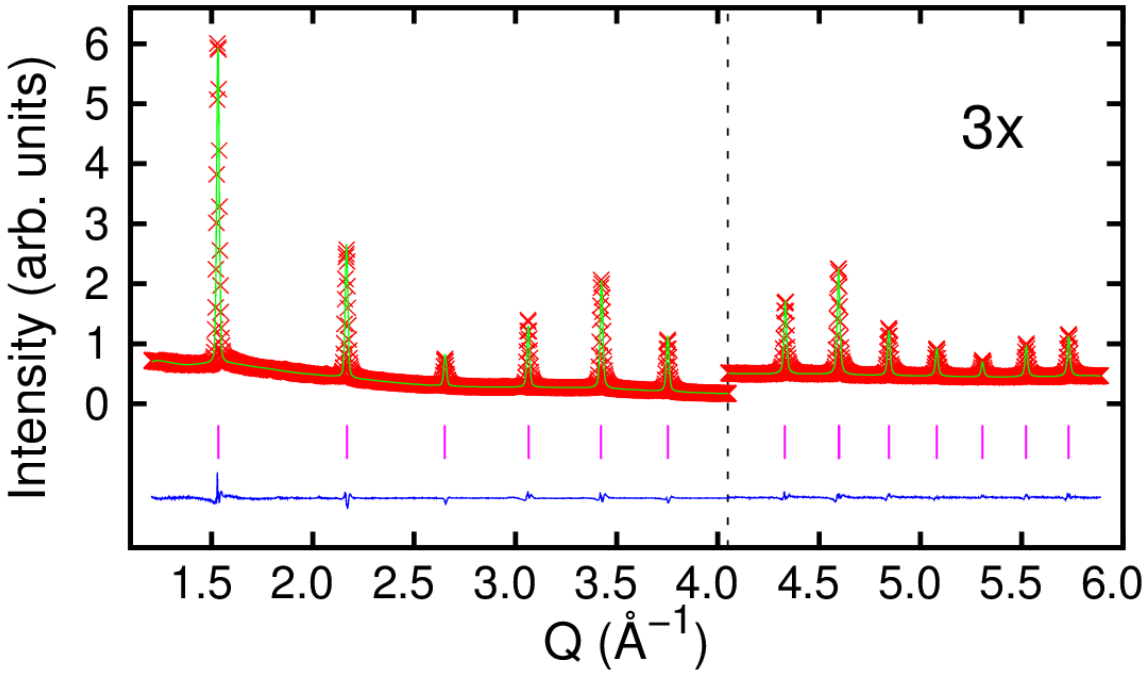

Figure 3.1: The initial CRYO-A Rietveld fit at 100 K (green) is displayed in comparison to the original data, in red. $YbZrF_7$ peak markers are labeled in pink. The difference curve is shown in blue. High angle peaks are magnified.

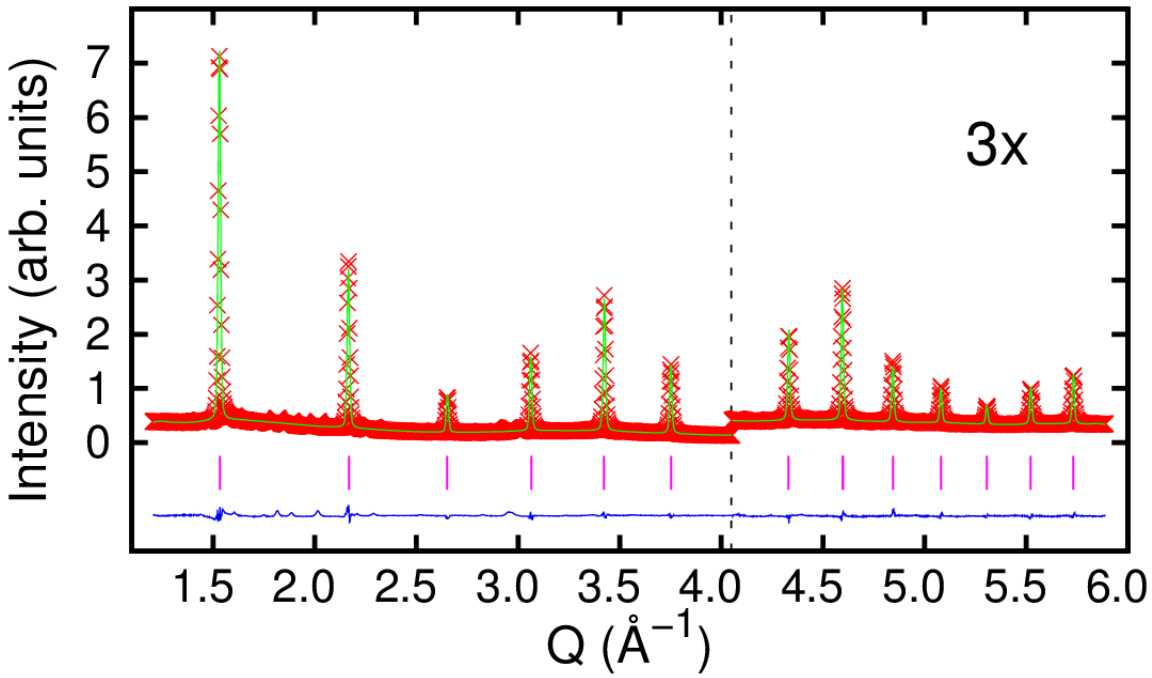

Figure 3.2: The CRYO-A Rietveld fit at 500 K (green) is displayed in comparison to the original data, in red. $YbZrF_7$ peak markers are labeled in pink. The difference curve is shown in blue. High angle peaks are magnified.

Table 3.4: Structural Model of $YbZrF_7$ Based on Initial Rietveld Fit at 100 K (CRYO-A)

Pm – 3m (Cubic)	**Fractional Coordinate (x)**	**Fractional Coordinate (y)**	**Fractional Coordinate (z)**
Yb (1)	0.000	0.000	0.060
Zr (1)	0.000	0.000	0.060
F (1)	0.500	0.052	0.052
F (2)	0.500	0.289	0.064
	Multiplicity	**Occupancy**	**Refined U_{iso} ($Å^2$)**
Yb (1)	6	0.0833	0.0167 (5)
Zr (1)	6	0.0833	0.0167 (5)
F (1)	12	0.2217	0.0343 (5)
F (2)	24	0.0325	0.0333 (5)
Refined Lattice Constant (Å)		4.10145 (6)	
Refined Unit Cell Volume ($Å^3$)		68.994 (3)	
X^2 (GSAS Fit)		1.690	

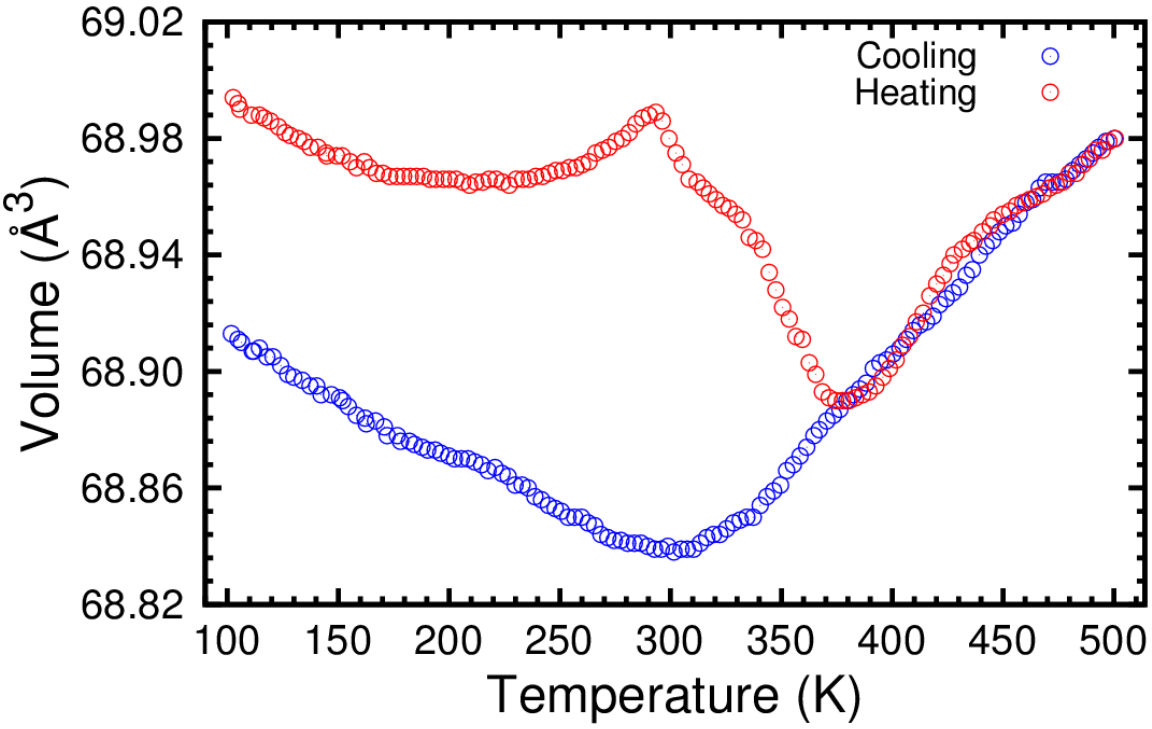

Figure 3.3: The unit cell volume of $YbZrF_7$ is plotted versus temperature for CRYO-A.

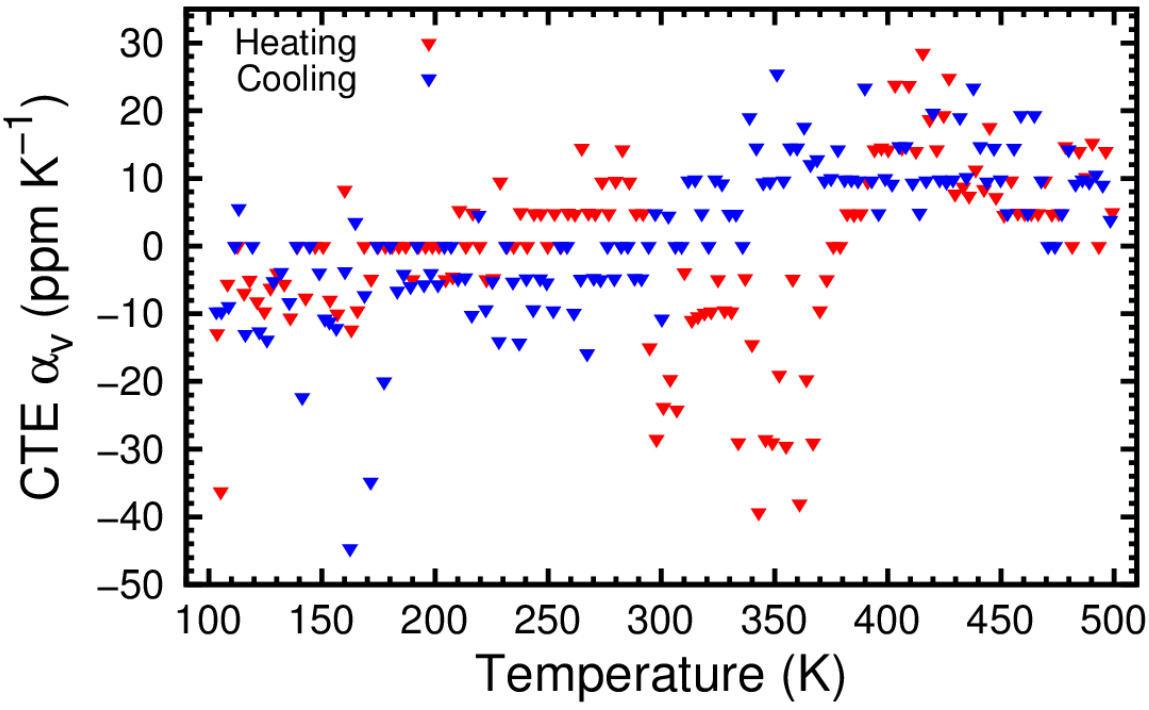

Figure 3.4: Point by point VCTE values are plotted versus temperature for CRYO-A.

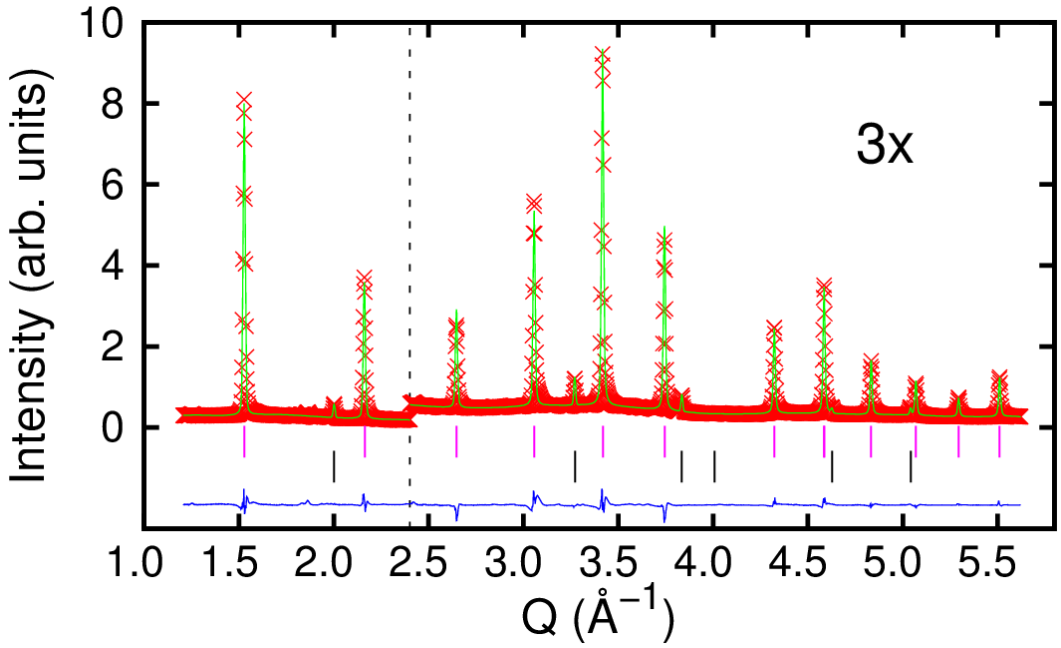

Figure 3.5: The initial CRYO-C_1 Rietveld fit at 100 K (green) is displayed in comparison to the original data, in red. Pink ($YbZrF_7$) and black (silicon) peak markers are indicated. The difference curve is shown in blue. High angle peaks are magnified.

The CRYO-C_1 diffraction pattern of cubic $YbZrF_7$ and silicon was very well described by the Rietveld fit at 100 K, as shown in **Figure 3.5**. In terms of the respective $YbZrF_7$ structural model (**Table 3.5**), the U_{iso} values were slightly altered from their values obtained in CRYO-A, while the lattice constants were of fair agreement with one another. Deviations may have been the result of experimental artifacts. Employment of silicon as an internal reference aimed to monitor the presence of such artifacts, so that changes in unit cell volume for $YbZrF_7$ could be correctly interpreted. The obtained lattice constant of silicon at 300 K, a = 5.4320 (8), was in good agreement with the lattice constant, a = 5.431073 (6), determined by Okada, et. al [118]. The expansion of $YbZrF_7$ was only partially reproduced compared to CRYO-A. Concurrently, $YbZrF_7$ thermal history dependence was replicated. As before, the heating and cooling curves of $YbZrF_7$ were not aligned with one another. This was in contrast to silicon (**Figure 3.7**), which showed no

thermal history dependence. In addition, the heating and cooling curves overlapped near 500 K.

Table 3.5: Structural Model for $YbZrF_7$ Based on Initial Rietveld Fit at 100 K (CRYO-C_1)

Pm – 3m (Cubic)	**Fractional Coordinate (x)**	**Fractional Coordinate (y)**	**Fractional Coordinate (z)**
Yb (1)	0.000	0.000	0.060
Zr (1)	0.000	0.000	0.060
F (1)	0.500	0.052	0.052
F (2)	0.500	0.289	0.064
	Multiplicity	**Occupancy**	**Refined U_{iso} ($Å^2$)**
Yb (1)	6	0.0833	0.0123 (5)
Zr (1)	6	0.0833	0.0123 (5)
F (1)	12	0.2217	0.0299 (5)
F (2)	24	0.0325	0.0289 (5)
Refined Lattice Constant (Å)		4.11005 (6)	
Refined Unit Cell Volume ($Å^3$)		69.429 (3)	
X^2 (GSAS Fit)		7.955	

Table 3.6: Structural Model for Silicon Based on Initial Rietveld Fit at 100 K (CRYO-C_1) [119]

Fd – 3m S (Cubic)	**Fractional Coordinate (x)**	**Fractional Coordinate (y)**	**Fractional Coordinate (z)**
Si (1)	0.125	0.125	0.125
	Multiplicity	**Occupancy**	**Refined U_{iso} ($Å^2$)**
Si (1)	8	1.000	0.020 (4)
Refined Lattice Constant (Å)		5.4303 (8)	
Refined Unit Cell Volume ($Å^3$)		160.13 (7)	
X^2 (GSAS Fit)		7.955	

This was previously observed in CRYO-A, as the $YbZrF_7$ maintained its volume on cooling until about 380 K. Strongly negative volumetric CTE values (**Figure 3.8**) were evident on heating from approximately 340 K to 380 K. This was attributed to local structural changes associated with fluoride mobility, as the structure had not previously been exposed to these temperatures due to its fast quench synthesis. Furthermore, near zero CTE extended over a larger temperature range on cooling when compared to CRYO-A. Silicon was also noted to sustain minimal thermal history dependence, as shown in **Figure 3.7**, where the heating and cooling expansion curves were in near alignment.

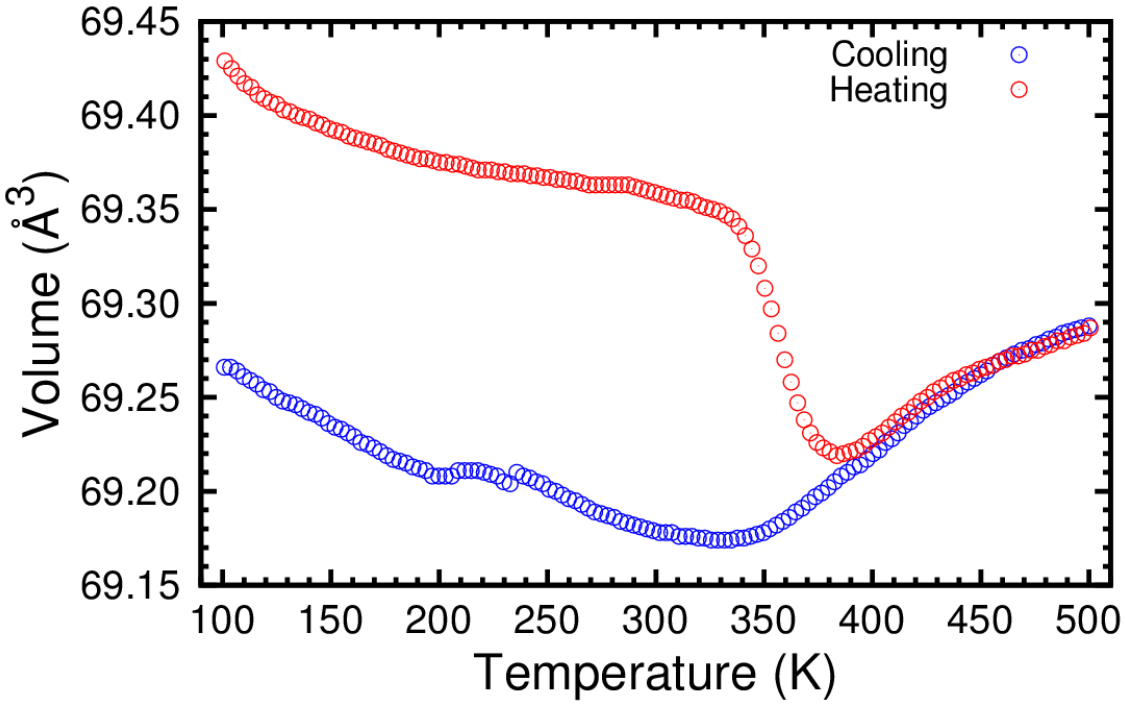

Figure 3.6: The unit cell volume of $YbZrF_7$ is plotted versus temperature for CRYO-C_1.

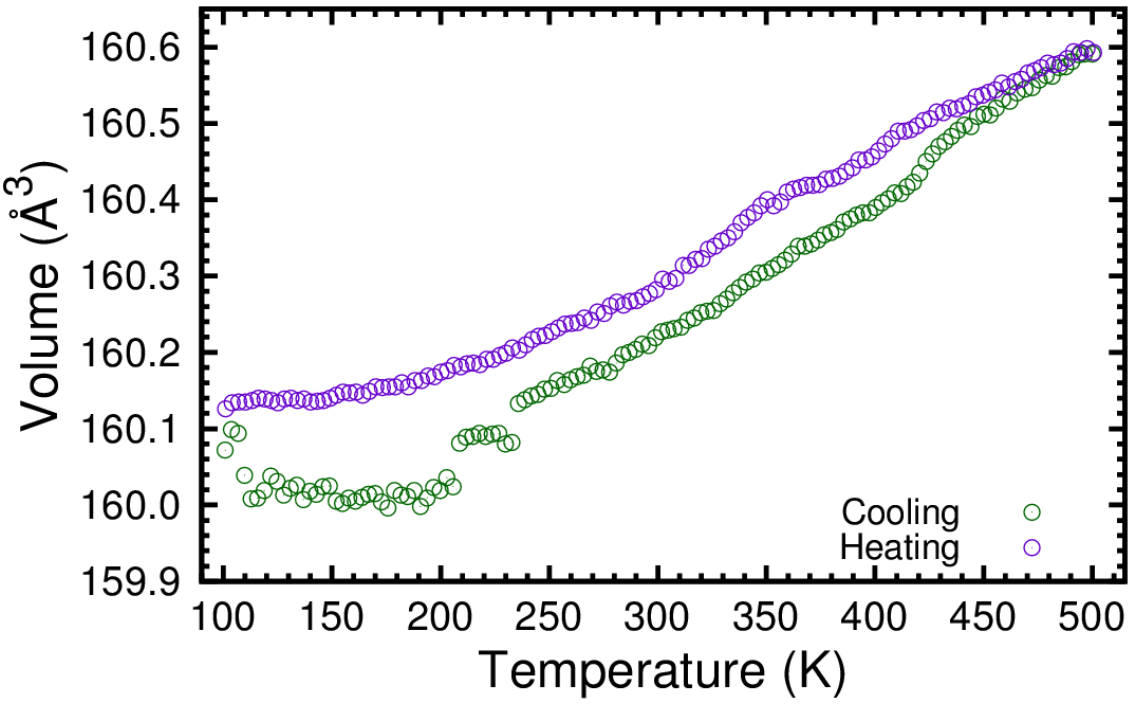

Figure 3.7: The unit cell volume of silicon is plotted versus temperature for CRYO-C_1.

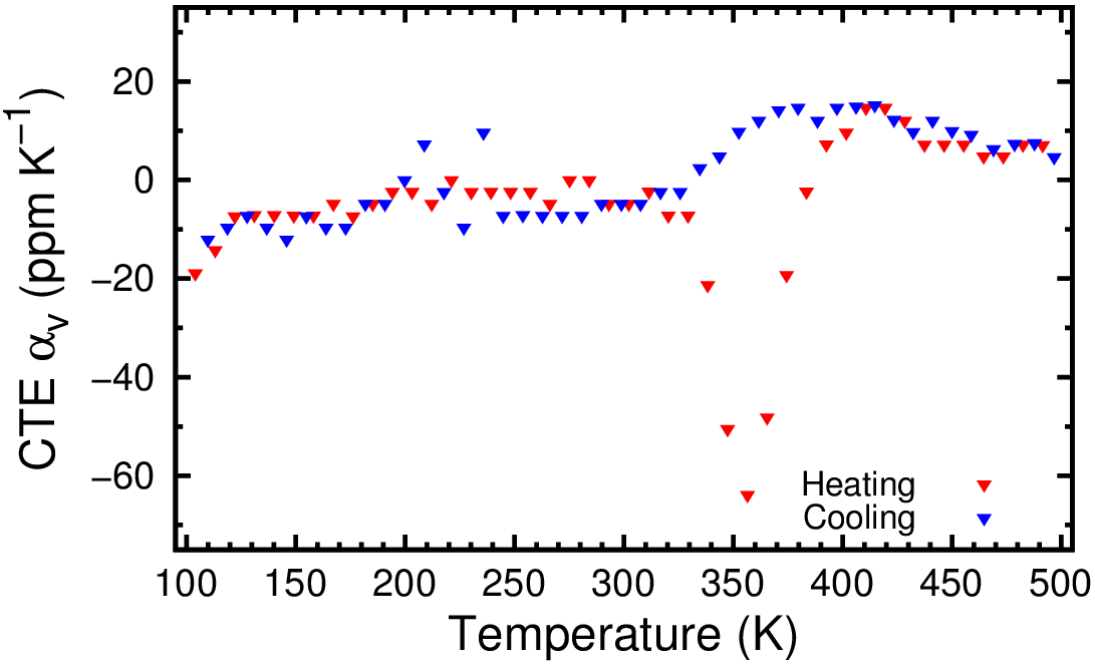

Figure 3.8: $YbZrF_7$ volumetric CTE values determined using every third point are plotted versus temperature for CRYO-C_1.

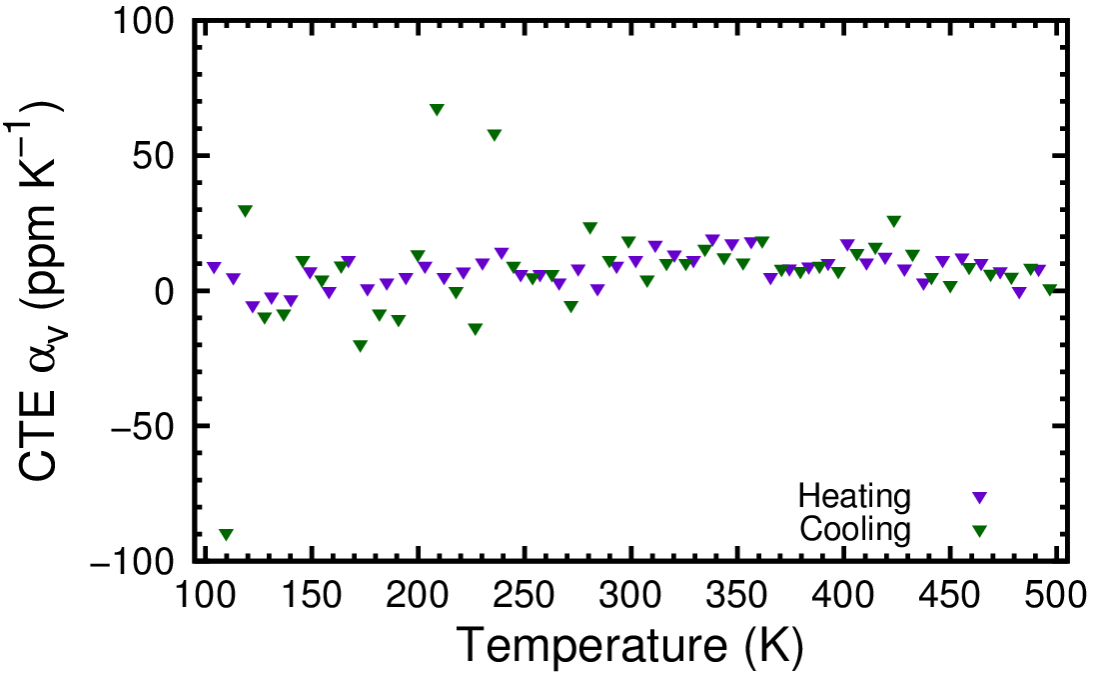

Figure 3.9: Silicon volumetric CTE values determined using every third point are plotted versus temperature for CRYO-C_1.

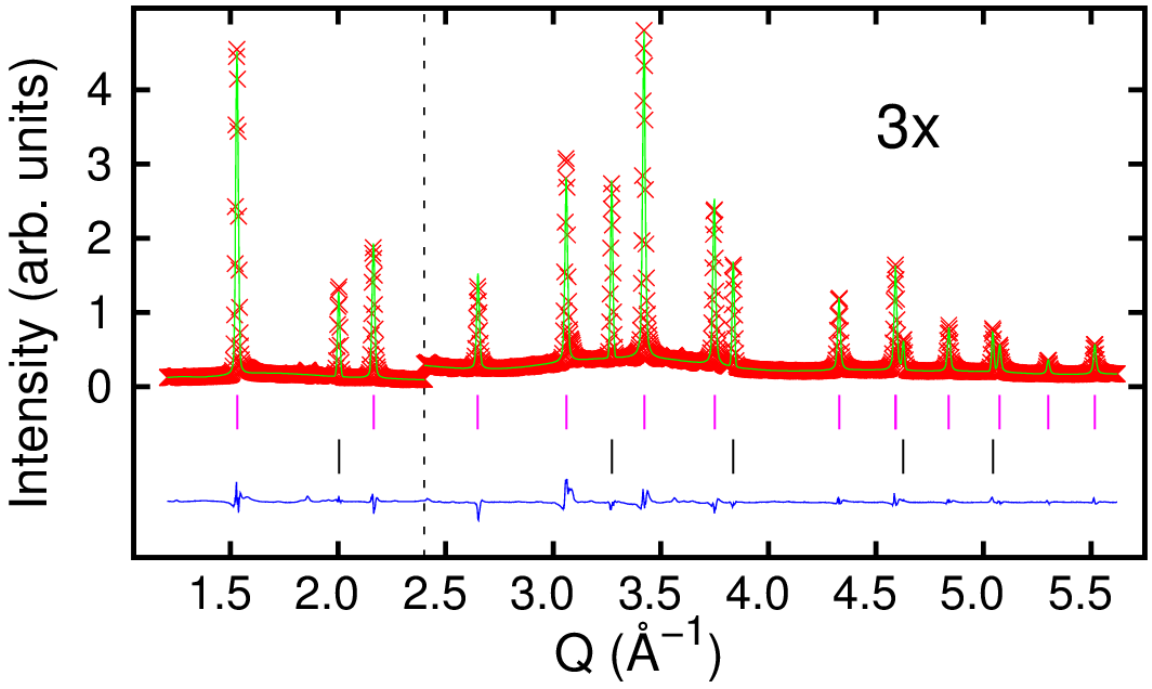

Figure 3.10: The initial CRYO-C_2 Rietveld fit at 299 K (green) is displayed in comparison to the original data, in red. Pink ($YbZrF_7$) and black (silicon) peak markers are indicated. The difference curve is shown in blue. High angle peaks are magnified.

At 299 K, the set of impurity peaks just before the first silicon peak became more prominent. These were indicative of trace amounts of unreacted YbF_3 and ZrF_4 [120-121]. Overlap of the highest intensity peaks in this region prevented impurity quantification. The overall quality of the Rietveld fit (**Figure 3.10**) was high, which lead to reasonable structural models for both $YbZrF_7$ (**Table 3.7**) and silicon (**Table 3.8**). Silicon showed no thermal history dependence on both heating and cooling, as shown in **Figure 3.12**. This was evident by the strong degree of overlap of the heating and cooling curves. At approximately 300 K, a sharp drop in synchrotron intensity was noted. This was reflected in both the silicon and the $YbZrF_7$ phases. In the case of $YbZrF_7$, thermal history dependence was repeated for CRYO-C_2. The overlap of the volume versus

temperature curves for $YbZrF_7$ was again observed near the temperatures of 100 and 500 K, as shown in **Figure 3.11**.

Table 3.7: Structural Model of $YbZrF_7$ Based on Initial Rietveld Fit at 299 K (CRYO-C_2)

Pm – 3m (Cubic)	**Fractional Coordinate (x)**	**Fractional Coordinate (y)**	**Fractional Coordinate (z)**
Yb (1)	0.000	0.000	0.060
Zr (1)	0.000	0.000	0.060
F (1)	0.500	0.052	0.052
F (2)	0.500	0.289	0.064
	Multiplicity	**Occupancy**	**Refined U_{iso} ($Å^2$)**
Yb (1)	6	0.0833	0.0177 (7)
Zr (1)	6	0.0833	0.0177 (7)
F (1)	12	0.2217	0.0353 (7)
F (2)	24	0.0325	0.0343 (7)
Refined Lattice Constant (Å)		4.10538 (9)	
Refined Unit Cell Volume ($Å^3$)		68.193 (5)	
X^2 (GSAS Fit)		6.708	

Table 3.8: Structural Model of Silicon Based on Initial Rietveld Fit at 299 K (CRYO-C_2)

Fd – 3m S (Cubic)	**Fractional Coordinate (x)**	**Fractional Coordinate (y)**	**Fractional Coordinate (z)**
Si (1)	0.125	0.125	0.125
	Multiplicity	**Occupancy**	**Refined U_{iso} ($Å^2$)**
Si (1)	8	1.000	0.022 (1)
Refined Lattice Constant (Å)		5.4289 (3)	
Refined Unit Cell Volume ($Å^3$)		160.01 (2)	
X^2 (GSAS Fit)		6.708	

Nearly zero volumetric CTE values closely overlapped in both heating domains at approximately 360 K. In contrast, the near zero CTE values on cooling were located near room temperature at approximately 305 K. This was in reasonable agreement to what was determined in the case of CRYO-C_1. As before, NTE was strongest on the first heating scheme between 305 and 370 K. The extent of NTE was not equally reflected in the case of the second heating scheme. The coefficients of thermal expansion were of approximately similar magnitude below 300 K on heating and cooling, as shown in **Figure 3.13**.

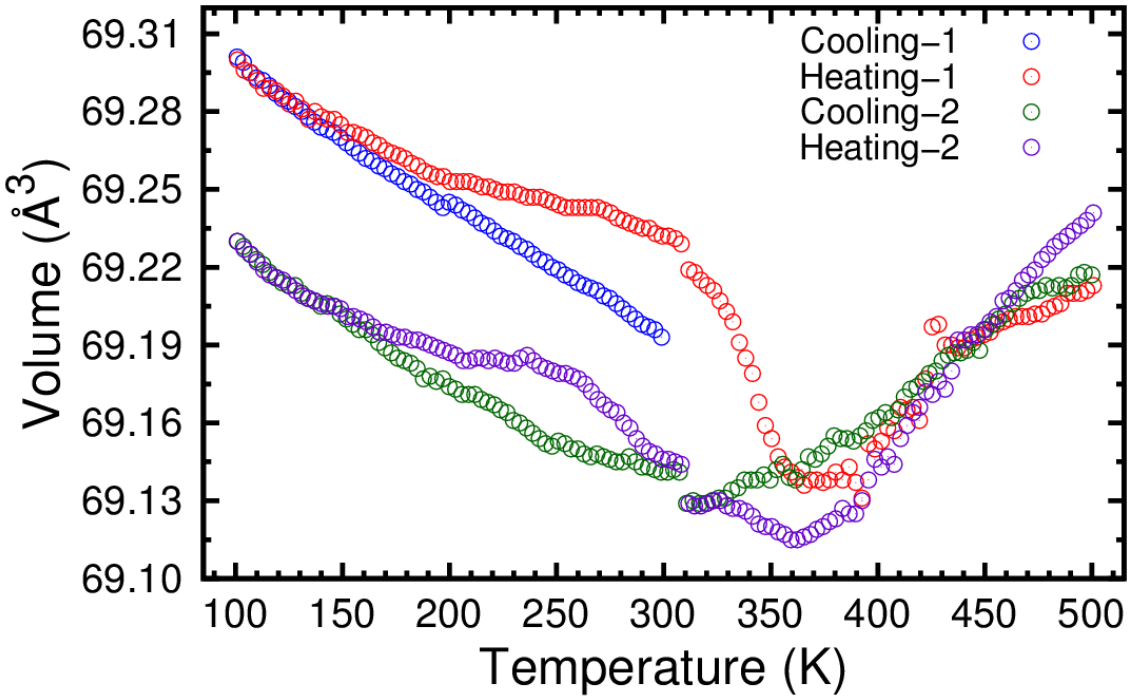

Figure 3.11: The unit cell volume of $YbZrF_7$ is plotted versus temperature for CRYO-C_2.

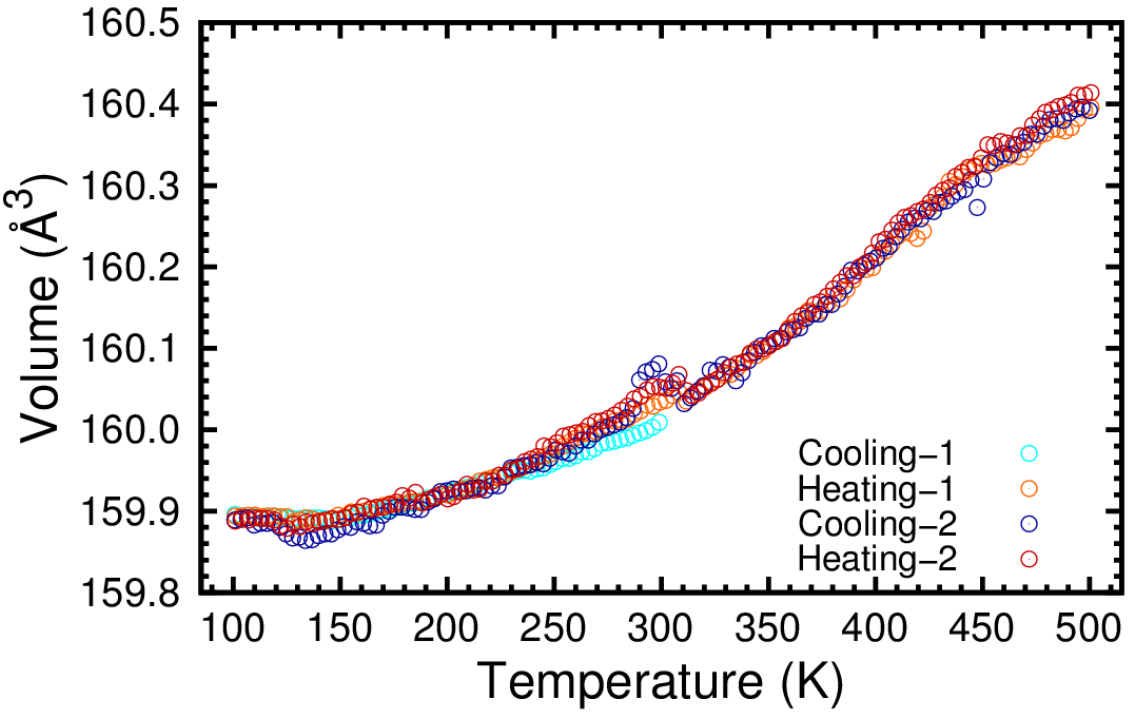

Figure 3.12: The unit cell volume of silicon is plotted versus temperature for CRYO-C_2.

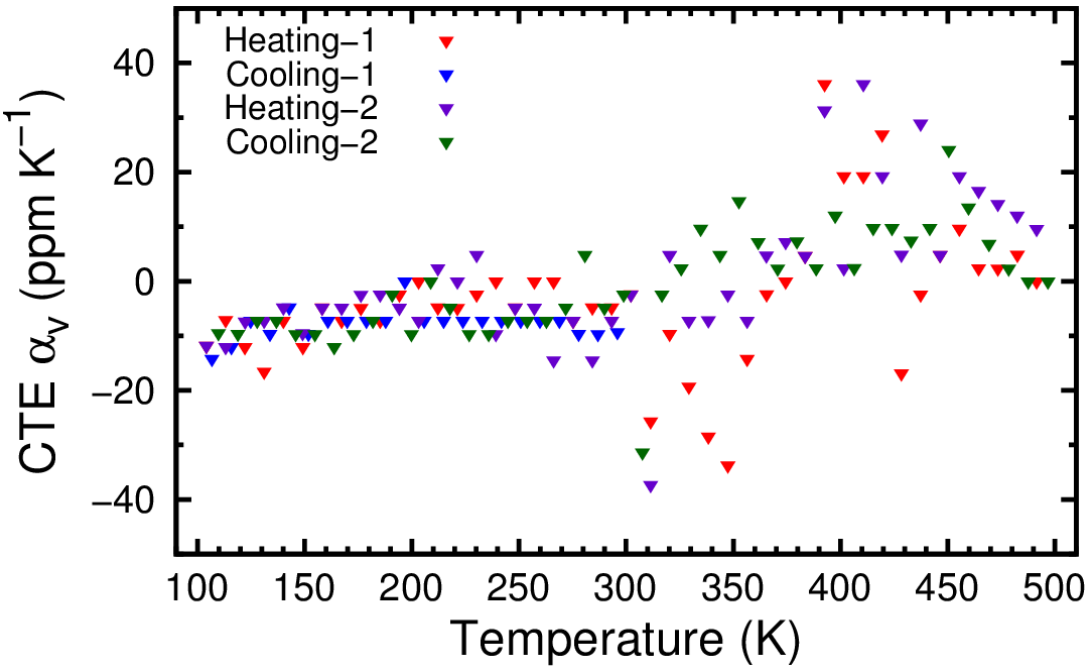

Figure 3.13: $YbZrF_7$ volumetric CTE values determined using every third point are plotted versus temperature for CRYO-C_2.

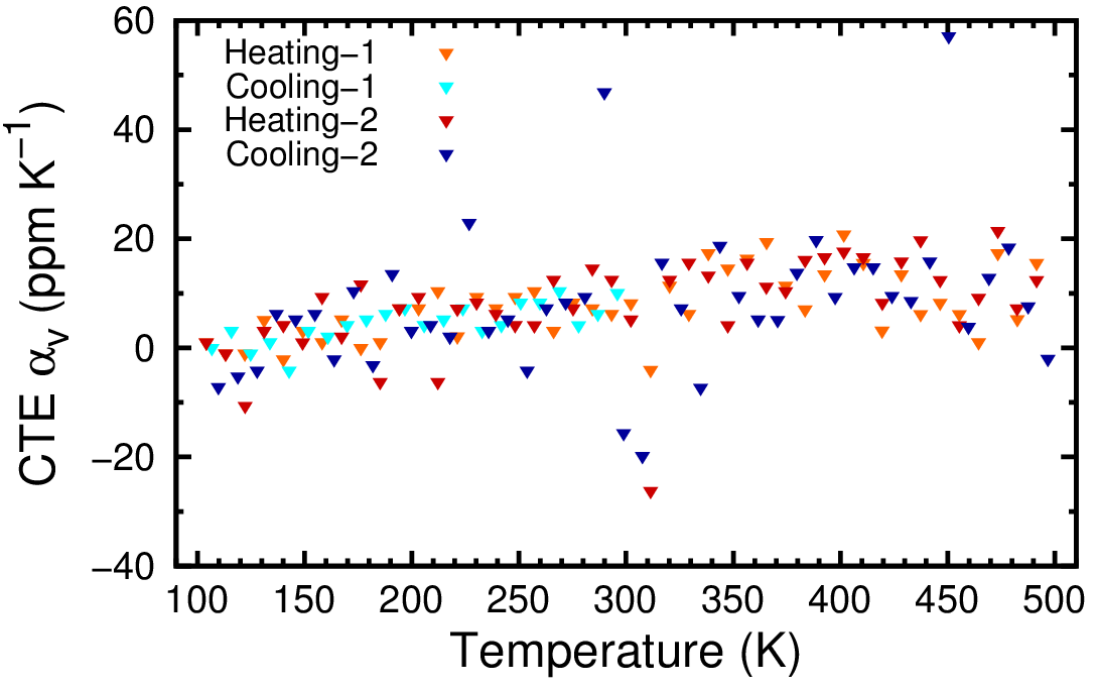

Figure 3.14: Silicon volumetric CTE values determined using every third point are plotted versus temperature for CRYO-C_2.

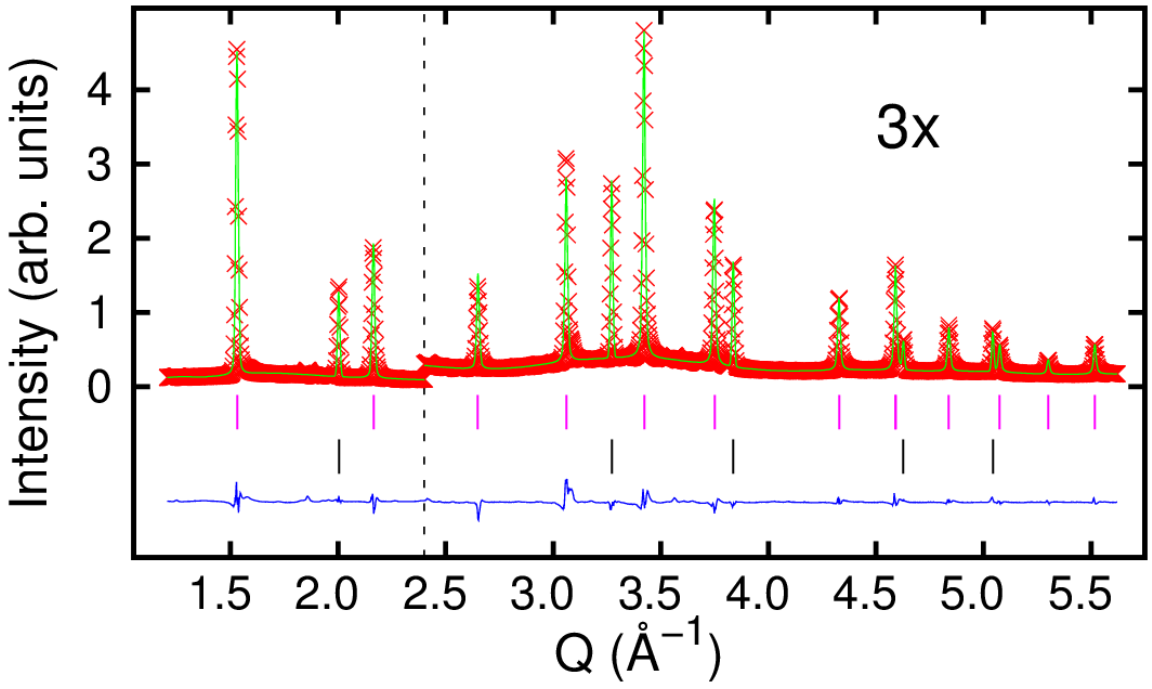

Figure 3.15: The initial CRYO-F Rietveld fit at 100 K (green) is displayed in comparison to the original data, in red. Pink ($YbZrF_7$) and black (silicon) peak markers are indicated. The difference curve is shown in blue. High angle peaks are magnified.

A Rietveld fit of high quality was obtained for CRYO-F synchrotron PXRD data, as shown in **Figure 3.15**. This generated a lattice constant for $YbZrF_7$, a = 4.10182 (6), which was in reasonable agreement to the previously experimentally determined lattice constants for $YbZrF_7$ at 100 K. $YbZrF_7$ again showed a thermal history dependence. As shown in **Figure 3.16**, $YbZrF_7$ behaved on cooling differently than on heating. As expected, silicon displayed no thermal history dependence (**Figure 3.17**), along with essentially equal volumetric CTE values in the case of heating and cooling (**Figure 3.19**). The volumetric CTE values of $YbZrF_7$ (**Figure 3.18**) were negative on both heating and cooling below 290 K, which was in agreement with the previously obtained results.

Table 3.9: Structural Model of $YbZrF_7$ Based on Initial Rietveld Fit at 100 K (CRYO-F)

Pm – 3m (Cubic)	**Fractional Coordinate (x)**	**Fractional Coordinate (y)**	**Fractional Coordinate (z)**
Yb (1)	0.000	0.000	0.060
Zr (1)	0.000	0.000	0.060
F (1)	0.500	0.052	0.052
F (2)	0.500	0.289	0.064
	Multiplicity	**Occupancy**	**Refined U_{iso} ($Å^2$)**
Yb (1)	6	0.0833	0.0064 (5)
Zr (1)	6	0.0833	0.0064 (5)
F (1)	12	0.2217	0.0240 (5)
F (2)	24	0.0325	0.0230 (5)
Refined Lattice Constant (Å)		4.10182 (6)	
Refined Unit Cell Volume ($Å^3$)		69.013 (3)	
X^2 (GSAS Fit)		4.898	

Table 3.10: Structural Model of Silicon Based on Initial Rietveld Fit at 100 K (CRYO-F)

Fd – 3m S (Cubic)	**Fractional Coordinate (x)**	**Fractional Coordinate (y)**	**Fractional Coordinate (z)**
Si (1)	0.125	0.125	0.125
	Multiplicity	**Occupancy**	**Refined U_{iso} ($Å^2$)**
Si (1)	8	1.000	0.010 (1)
Refined Lattice Constant (Å)		5.4297 (2)	
Refined Unit Cell Volume ($Å^3$)		160.07 (2)	
X^2 (GSAS Fit)		4.898	

Maximum NTE (~ - 12 ppm K^{-1}) was noted at approximately 340 K, although very similar values were identified at significantly lower temperatures approaching 100 K. Near zero CTE was again observed at different points on cooling versus heating. Near 500 K, the heating and cooling curves overlap, although not to the extent that was previously observed for other $YbZrF_7$ samples. Due to the extremely strong overlap between silicon heating and cooling curves, it was likely that all phenomena observed for $YbZrF_7$ could be linked directly to the expansion behavior of $YbZrF_7$ as opposed to possible experimental artifacts.

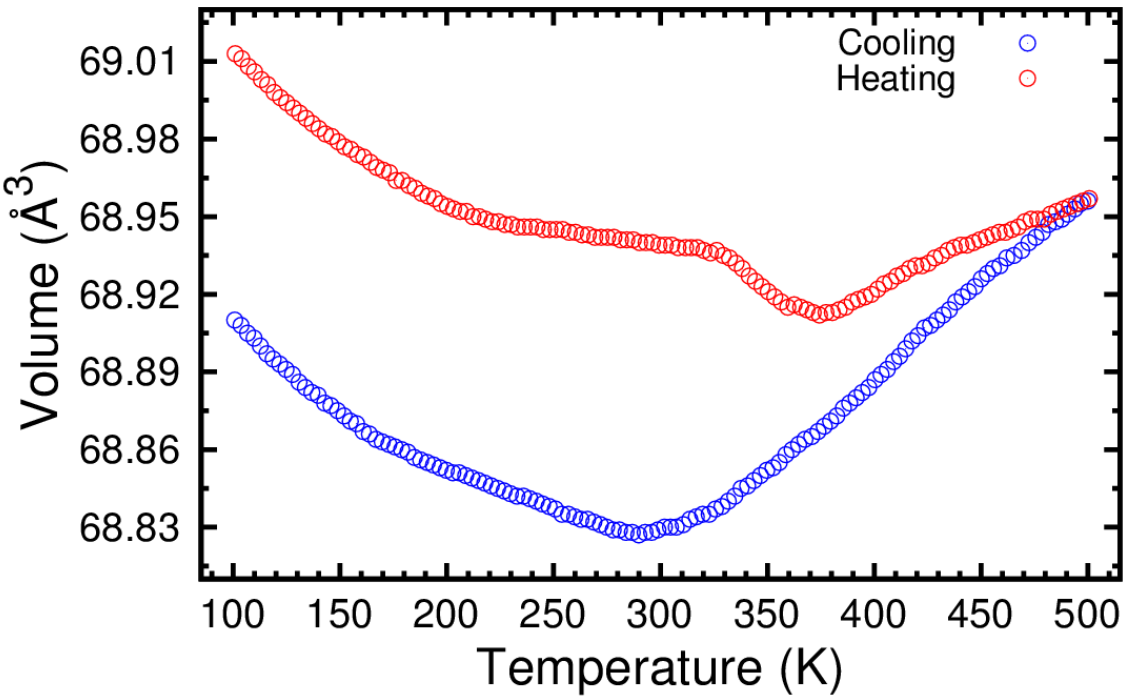

Figure 3.16: The unit cell volume of $YbZrF_7$ is plotted versus temperature for CRYO-F.

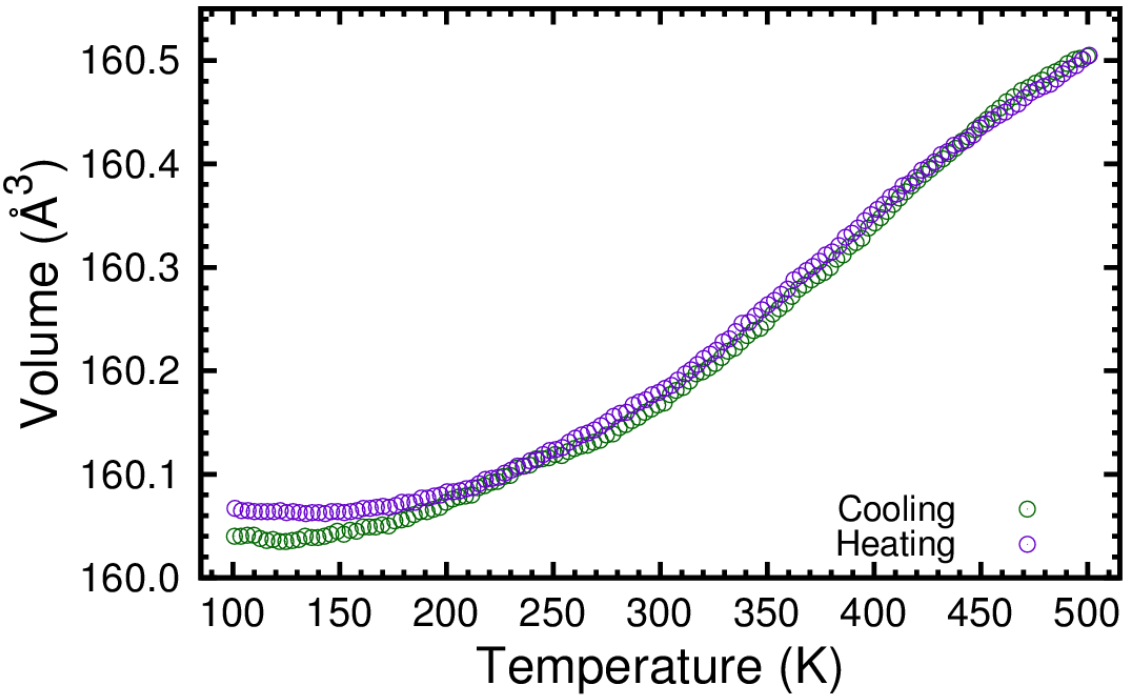

Figure 3.17: The unit cell volume of silicon is plotted versus temperature for CRYO-F.

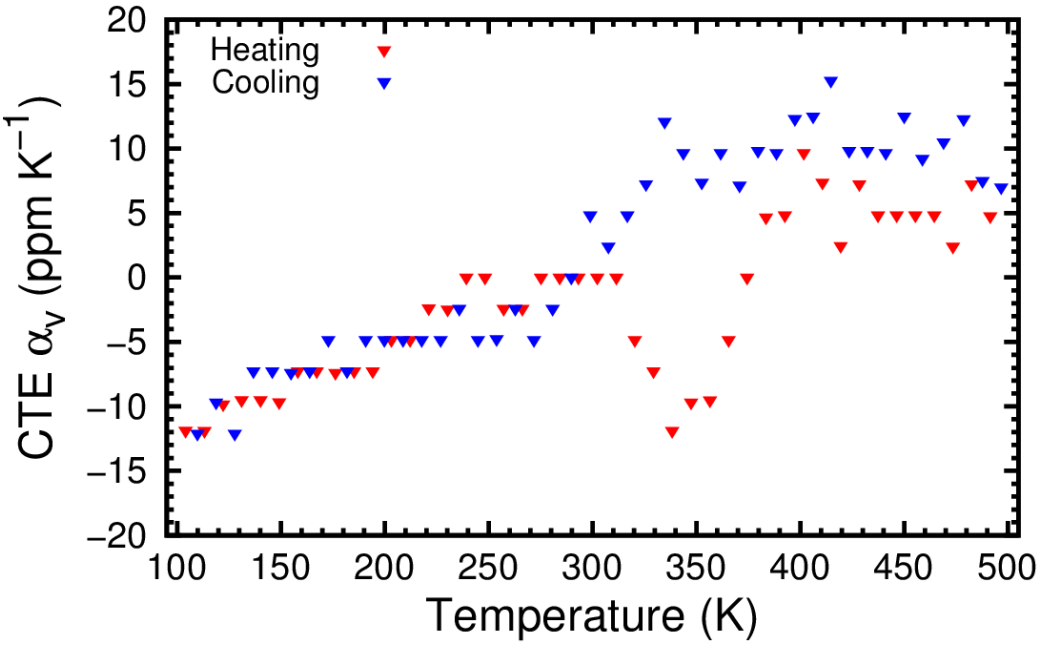

Figure 3.18: $YbZrF_7$ volumetric CTE values determined using every third point are plotted versus temperature for CRYO-F.

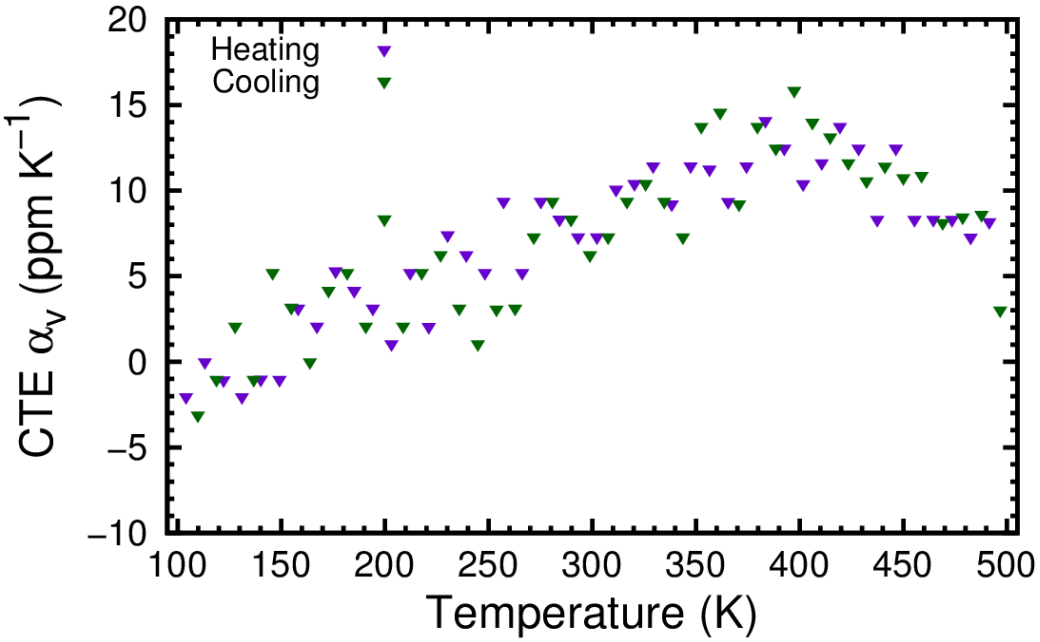

Figure 3.19: Silicon volumetric CTE values determined using every third point are plotted versus temperature for CRYO-F.

3.3.2 Furnace Enabled Synchrotron X-Ray Diffraction (304 – 1057 K)

The purpose of the FURN-D experiment was to better understand the behavior of $YbZrF_7$ at temperatures above 500 K. Analysis and discussion of the selected diffraction patterns will be restricted to a qualitative perspective, as no fit was applied due to complications arising from cubic and (presumed) monoclinic peak overlap.

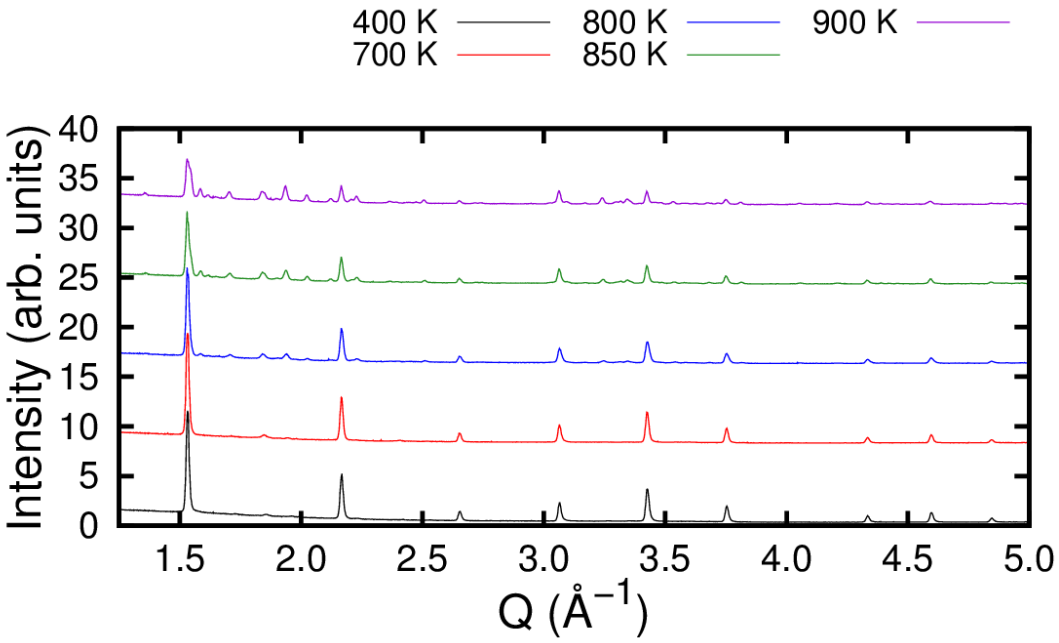

Figure 3.20: Diffraction patterns are shown at selected temperatures as $YbZrF_7$ undergoes a phase transition.

At 400 K, the sample is single phase cubic. This is shown in **Figure 3.20**, which shows the familiar set of cubic $YbZrF_7$ peaks for Q = 1.5 – 5.0 Å^{-1}. These peaks were in good agreement in terms of both peak position and intensity compared to cubic $YbZrF_7$ at 500 K, as displayed in **Figure 3.2**. As the temperature increases to 700 K, an additional peak

appears between Q = 1.5 and 2.0 $Å^{-1}$. Its position shifts slightly while its intensity increases at 800 K, along with the appearance of several more peaks. This trend continues to 850 K. It is presumed that these additional peaks are from monoclinic $YbZrF_7$. The initial cubic peaks are substantially reduced in intensity as this new phase appears. It is unlikely that within the time frame of the temperature ramp, a full conversion of $YbZrF_7$ has occurred. Thus, cubic $YbZrF_7$ most likely persists at 900 K. Absent a fit to the data; this secondary phase cannot be definitively attributed to monoclinic $YbZrF_7$.

3.4 Conclusions

The variable temperature behavior of cubic $YbZrF_7$ was successfully examined quantitatively between 100 and 500 K. The thermal history dependence of $YbZrF_7$ was most apparent, as it behaved differently on heating versus cooling. This was also reflected in the volumetric coefficients of thermal expansion, which were estimated on a point by point basis. This thermal history dependence is a consequence of how the material was synthesized. A quench from approximately 1300 K to 300 K allowed for the cubic structure to be retained. On heating from 100 to 300 K, the behavior is presumably a consequence of vibrational motion, as the material had to be cooled from room temperature. Above 300 K, a local structural change occurs, likely a result of the fluoride anions becoming mobile above room temperature. Once the material has been heated to 500 K, a more symmetric cooling curve is observed, as the structural relaxation seen on initial heating is not reversible. Slight differences in synthesis for each sample also produced minor differences in the material's expansion on heating and cooling, yet the overall trend was reproduced.

Near zero thermal expansion was typically noted on cooling near room temperature, whereas on heating it was commonly located near 370 K. For all $YbZrF_7$ samples that were verified by silicon acting as an internal reference, negative thermal expansion was observed below 280 K on heating and cooling. Above room temperature, $YbZrF_7$ shows NTE on heating within a small temperature range, typically between 310 and 360 K, which is most likely associated with a change in local structure. Above 500 K, cubic $YbZrF_7$ gradually undergoes a phase transition. This secondary phase was presumably monoclinic $YbZrF_7$ due to its stability at higher temperatures, although this was unconfirmed due to a lack of an available Rietveld fit. By 900 K, the presence of a secondary phase derived from $YbZrF_7$ is fully evident in the diffraction pattern.

CHAPTER 4

BEHAVIOR OF $YbZrF_7$ ON COMPRESSION

4.1 Introduction

It is often worthwhile to consider how a material behaves on compression. If the material is used in a composite where it is subject to stress, its pressure dependent behavior should ideally be well understood. Abundant research efforts have characterized the behavior of steel on compression, as this impacts how steel can be managed in civil engineering [122-124]. This may also reveal a material's limitations in applicability. This is especially true for materials involved in planetary research, where dramatic changes in both temperature and pressure can occur. For instance, if optical equipment is utilized for studies on Mars or Venus, the range of environmental conditions that it is exposed to must be considered. The surface of Venus maintains an atmospheric pressure of over 90 times the atmospheric pressure on Earth [125]. It must be ensured that the material can reliably operate in these conditions.

There exist other reasons as to why a material's compression behavior might be studied. Although they are perhaps less practical, they can often elucidate interesting or unusual properties. It may also assist in understanding how a material's structure can adapt. NTE materials, in particular, are known to adopt a diverse range of behavior on compression [61-62]. In some cases, the materials proceed from a distinct crystalline phase to another. In others, an ordered crystalline phase transforms to a material with no long range order,

resulting in amorphization. Both types of transitions are detectable by x-ray diffraction [84].

The majority of materials stiffen on compression. This is directly linked to the increase of interatomic repulsions as the atoms are forced closer together [61]. The isothermal bulk modulus (**Equation 4.1**) can be employed to quantify a material's resistance to compression [126].

$$K_T = -V\left(\frac{\partial P}{\partial V}\right)_T \approx -V\left(\frac{P - P_0}{V - V_0}\right) \qquad \mathbf{4.1}$$

The isothermal bulk modulus (K) accounts for the volume (V) and the first derivative of a pressure (P) versus volume (V) relationship at constant temperature. Bulk modulus at ambient temperature and pressure is commonly denoted by K_0. Analogous to examining temperature dependent behavior (**Chapter 3**), the unit cell volume can be determined by x-ray diffraction as a function of pressure. This allows calculation of an isothermal bulk modulus value, and it can be compared to other materials at the same temperature.

NTE materials are not just unusual in terms of their temperature dependent behavior, but also in relation to their behavior on compression. Softening on compression, as opposed to stiffening, is associated with a negatively valued K'. This is given in **Equation 4.2**.

$$K' = \frac{\partial K}{\partial P} \qquad \mathbf{4.2}$$

Pressure-induced softening has previously been observed in NTE materials. This includes ReO_3 type materials, such as $CaZrF_6$, $CaNbF_6$, and $MgZrF_6$ [61-62]. It might therefore be

reasonable to hypothesize that $YbZrF_7$ will also adopt pressure-induced softening. An unresolved question relates to how the anion excess component of $YbZrF_7$ will impact its overall behavior on compression.

There are numerous approaches available that can characterize a material's behavior on compression. For cubic $YbZrF_7$, a Diamond Anvil Cell (DAC) was selected for a variety of reasons. A depiction of this device is shown in **Figure 4.1**. In a DAC, the material is positioned within a metal gasket and it is compressed by the contact of two precision-crafted diamond surfaces. A pressure transmitting fluid is also required. The diamond surfaces are of extremely small surface area, and hence modest force can generate massive pressures on the order of several tens of GPa [127]. It must be emphasized that such pressures are not trivial, as 1 GPa is approximately 10,000 atmospheres. The DAC is a desirable choice due to its extremely wide working pressure range and also because it can be readily adapted for use in powder x-ray diffraction. A DAC can be assembled such that an x-ray beam can directly interact with the sample. This is crucial, as it allows for the behavior of $YbZrF_7$ on compression to be quantified in terms of its estimated unit cell volume and consequently its bulk modulus [128].

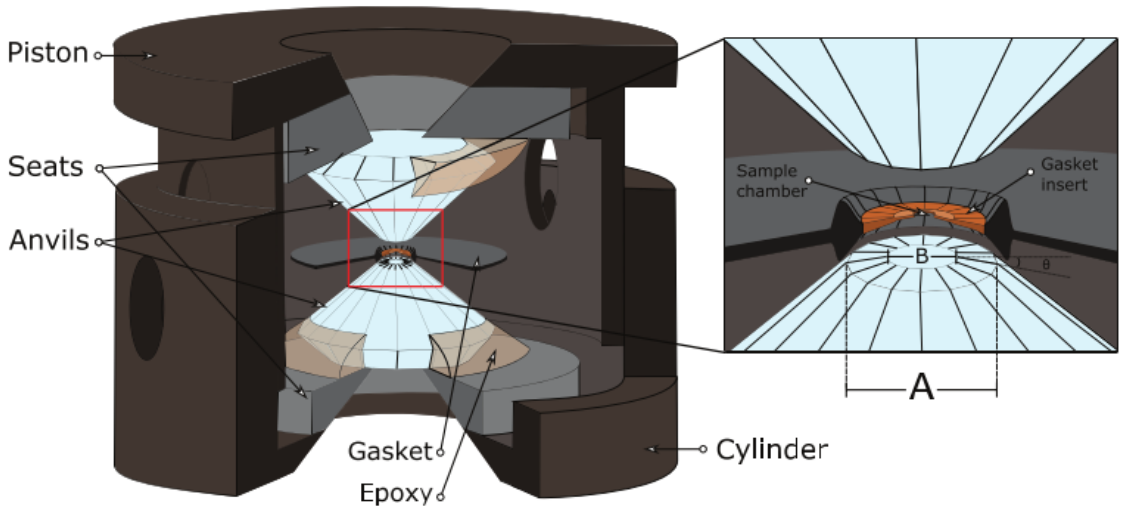

Figure 4.1: The typical configuration of a Diamond Anvil Cell is displayed. Relevant components are labeled. Within the sample chamber, a pressure-transmitting medium is required. Reprinted with permission from G. Shen et al. *Rep. Prog. Phys.,* 80, 1-53, 2017. Copyright 2017, IOP Publishing [127].

4.2 Experimental Methods and Materials

A variable pressure synchrotron x-ray experiment was performed at the Advanced Photon Source, sector 17-BM (λ = 0.72950 Å). The sample was compressed in a Diacell Bragg-(G) Diamond Anvil Cell (DAC). Sufficient cubic $YbZrF_7$ (sample **A**) was combined with pure NaCl within a sealed, inert atmosphere glove bag. NaCl served as an internal reference for determining the pressure within the DAC. The NaCl unit cell volume estimated from diffraction measurements could be substituted into a pressure-volume equation of state developed by Francis Birch [129]. The prepared $YbZrF_7$-NaCl mixture was thoroughly ground. This mixture was loaded into the DAC and silicone oil (Alfa Aesar, 237 g mol^{-1}) added. The silicone oil served as the pressure transmitting medium. The sample was then continuously compressed within the DAC while simultaneously detecting x-ray diffraction intensity.

By integrating the individual 2D diffraction patterns using the software program GSAS-II, a set of GSAS-readable files (.fxye) was generated [130]. In GSAS, two phases were used: cubic $YbZrF_7$ and NaCl. The $YbZrF_7$ phase was fit using a model adapted from the work Poulain, et. al. [72]. The NaCl phase was fit using a model from Cherginets, et. al. [131]. An initial fit to the first diffraction pattern (ambient pressure) was obtained in GSAS using optimized parameters and refined settings for $YbZrF_7$ (**Table 4.1**, **Table A.19**) and NaCl (**Table 4.2**, **Table A.20**). Note that $YbZrF_7$ made use of a Von Dreele-type Le Bail fit whereas NaCl was fit using a Rietveld method [130].

Three separate sequential GSAS operations were performed based on the initial results from the fit, as shown in **Table 4.3**. This was due to divergence of fits following a certain pressure. This was primarily corrected by modifying the background function. Additional changes to the GSAS parameters from the initial fit to the sets of sequential fits are noted in **Table A.21**.

Unit cell volumes for $YbZrF_7$ and NaCl were estimated at 46 pressures based on fits to the diffraction patterns. The NaCl unit volumes were substituted into the Birch isothermal equation of state to determine the pressure [129]. The unit cell volumes of $YbZrF_7$ were then plotted as a function of applied pressure as shown in **Figure 4.2** using EoSFit7 [132-133]. A third order Birch-Murnaghan equation of state was fit to these data to obtain estimates of V_0, K_0, and K_0' given in **Table 4.4**.

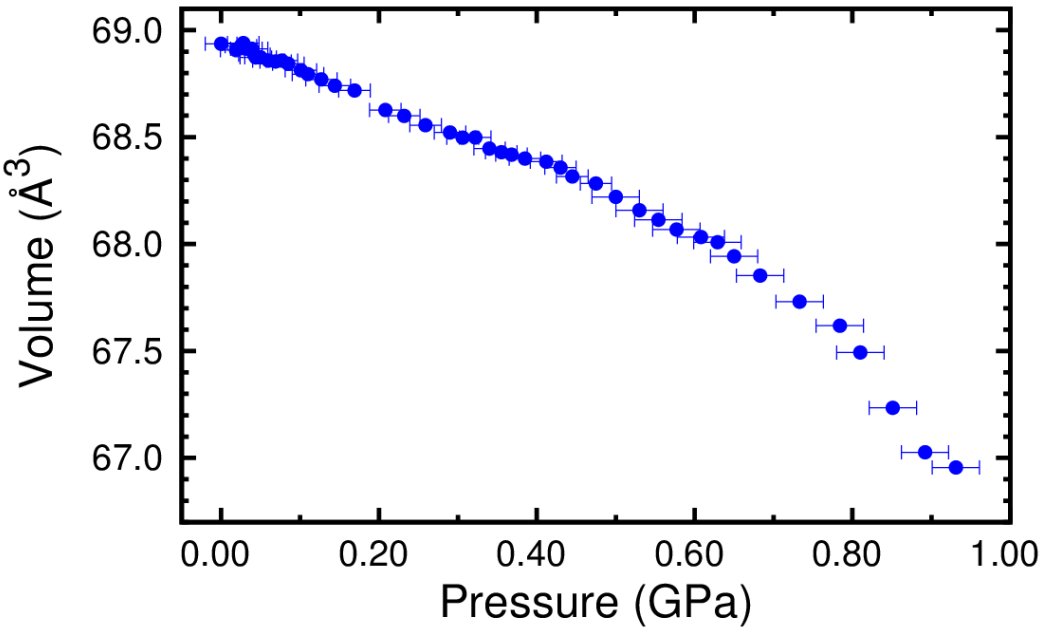

Figure 4.2: The unit cell volume of $YbZrF_7$ versus applied pressure along with corresponding one-sigma error bars.

4.3 Results and Discussion

In total, 46 x-ray diffraction patterns were fit to a model from 0.00 to 0.93 GPa. Pressures above 0.93 GPa could not be fit due to the emergence of an amorphous $YbZrF_7$ phase. Above this point, pressures were estimated using NaCl unit cell volumes. All fits for pressures above 0 GPa were based upon the initial model for 0 GPa. Slight modifications were made to the model as noted in **Table A.21** in order to generate converged fits.

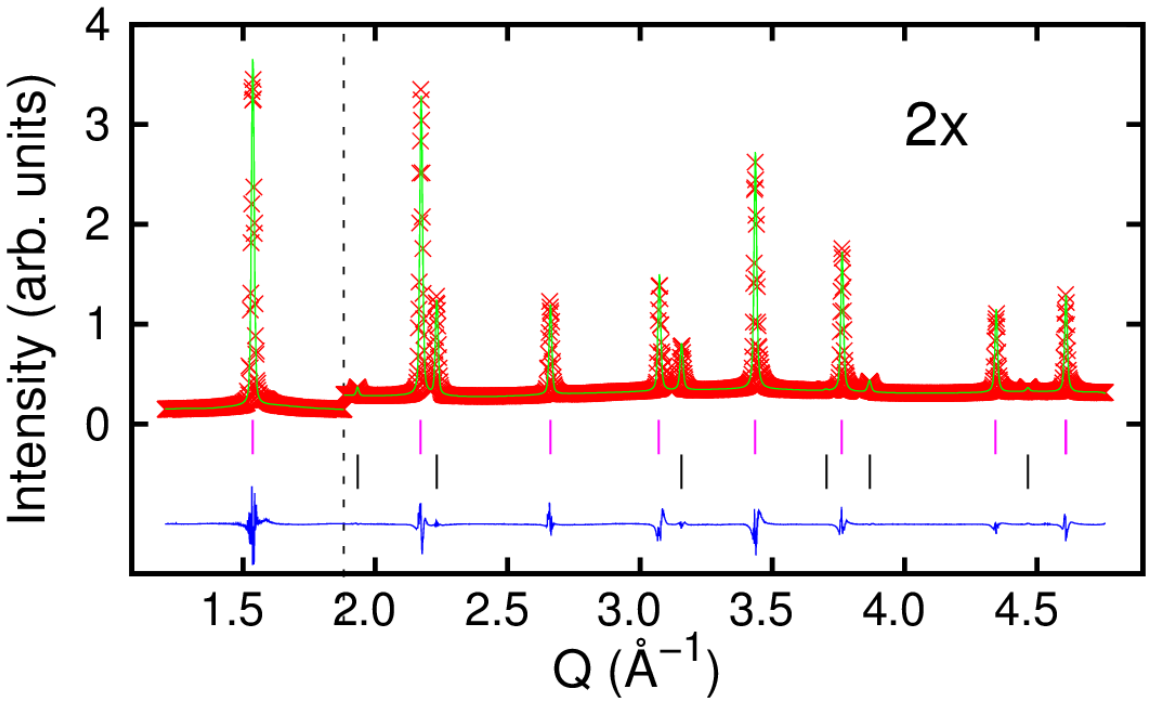

Figure 4.3: The initial Von Dreele-Type Le Bail and Rietveld fits (green) at 0 GPa for $YbZrF_7$ and NaCl respectively are compared to the diffraction pattern, in red. Peak markers for $YbZrF_7$ (pink) and NaCl (black) are also shown. The difference curve is displayed in blue. High angle peaks are magnified.

The initial fit (**Figure 4.3**) was of high quality, as given by an R-factor of 0.0592. This stemmed from excellent fit agreement with the peak positions and intensities. The

$YbZrF_7$ and NaCl peaks were well resolved, facilitating the use of NaCl as a pressure calibrant.

Table 4.1: Structural Model of $YbZrF_7$ Based on Initial Fit at 0 GPa [72]

Pm – 3m (Cubic)	**Fractional Coordinate (x)**	**Fractional Coordinate (y)**	**Fractional Coordinate (z)**
Yb (1)	0.000	0.000	0.060
Zr (1)	0.000	0.000	0.060
F (1)	0.500	0.052	0.052
F (2)	0.500	0.289	0.064
	Multiplicity	**Occupancy**	**Refined U_{iso} ($Å^2$)**
Yb (1)	6	0.0833	0.01552 (-)
Zr (1)	6	0.0833	0.01552 (-)
F (1)	12	0.2217	0.03312 (-)
F (2)	24	0.0325	0.03211 (-)
Refined Lattice Constant (Å)		4.10033 (9)	
Refined Unit Cell Volume ($Å^3$)		68.937 (4)	
X^2 (GSAS Fit)		7.119	

Table 4.2: Structural Model of NaCl Based on Initial Rietveld Fit at 0 GPa [131]

Fm – 3m (Cubic)	**Fractional Coordinate (x)**	**Fractional Coordinate (y)**	**Fractional Coordinate (z)**
Na (1)	0.000	0.000	0.000
Cl (1)	0.500	0.500	0.500
	Multiplicity	**Occupancy**	**Refined U_{iso} ($Å^2$)**
Na (1)	4	1.000	0.045 (5)
Cl (1)	4	1.000	0.045 (5)
Refined Lattice Constant (Å)		5.641 (1)	
Refined Unit Cell Volume ($Å^3$)		179.5 (1)	
X^2 (GSAS Fit)		7.119	

Table 4.3: Sequential GSAS Operations and Their Respective Pressure Ranges

Sequential GSAS #	**Pressure Range (GPa)**	**Number of X-Ray Diffraction Patterns**
1	0.00 – 0.29	22
2	0.31 – 0.81	21
3	0.85 – 0.93	3

The cubic $YbZrF_7$ lattice constant obtained from the initial Rietveld model, a = 4.1033 (9) Å, was in excellent agreement with previous laboratory and synchrotron measurements. The lattice constant of NaCl, a = 5.641 (1) Å estimated from the initial Rietveld model for NaCl very closely matched the published data of Cherginets, et. al [131].

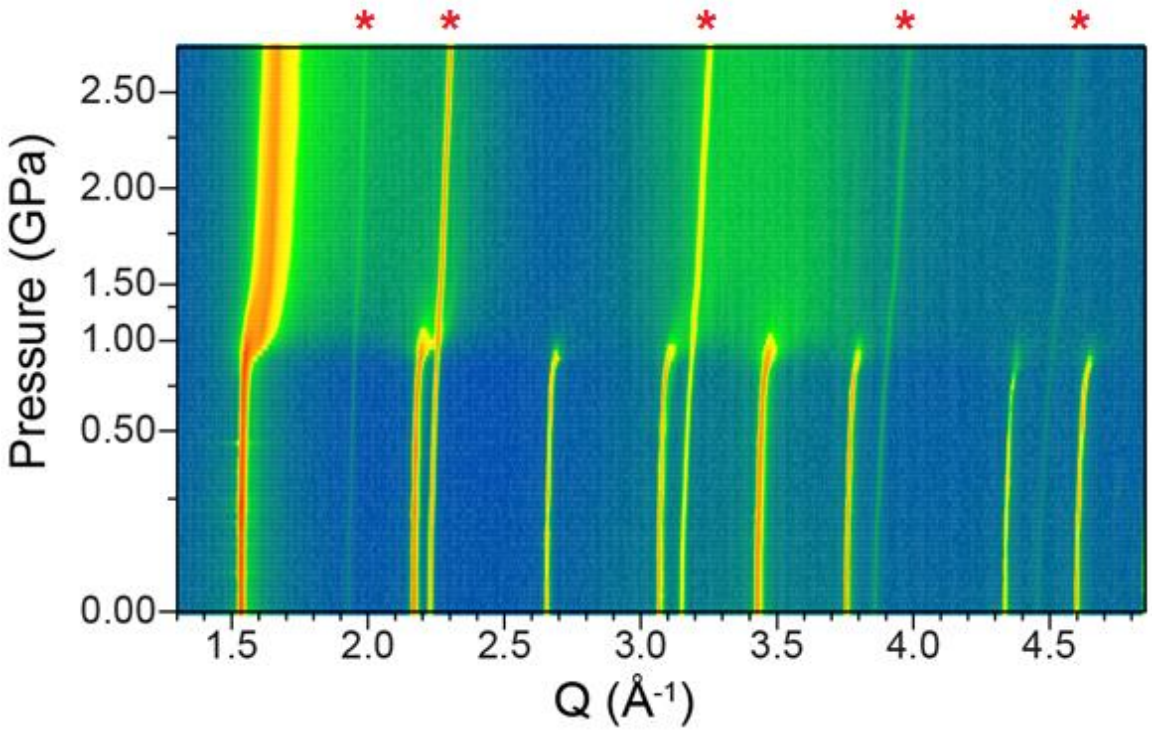

Figure 4.4: $YbZrF_7$ and NaCl diffraction patterns are shown as a function of pressure. On compression, the NaCl peaks (*) persist at high pressure.

As cubic $YbZrF_7$ was compressed, it remained cubic until approximately 0.90 GPa. This was clear from the contour plot, as shown in **Figure 4.4**. The intensity of the higher angle peaks above Q = 1.6 Å abruptly collapsed to nearly zero, whereas the first cubic $YbZrF_7$ peak was transformed to a broader peak indicative of a rapidly emerging amorphous

phase. This was also apparent in **Figure 4.5**, where the NaCl peaks persist past the point of $YbZrF_7$ amorphization.

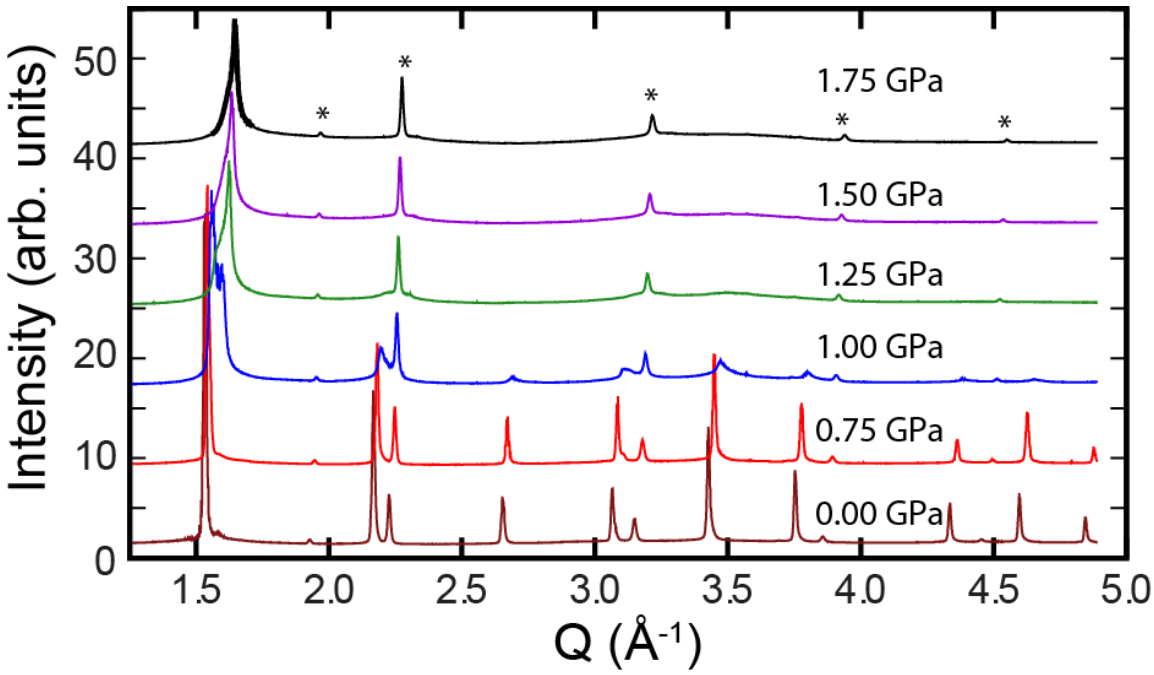

Figure 4.5: Diffraction patterns for $YbZrF_7$ at designated pressures are shown. NaCl peaks (*) are marked.

The amorphization behavior observed for this material was highly unusual. Phase transitions involving amorphization are often associated with kinetic barriers, and thus they may be expected to occur more gradually. For example, $Ca(OH)_2$ undergoes a phase transition to a glass over a broad pressure range between 10.7 and 15.4 GPa [134]. In this case, the cubic $YbZrF_7$ became disordered abruptly. The pressure range for the phase transition was determined to be less than 0.5 GPa, as shown in **Figure 4.5**. Above 1.50 GPa, there was no detectable cubic $YbZrF_7$. Also, cubic $YbZrF_7$ amorphized at a modest pressure of 0.9 GPa, which appeared reasonable compared to $CaZrF_6$, which begins to

disorder at 0.4 GPa [61]. In contrast, $CaNbF_6$ amorphized at pressures above 4 GPa [62]. This might imply that the presence of zirconium and its affinity for higher coordination influences this pressure-induced amorphization.

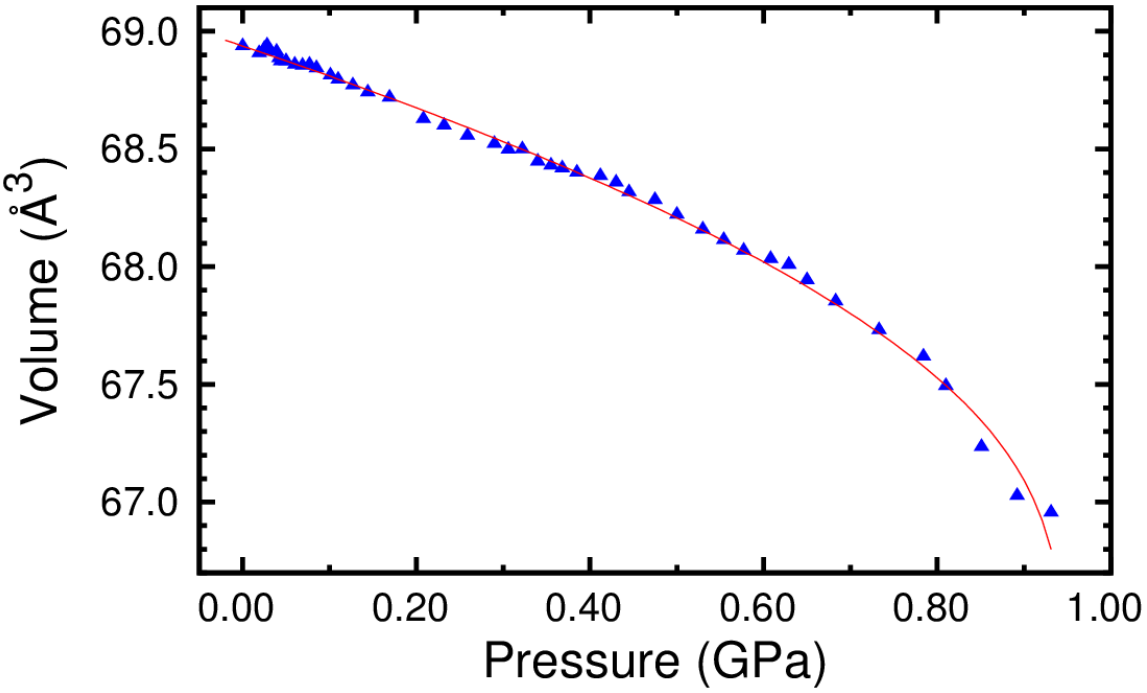

Figure 4.6: $YbZrF_7$ pressure-volume data is fit to a third order Birch-Murnaghan equation of state [133].

The Birch-Murnaghan isothermal equation of state provided a reasonable fit to the pressure-volume dependence of $YbZrF_7$ between 0 and 1 GPa, as shown in **Figure 4.6** [133,135]. The quality of fit was excellent at low pressures, although this was not true at pressures near amorphization. The estimated isothermal bulk modulus (K_0) of approximately 55 GPa is comparable in magnitude to other ReO_3-type fluorides such as ScF_3 and $CaZrF_6$ with isothermal bulk moduli of 60 and 42 GPa respectively [61,136]. The first derivative of bulk modulus (K_0') was found to be approximately – 28, indicative

of pronounced pressure-induced softening. This was not an unexpected result, as ReO_3-type NTE materials have been known to display this rare behavior [61].

Table 4.4: EoSFit Derived Isothermal Bulk Moduli Data for $YbZrF_7$ [133]

Initial Volume Unit Cell Volume, V_0 ($Å^3$)	68.937 (5)
Isothermal Bulk Modulus, K_0 (GPa)	55.4 (7)
Bulk Modulus First Derivative, K_0'	- 27.7 (6)
K_{pp} (GPa^{-1})	- 17.6

4.4 Conclusions

Cubic $YbZrF_7$ persists on compression at room temperature until approximately 0.9 GPa, where the material abruptly amorphizes. It was suggested that this abrupt amorphization was a consequence of zirconium and its ability to readily adopt higher coordination number. This order to disorder transition was indicated by the disappearance of diffraction intensities characteristic of cubic $YbZrF_7$ immediately followed by the emergence of a single broad peak at Q = 1.6 $Å^{-1}$. 46 diffraction patterns were collected at nearly even pressure intervals between 0 GPa and 0.93 GPa. The pressure within the DAC device was calculated by the Birch equation of state for the internal reference, NaCl [129]. An isothermal bulk modulus was subsequently determined for $YbZrF_7$ of approximately 55 GPa, which is reasonable in comparison to similar materials such as

$CaZrF_6$ [61]. The negative value of K_0' (- 28) was evidence of pronounced pressure induced softening. This unusual phenomenon has been well established in ReO_3-type NTE materials.

CHAPTER 5

STABILITY OF $YbZrF_7$

5.1 Introduction

If there is interest in a material's applicability, it is worthwhile to consider how it performs under a broad range of different conditions. $YbZrF_7$ has thus far been characterized in terms of its anomalous thermal expansion and its behavior on compression. Such phenomena depend primarily on structure at the atomic level. It has been shown that if local or long-range structural changes occur, they can profoundly influence the material's properties. In some cases, it may not be necessary to consider what takes place at an atomic level. This may concern a particular change in the material that will not be fully resolved through x-ray diffraction or other similar characterization methods. A comprehensive description of a material must involve some understanding of its macroscopic behavior.

In fluorozirconates, oxide impurities are a major area of study. This process involves the substitution of some of the fluoride anions with oxide anions. The presence of oxide defects can dramatically affect the optical properties of fluorozirconate glass materials, often reducing their infrared transparency [137-138]. It is therefore of interest as to how readily oxygen can be incorporated into the structure of $YbZrF_7$ at certain temperatures. Anydrous fluoride melts have not only been proposed to react with oxides, but also to thermally decompose [139].

These materials may also react with moisture. It is known that fluorides (in general) can produce hydrofluoric acid when exposed to water [110]. Additionally, $MgZrF_6$ has been shown to form a dihydrate when kept in air for a significant amount of time [140]. Air contains some water, and thus there are concerns regarding air stability in fluorozirconates. It has been reported that $CaZrF_6$ may be handled in air [61]. It is of interest as to how exactly $YbZrF_7$ reacts with moisture. The rate of reaction, specific products formed, and the effect of varying relative humidity are all of importance.

Thermogravimetic analysis (TGA) is an extremely capable and versatile technique that can identify how a material responds to different environmental settings [141]. This obviously includes temperature, but also the influence of moisture, air, or reactivity to a specific substance. TGA relies on a material's change in weight when exposed to these conditions. Essentially, a sample is contained within a metal pan which is suspended in a precision balance. This pan can be subjected to heating or cooling, as it is contained within a temperature controlled furnace. Sample amounts are typically between 2 and 50 mg, with a precision of approximately 1 μg. As the material is exposed to a desired condition, its weight changes can be followed as a function of temperature or time [142].

TGA can characterize how $YbZrF_7$ responds to high temperatures in addition to moisture at ambient conditions. It is also ideal due to the small sample amount needed. It may provide an indication of its ability to undergo hydrolysis at either room temperature or elevated temperatures. For instance, absorption of moisture would be clearly indicated by an increase in sample weight. The focus of inquiry surrounds possible thermal decomposition of $YbZrF_7$ in addition to its moisture and oxygen sensitivity.

5.2 Experimental Methods and Materials

All TGA experiments made use of a Perkin Elmer TGA 7 connected to a Perkin Elmer 7/DX Thermal Analysis Controller. Method preparation and data acquisition utilized the Perkin Elmer Pyris software. The balance was twice calibrated using N.B.S. Circular 547 Class M weights of 5.000 and 10.000 mg. Sample temperature calibration was performed using a calcium oxalate standard. Prior to all measurements, the pan was dried for at least 30 minutes in a 100 °C oven. Residual organic material within the furnace was removed by heating the furnace to approximately 900 °C for one hour. The overall TGA apparatus is shown in **Figure 5.1**. Specific components are highlighted and described in **Figure 5.2**.

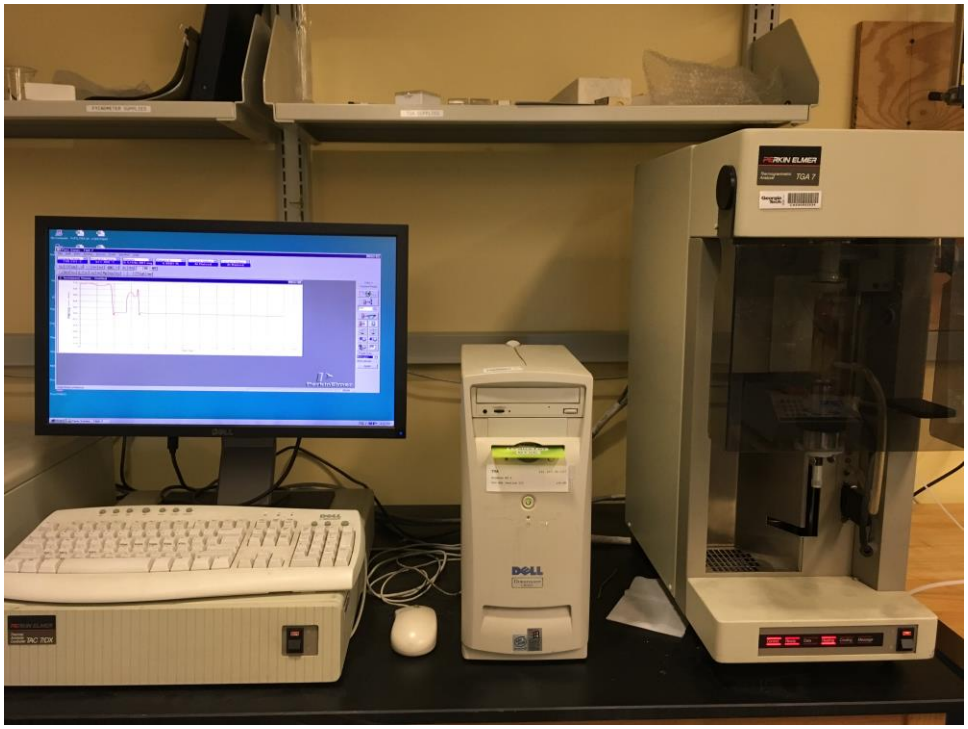

Figure 5.1: In a typical TGA setup, the main apparatus (far right) is linked to a computer display (far left) where data analysis can be performed. Communication between the computer and TGA apparatus allow for desired operations to take place.

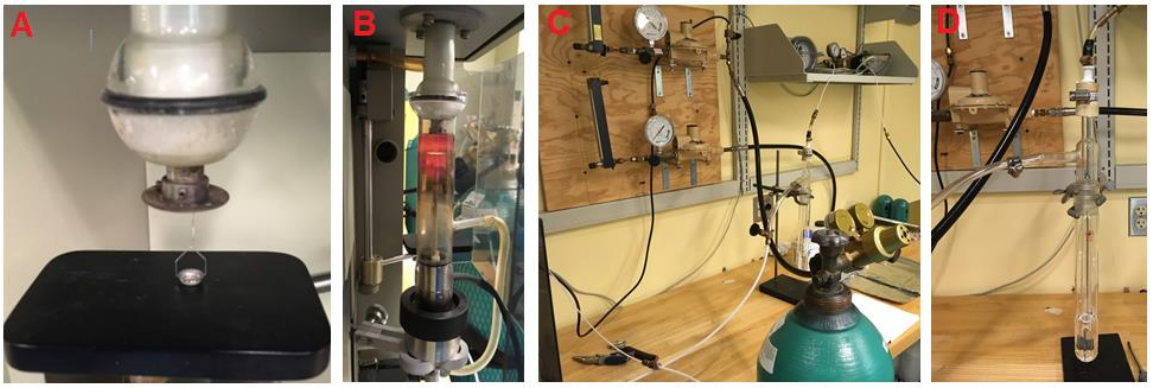

Figure 5.2: In the TGA apparatus, a platinum pan is connected by a platinum stirrup to a precision balance in A. In B, the pan is removed from the black platform in A and held in a furnace, which is sealed in a glass vessel. Within this vessel, gas (C) can be flowed in. A gas bubbler (D) allows for dry air to be flowed through a saturated salt solution such that moist air of known relative humidity can be used.

5.2.1 Thermal Decomposition of $YbZrF_7$

A platinum pan was tared to zero weight on the TGA balance. The pan was then transferred to an inert nitrogen atmosphere glovebox. A small amount of cubic $YbZrF_7$ (sample **G**) was added to the pan. The sample was sealed in a plastic container and removed from the glovebox. The sample was immediately placed onto the stirrup and sealed within the TGA apparatus. The sample chamber was flushed with nitrogen. After several minutes, the system was set to 100 % weight. The furnace temperature was controlled according to the parameters given in **Table 5.1**. The sample temperature closely followed the programmed temperature, as highlighted in **Figure 5.3**. An identical procedure was also performed for an impure sample of monoclinic $YbZrF_7$, sample **H**. A weight baseline correction was not applied, as the changes in weight observed for thermal decomposition overwhelmed the magnitude of baseline drift. Weight was measured once every second.

Table 5.1: Thermogravimetric Analysis Heating and Cooling Schedule for Studying Thermal Decomposition of Cubic and Monoclinic $YbZrF_7$

Samples	Stage 1	Stage 2	Stage 3	Stage 4	Stage 5
G and **H**	30 °C	30 → 900 °C	900 °C	900 → 30 °C	30 °C
Duration	10 minutes	29 minutes	30 minutes	29 minutes	10 minutes
Rate	---	30 °C min^{-1}	---	30 °C min^{-1}	---

5.2.2 Air and Moisture Stability of Cubic $YbZrF_7$

A Phillips X'Pert MPD Powder Diffractometer (Cu $K_{\alpha1}/K_{\alpha2}$ radiation) was used to record an x-ray diffraction pattern for cubic $YbZrF_7$ (sample **G**), which had previously been stored in an inert nitrogen atmosphere. The sample was then exposed to ambient air for 24 hours. Using the same sample, a second (comparative) x-ray diffraction pattern was recorded. In both cases, the sample was covered by a Kapton film while the diffraction pattern was recorded. This sample was again exposed to ambient air at 30 °C and its baseline corrected weight was monitored for 24 hours at 5 minute intervals. After 24 hours, the sample was heated to 120 °C in order evaporate any produced HF. This allowed for an approximation as to how much moisture was absorbed by the sample.

Cubic $YbZrF_7$ (sample **G**) was loaded onto a pre-tared TGA pan within an inert nitrogen atmosphere glovebox. The sample was sealed within a plastic vial and removed from the glovebox. The pan was placed onto the TGA stirrup and the apparatus was closed. The TGA system was immediately flushed with dry-grade air of approximately zero percent

humidity for 30 minutes. The sample was then heated to 300 °C over 9 minutes at a rate of 30 °C per minute. The dry air flow was promptly ceased after an additional 21 minutes at 300 °C. After 10 minutes, the sample was exposed to moist air of known relative humidity. This was accomplished by bubbling dry air through a vessel containing an aqueous saturated salt solution held at approximately 25 °C. The relative humidity was estimated based on data reported by the National Institute of Standards and Technology (NIST), as indicated in **Table 5.2** [143]. The material was held under moist air at 300 °C for 120 minutes while weight was measured every 10 seconds.

Table 5.2: Saturated Aqueous Salt Solutions and Their Relative Humidity [143]

Saturated Solution	**% Relative Humidity at 25 °C**
NaCl	75.3 (1)
K_2CO_3	43.2 (4)
KCH_3COO	22.5 (3)

The above procedure was repeated for cubic $YbZrF_7$ (sample **G**) using a saturated K_2CO_3 salt solution for sample temperatures of 400 and 500 °C. Slight modifications were made to the sample heating procedure for these two experiments as detailed in **Table 5.3**. At the end of stage 3, the dry air flow was shut off for 10 minutes. A weight was recorded by

the TGA instrument every 10 seconds. Baseline correction was not applied for these measurements, as the weight drift was negligible compared to the weight loss observed.

Table 5.3: Thermogravimetric Analysis Temperature Schedule for Moisture Exposure at 400 and 500 °C

	Stage 1	**Stage 2**	**Stage 3**	**Stage 4**
Temperature	30 °C	30 → 400 °C	400 °C (dry)	400 °C (moisture)
Rate	---	30 °C min^{-1}	---	---
Duration	10 minutes	12 minutes	10 minutes	120 minutes
	Stage 1	**Stage 2**	**Stage 3**	**Stage 4**
Temperature	30 °C	30 → 500 °C	500 °C (dry)	500 °C (moisture)
Rate	---	30 °C min^{-1}	---	---
Duration	10 minutes	16 minutes	10 minutes	120 minutes

5.3 Results and Discussion

In summary, the high temperature thermal decomposition of both cubic and monoclinic $YbZrF_7$ was studied. Two separate powder x-ray diffraction patterns were obtained for a cubic $YbZrF_7$ sample. The initial powder pattern examined the sample which was previously stored under completely moisture free conditions. The subsequent powder pattern determined the effects of a 24 hour exposure to open air of unknown humidity at ambient temperature and pressure. Three cubic $YbZrF_7$ samples were treated with air of known relative humidity at 300, 400, and 500 °C in order to assess the sample's moisture reactivity.

5.3.1 Thermal Decomposition of $YbZrF_7$

Independently synthesized cubic $YbZrF_7$ (sample **G**) and monoclinic $YbZrF_7$ (sample **H**) were analyzed in terms of their behavior at temperatures near 900 °C. It must be noted that the monoclinic $YbZrF_7$ was not single-phase. Any weight change could be monitored as a function of temperature. Although their respective structures at room temperature were substantially different, it would not be expected that any decomposition occurring at high temperature would be affected by this.

As shown in **Figure 5.3**, cubic $YbZrF_7$ experienced negligible weight change until approximately 500 °C. Before this temperature, the pan maintained a slight weight baseline drift. At 700 °C, a rapid weight loss began and the weight loss rate persisted for approximately 10 minutes. Beyond this point, the sample was maximally thermally decomposed.

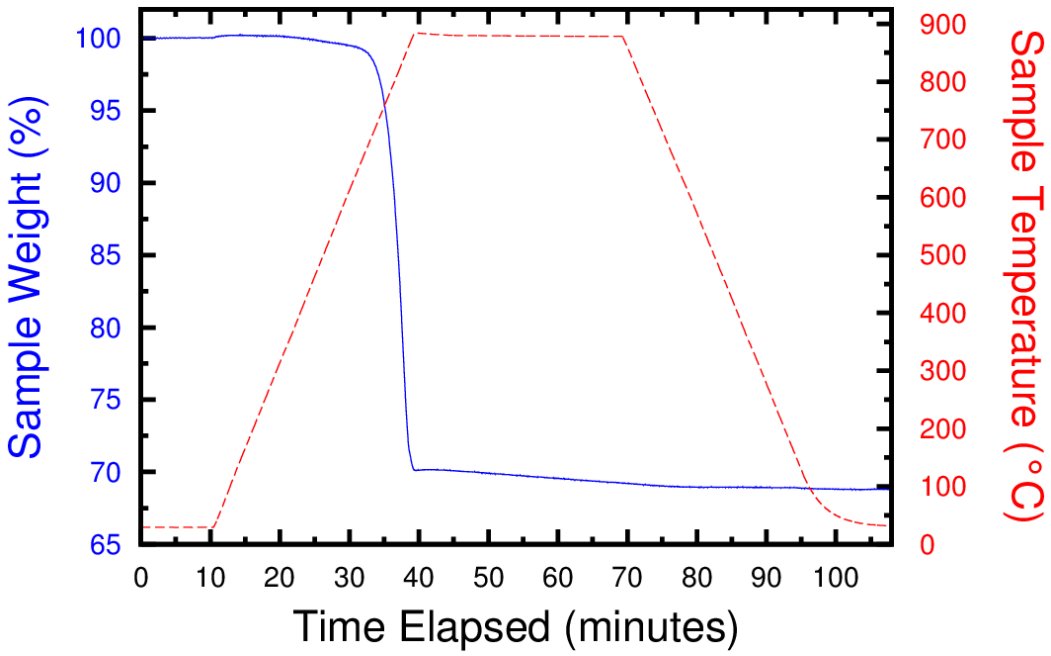

Figure 5.3: The thermal decomposition of cubic $YbZrF_7$ (sample **G**) is shown in relation to sample weight loss and applied temperature.

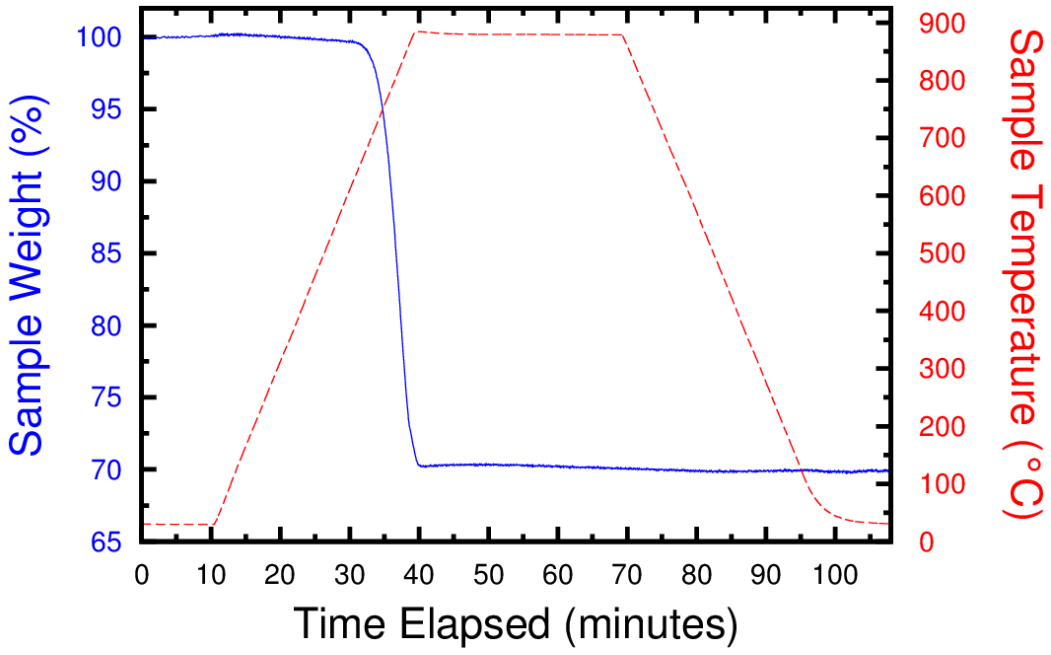

Figure 5.4: The thermal decomposition of monoclinic $YbZrF_7$ (sample **H**) is shown in relation to sample weight loss and applied temperature.

Similar behavior was observed for monoclinic $YbZrF_7$, as depicted in **Figure 5.4**. It is known that at temperatures between 600 and 700 °C, the monoclinic phase is thermodynamically stable [70]. Thus, no phase transition would have been initiated for the monoclinic sample in this domain. After 40 minutes had elapsed in the cubic sample, a 30 % weight loss was noted. An essentially identical weight loss of 30 % occurred for monoclinic $YbZrF_7$ at the same point in time. It appeared that for cubic $YbZrF_7$, the sample continued to thermally decompose but at a significantly lower rate. It is more likely that this constituted an experimental artifact as opposed thermal decomposition.

The only possible decomposition above 700 °C involves the decomposition of $YbZrF_7$ into its starting materials (YbF_3 and ZrF_4) and the subsequent sublimation of ZrF_4. The sublimation of ZrF_4 has been characterized in published literature and it is often exploited as a purification technique [69,144]. It is unlikely that the decomposition would proceed through another route in these conditions. The relative weight loss was larger than what would be allowed for the formation of fluorine gas. Additionally, the sample environment consisted of ultra-high purity nitrogen gas, which could not react with the sample. If the entire $YbZrF_7$ sample was converted to YbF_3 and ZrF_4, a 42 % weight loss would occur if all of the ZrF_4 was sublimated. Given that the thermal decomposition rate abruptly plateaued after 40 minutes, it may be reasonable to assume all produced ZrF_4 sublimated. A 30 % loss in weight implies that 71 % of the initial $YbZrF_7$ was decomposed into YbF_3 and ZrF_4, where ZrF_4 was transformed to the gas phase. This left 29 % of the original $YbZrF_7$ intact, along with solid YbF_3. This would be a highly unusual outcome, however. Another plausible explanation for the immediate decrease in thermal decomposition rate may stem from the presence of residual moisture within the TGA apparatus. If the sample

environment was not completely free of moisture, hydrolysis could take place simultaneously, which acts as a secondary contribution to weight loss. Confirmation of this would be experimentally challenging, as the remaining sample mass was insufficient for laboratory PXRD measurements.

5.3.2 Air and Moisture Stability of Cubic $YbZrF_7$

The moisture stability of cubic $YbZrF_7$ (sample **F**) was first assessed on a primarily qualitative basis. This involved powder x-ray diffraction measurements, which could identify any changes to the long-range order of the material stemming from a reaction with moisture. If the material amorphized, this would be revealed in dramatic loss of resolved cubic peak intensities, similar to the amorphized $YbZrF_7$ in **Chapter 4**.

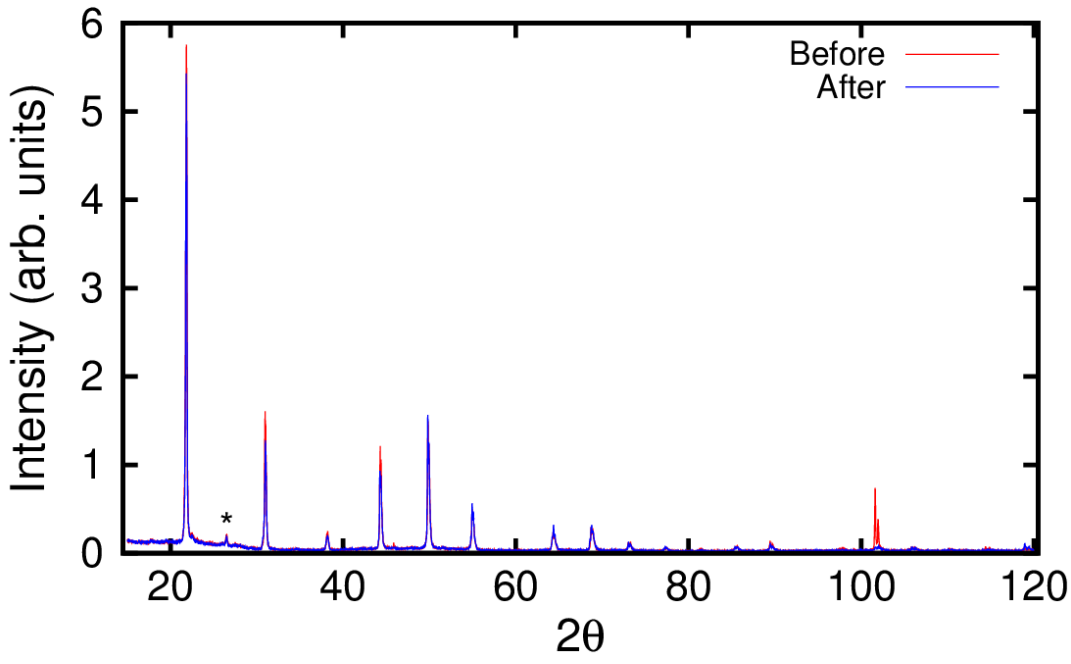

Figure 5.5: PXRD patterns for cubic $YbZrF_7$ (sample **G**) before and after exposure to air for 24 hours. A minor peak (*) represented the presence of YbF_3 and ZrF_4 impurities.

The diffraction pattern for cubic $YbZrF_7$ did not display any significant change following 24 hour exposure to air. The distinct ReO_3-type $YbZrF_7$ cubic peaks primarily retained their peak positions, even to high angle. Overall, evidence provided from the PXRD measurements suggests that cubic $YbZrF_7$ is quite stable in air at room temperature.

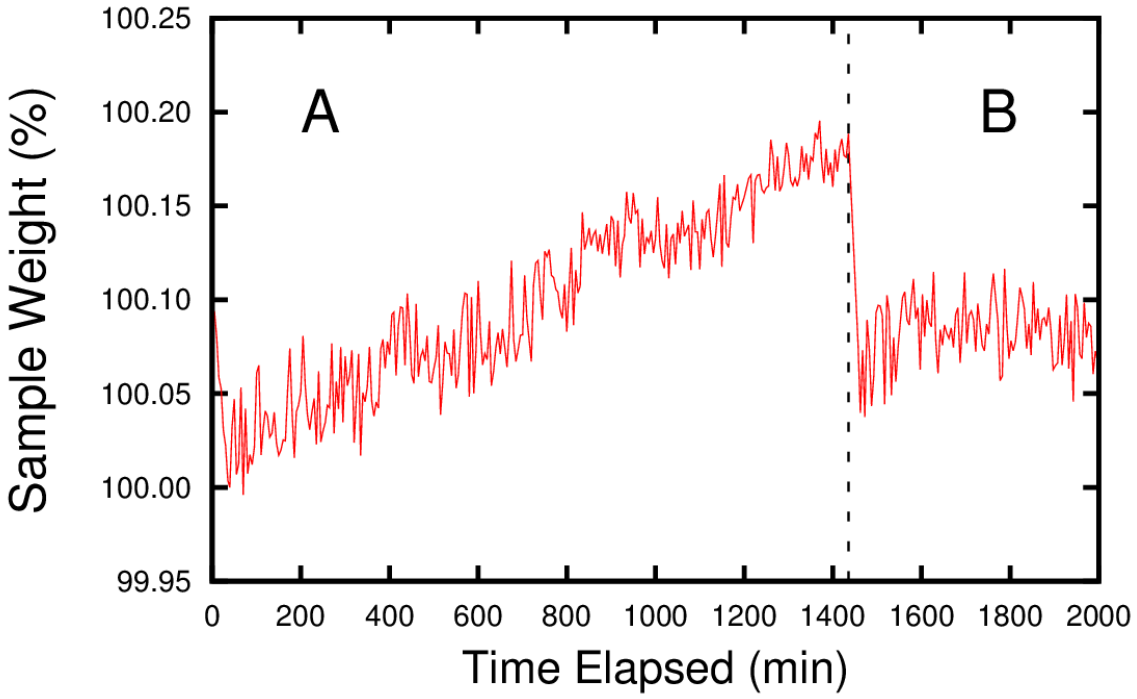

Figure 5.6: In region A, cubic $YbZrF_7$ is held in air at 30 °C for 24 hours. In region B, the sample was held in air at 120 °C in order to evaporate any produced HF.

As shown in **Figure 5.6**, the sample absorbed moisture, but only ~ 0.1 % of the initial sample weight. If the entire sample reacted with moisture to produce HF and it was completely evaporated at this temperature, a weight loss of approximately 5 % would be expected. Thus, 0.1 % of the sample is likely insufficient to affect the properties of cubic $YbZrF_7$. This result was consistent with PXRD measurements, indicative of insignificant

influence of moisture. Note that the large weight loss below 40 minutes duration is a non-real artifact. Above 40 minutes, sample weight changes are more reliable.

Initial settings controlled how the cubic $YbZrF_7$ sample was exposed to moist air. These settings involved exposing the material to dry air first at 30 ℃ for 30 minutes and subsequently for another 21 minutes at 300 ℃. TGA analysis will only consider weight changes that can be attributed to the moist air at 300 ℃, 400 ℃, and 500 ℃. $YbZrF_7$ was exposed to moist air of a known relative humidity for 120 minutes at these temperatures. It is known that at high temperatures, fluorides can react with water to generate oxides, as in the case of AlF_3 reacting with H_2O to form Al_2O_3 [145]. It is proposed that $YbZrF_7$ would react in a similar manner, as given in **Equation 5.1**.

$$YbZrF_{7\ (s)} + \frac{7}{2}H_2O_{\ (g)} \longrightarrow \frac{1}{2}Yb_2O_{3\ (s)} + ZrO_{2\ (s)} + 7HF_{\ (g)} \qquad \mathbf{5.1}$$

This reaction constitutes a 19.4 % weight loss, assuming 100 % formation of product and complete evaporation of hydrofluoric acid. All weight changes could be effectively detected through TGA, although there are kinetic and thermodynamic considerations. The reaction's favorability may be enhanced at increased temperature or relative humidity.

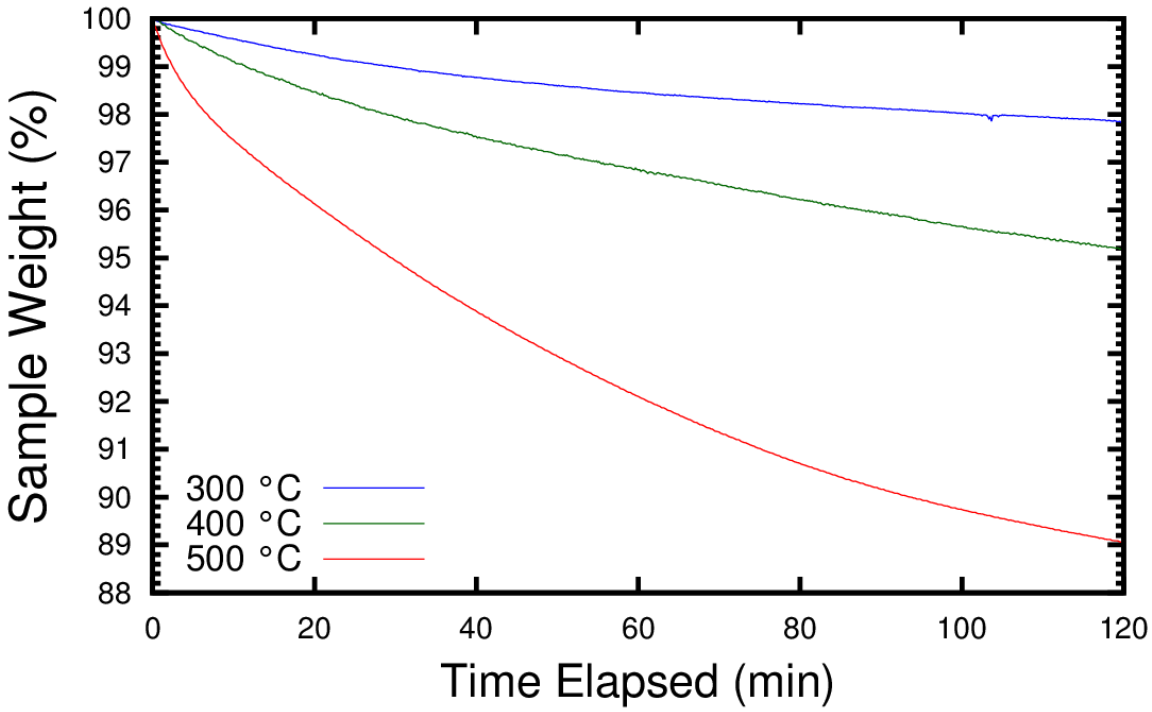

Figure 5.7: The moisture sensitivity of cubic $YbZrF_7$ at 43 % relative humidity is displayed at selected temperatures according to observed weight loss.

At 300 °C, $YbZrF_7$ remained mostly stable to moisture, as shown in **Figure 5.7**. A small total sample weight loss of 2.2 % represented only 11 % of the total possible weight loss allowed for the proposed reaction given by **Equation 5.1**. The weight loss was essentially doubled to approximately 4.8 % at 400 °C, indicative of 25 % of the weight loss expected if all of the H_2O available reacted with $YbZrF_7$. At 500 °C, the amount of moisture that reacted with the sample was substantial. This generated an approximately 11.0 % weight loss, implying that 57 % of the maximum available weight loss occurred. Supplemented with data obtained from the PXRD measurements, it may be reasonable to assume that at room temperature, $YbZrF_7$ sustains no appreciable weight loss due to this reaction. The moisture from air appears limited in its ability to react with $YbZrF_7$ at ambient temperature and pressure.

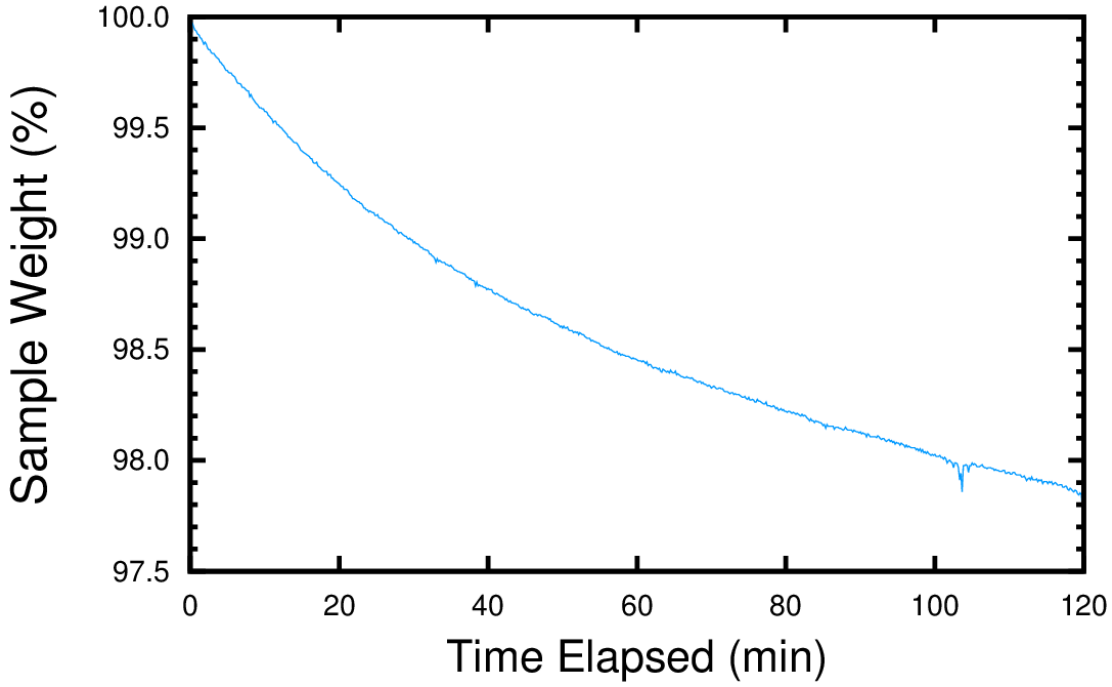

Figure 5.8: The moisture sensitivity of cubic $YbZrF_7$ at 43 % relative humidity and 300 °C is displayed according to observed weight loss.

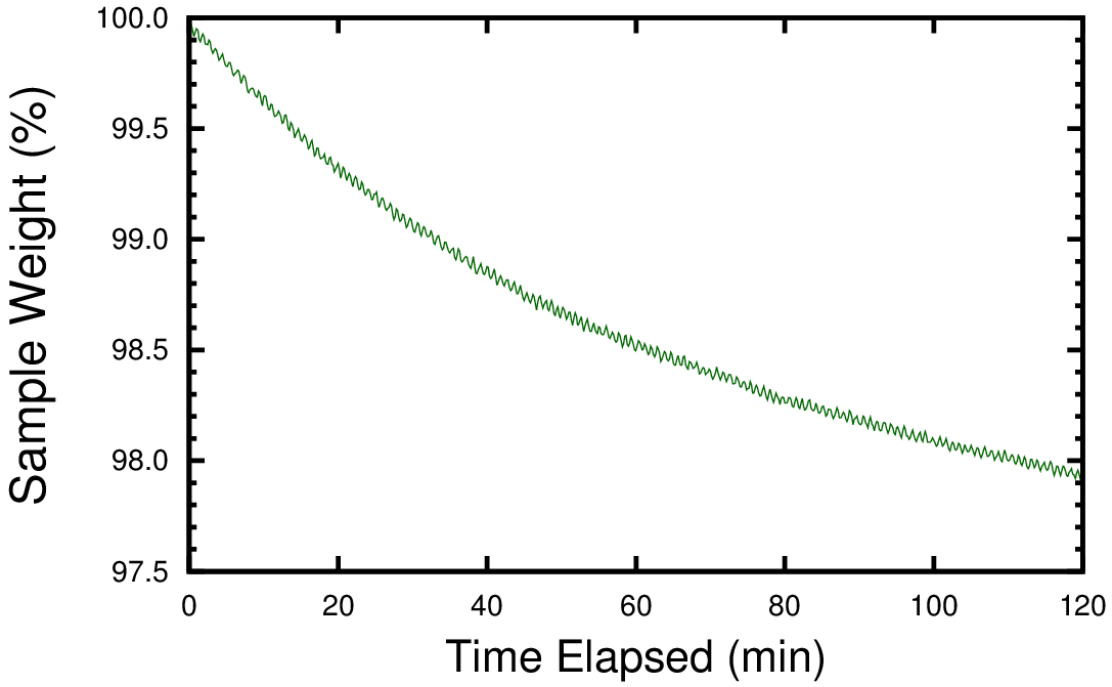

Figure 5.9: The moisture sensitivity of cubic $YbZrF_7$ at 75 % relative humidity and 300 °C is displayed according to observed weight loss.

Interestingly, virtually no difference in $YbZrF_7$ weight loss was observed for separate relative humidity of 43 and 75 percent. As shown in **Figure 5.9**, a remarkable degree of weight fluctuation was noted in the case of exposure to 75 percent relative humidity. This was especially true in comparison to 43 percent relative humidity, provided in **Figure 5.8**. Additionally, a drop in weight and immediate return to the previous weight was noted for the sample exposed to 43 percent humidity. These anomalies were likely experimental in origin and therefore unrelated to the presence of moisture.

5.4 Conclusions

Cubic $YbZrF_7$ displays nearly identical thermal decomposition compared to monoclinic $YbZrF_7$. An essentially constant rate of weight loss was observed between 750 and 900 °C. For both cubic and monoclinic $YbZrF_7$, this rate of thermal decomposition abruptly dropped to near zero following a sample weight loss of approximately 30 %. This presents several possibilities. The most likely source for this weight loss involves a contribution from both a sublimation of ZrF_4 as well as a hydrolysis reaction caused by residual moisture. A less likely cause for the weight loss involves conversion of 71 % of the original sample to a mixture to unreacted $YbZrF_7$, decomposed YbF_3, and gas-phase ZrF_4. PXRD and TGA measurements revealed that $YbZrF_7$ is reasonably stable in air at room temperature. Even at high temperatures, the relative humidity was discovered to have a negligible effect on the formation of Yb_2O_3 and ZrO_2 as part of a hydrolysis reaction.

CHAPTER 6

FINAL CONCLUSIONS AND POSSIBLE FUTURE WORK

Powder x-ray diffraction was the primary method of characterization in this study. It was adequate for identifying the average structure of $YbZrF_7$, its thermal expansion properties, and its behavior on compression. Other techniques are commonly applied in solid state chemistry, however. The structural model for cubic $YbZrF_7$ was derived from neutron diffraction data, reported by Poulain, et. al. [72]. Application of this model was the crucial component which revealed interesting properties of $YbZrF_7$. The investigation of ReO_3-type materials are often accompanied by the use of neutron diffraction, where a beam of neutrons are scattered by the atomic nuclei. This was accomplished in the cases of ScF_3 and $CaZrF_6$ [57,61]. The principal advantage of neutron scattering is its ability to confirm and refine an elucidated crystal structure. Neutrons, however, must originate from a spallation source or nuclear reaction, dramatically increasing operational costs [84]. The amount of sample required for measurement is also substantially larger compared to powder x-ray diffraction.

The local structure of $YbZrF_7$ was not elaborated on, as it demands a separate characterization technique. In conventional powder x-ray diffraction, the average crystal structure is determined through Bragg scattering, as described in **Section 1.9**. Oftentimes, this is sufficient for the study of a crystalline system, as the long-range order may be the only consideration. A more thorough description of the crystal structure can be obtained from total x-ray scattering, although it requires complicated modeling [146]. In total scattering, both Bragg scattering and diffuse scattering are accounted for. This introduces

a pair distribution function, which ultimately allows for the calculation of bond distances [147]. In $YbZrF_7$, this would translate to the range of metal-metal and metal-fluoride bond distances. This produces a view of the local structure, which can provide mechanistic insight into the unusual behavior of cubic $YbZrF_7$.

The thermal expansion behavior of $YbZrF_7$ was examined over the range 100 – 500 K. At temperatures above 500 K, a phase transition occurs. The proposed secondary phase was monoclinic, although this was essentially unconfirmed due to the lack of an available PXRD fit above 500 K. Although a pure phase of monoclinic $YbZrF_7$ has not been synthesized, the proposed structural model (**Tables A.10**, **A.11**) must be used to analyze data for these temperatures. The largest NTE observed in $YbZrF_7$ was typically between 300 and 370 K. Beyond this point, the volumetric expansion coefficient remains positive to 500 K. While it may be considered unlikely that it sustains NTE at temperatures above 500 K, similar materials such as ReO_3 have shown multiple regions of NTE [58]. This can be readily addressed for $YbZrF_7$, as the necessary PXRD data has been acquired.

$YbZrF_7$ displays several intriguing properties. A thermal history dependence was observed, which probably involves local structural changes associated with fluoride mobility when initially heated above 300 K. Additionally, near zero volumetric thermal expansion was identified near room temperature after the first heating. When $YbZrF_7$ is compressed, it undergoes abrupt amorphization near 0.9 GPa. Pressure-induced softening also occurs. Although pressure-induced softening is rare, it has been seen in other similar ReO_3-type materials [61]. It remains unknown whether these phenomena would reoccur in the case of monoclinic $YbZrF_7$. A single phase of monoclinic $YbZrF_7$ must be synthesized, as all prior attempts have resulted in a mixed phase system, possibly

including unreacted starting material. If pure monoclinic $YbZrF_7$ can be successfully synthesized, it may then be a target for such studies.

The density of cubic $YbZrF_7$ was experimentally determined for a quenched sample. The measured density was in reasonable agreement with a GSAS-computed density for the same material, as well as a theoretical density reported by Poulain, et. al [72]. It may also be valuable to study how different heat treatments influence the packing of cations and anions, as the diffraction measurements support the structure's relaxation on heat treatment.

It is interesting that cubic $YbZrF_7$ is quite air and moisture stable at room temperature. This was determined by a combination of PXRD and TGA measurements. In the case of PXRD data, virtually no change was observed between each diffraction pattern of cubic $YbZrF_7$. TGA showed a < 0.1 % weight change in moist air. It may be considered how these findings can be extended. For example, infrared spectroscopy may directly determine the presence of a hydroxyl stretching frequency [23]. At modest relative humidity, it is predicted that this infrared signature would be undetected for air exposure limited to 24 hours. The conditions of relative humidity explored in this study were limited, however. Cubic $YbZrF_7$ may more readily react with water at a relative humidity approaching 100 percent. This may be the case for either room temperature or temperatures above 300 °C. If cubic $YbZrF_7$ were to be used for application, a comprehensive knowledge of its reactivity with moisture would be valuable.

Although a large number of $LnZrF_7$ materials have been synthesized, only $YbZrF_7$ was focused on in this work. Previous attempts to synthesize cubic $YZrF_7$ were unsuccessful,

as only the monoclinic phase could be generated. There may be potential in producing cubic $LaZrF_7$, although compounds with higher ratios of zirconium have also been reported, such as $LaZr_3F_{15}$ or $LaZr_2F_{11}$ [148-149].

$YbZrF_7$ maintains 1:1 stoichiometry, although recent research efforts have explored the synthesis of off-stoichiometric varieties of ReO_3-type materials as a means to control their thermal expansion. It is of course fundamental that charge balance be preserved, but an additional constraint is that the ReO_3-type structure be retained if there is NTE and ZTE interest. This typically involves the removal of cations, introducing crystallographic defects. This was accomplished by Wang, et. al. for a zirconium doped ScF_3 system, which essentially produces an analogous material to $YbZrF_7$ in the form of $Sc_{1-x}Zr_xF_{3+\delta}$ [63]. The synthesis of non-stoichiometric cation ordered derivatives of $MgZrF_6$ has also been reported where the material becomes zirconium rich, given by $Mg_{1-x}Zr_xF_{6+2x}$ [62]. Synthesis and characterization of zirconium rich derivatives of $YbZrF_7$ has also been accomplished, as in the case of $YbZr_3F_{15}$, which adopts an ReO_3-related structure [150]. The system $Yb_{0.2}Zr_{0.8}F_{3.2}O_{0.3}$ has also been previously characterized, as it has been described to adopt an interstitial anion-excess ReO_3-type structure [151]. It is presently unknown whether either of these two classes of off-stoichiometric $YbZrF_7$ may display a promising range of NTE behavior. If a set of materials (such as $Yb_xZr_{1-x}F_{3+x}O_\delta$) can be synthesized, there may be interest in determining if their thermal expansion coefficients can be tuned as a function of composition.

APPENDIX-A

SUPPLEMENTARY MATERIAL

Table A.1: Additional Phillips X'Pert MPD Powder X-Ray Diffractometer Settings Adopted for All Measurements (Part I)

Goniometer	PW3050
Sample Stage	MPSS (vertical)
Kα (Å)	1.541874
Kβ (Å)	1.392250
Incident Beam Path Radius (mm)	200.0
Anode Material	Cu
Voltage (kV)	40
Current (mA)	40
Focus Type	Line
Focus Length (mm)	12.0
Focus Width (mm)	0.4
Focus Take-Off Angle (°)	6.0
Soller Slit Opening (rad.)	0.04

Table A.2: Additional Phillips X'Pert MPD Powder X-Ray Diffractometer Settings Adopted for All Measurements (Part II)

Mask	Fixed 10 mm (MPD/MRD)
Mask Distance to Sample (mm)	85
Mask Width (mm)	6.60
Divergence Slit Type	Progressive Divergence Slit (Fixed)
Distance from Slit To Sample (mm)	100
Divergence Slit Angle (°)	0.5
Diffracted Beam Path Radius (mm)	200.0
Anti-Scatter Slit Type	Progressive AS Slit (Fixed)
Anti-Scatter Slit Angle (°)	0.50
Monochromator	Diffracted Beam Curved 1x Graphite Cu
Receiving Slit Type	Progressive Receiving Slit
Receiving Slit Height (mm)	0.30
Detector Name and Type	PW3011/10 (Point Detector)
PHD Lower, Upper Level Range (%)	35.0 – 80.0
Scan Mode	Continuous
Phi (°)	0.0

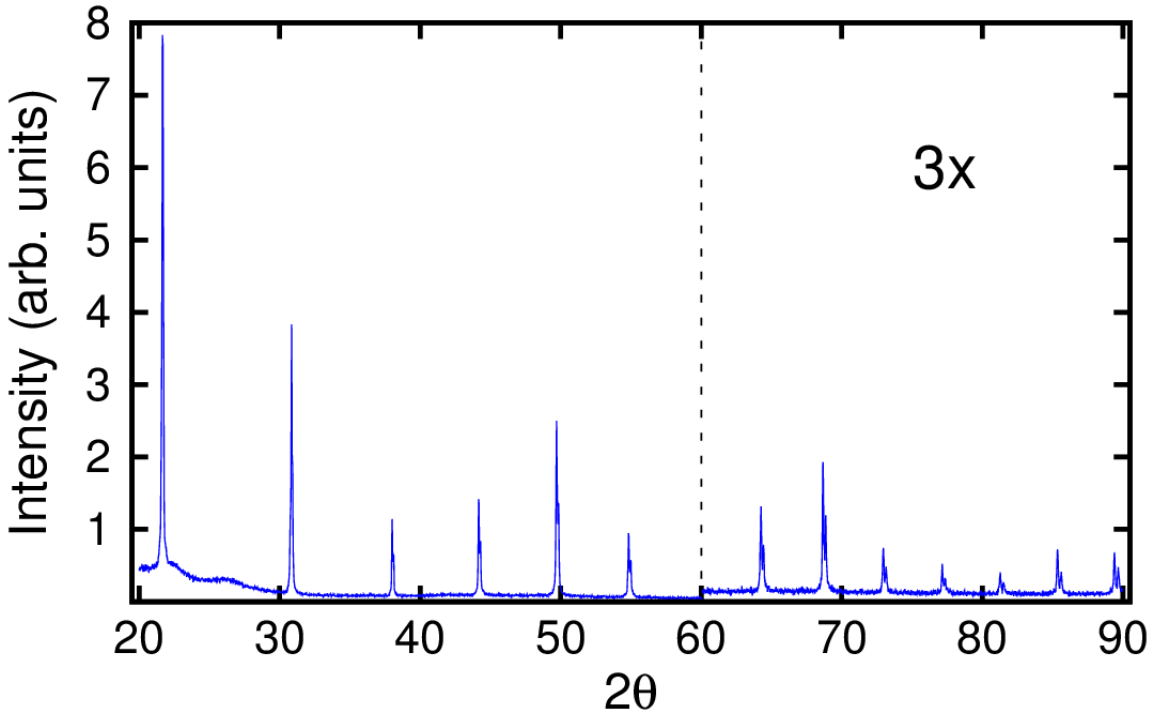

Figure A.1: The raw laboratory x-ray diffraction pattern of cubic $YbZrF_7$ (sample **A**) is shown in blue. High angle peaks are magnified.

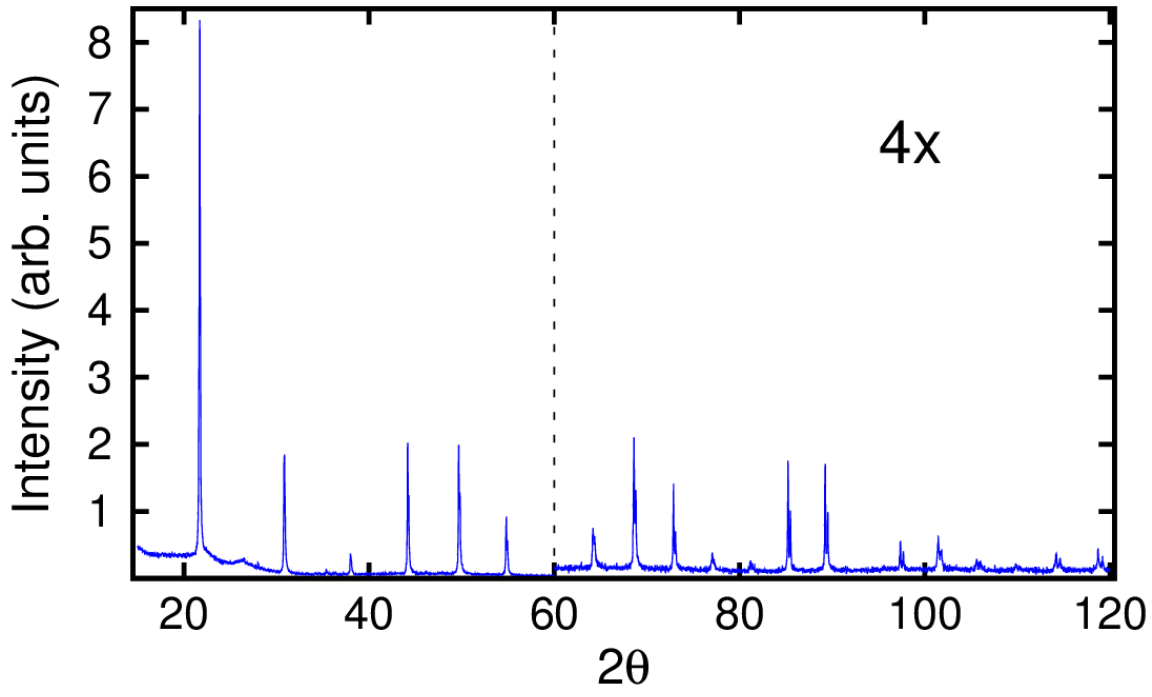

Figure A.2: The raw laboratory x-ray diffraction pattern of cubic $YbZrF_7$ (sample **B**) is shown in blue. High angle peaks are modified.

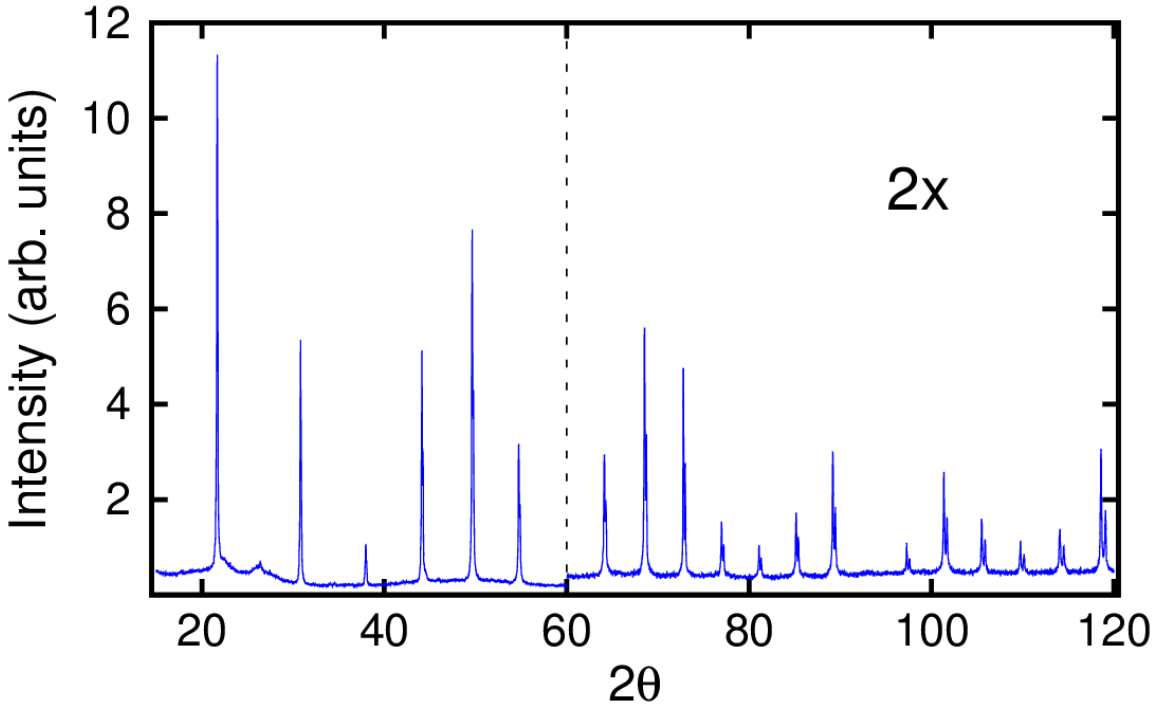

Figure A.3: The raw laboratory x-ray diffraction pattern of cubic $YbZrF_7$ (sample **C**) is shown in blue. High angle peaks are magnified.

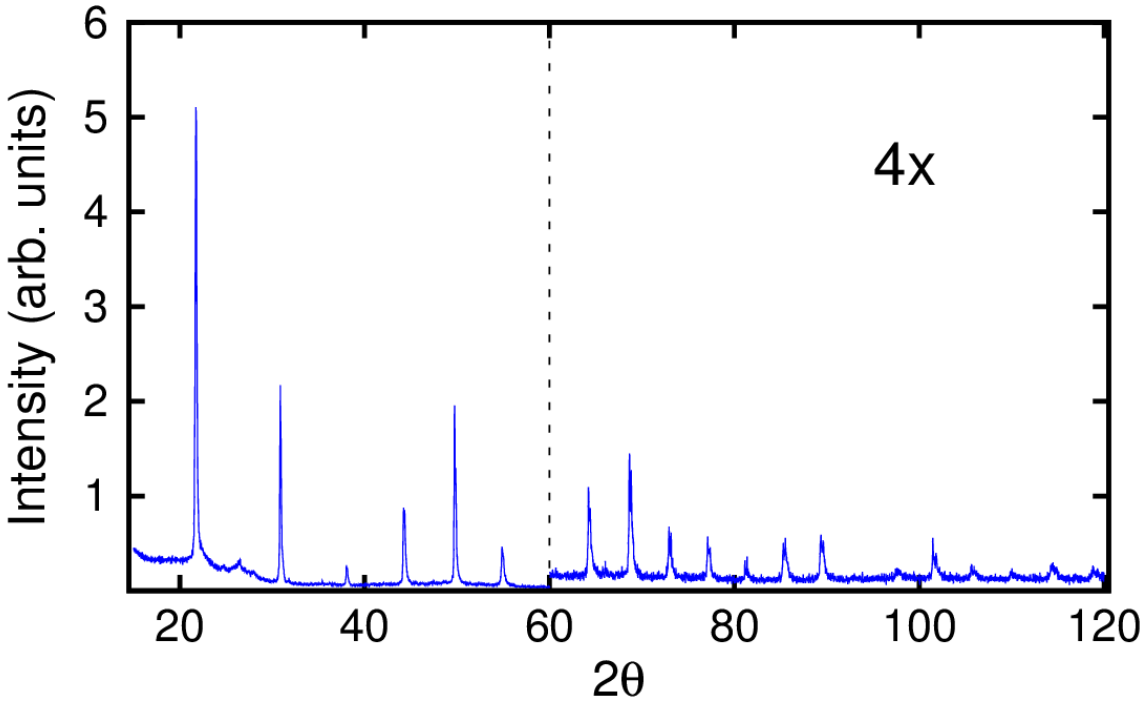

Figure A.4: The raw laboratory x-ray diffraction pattern of cubic $YbZrF_7$ (sample **D**) is shown in blue. High angle peaks are modified.

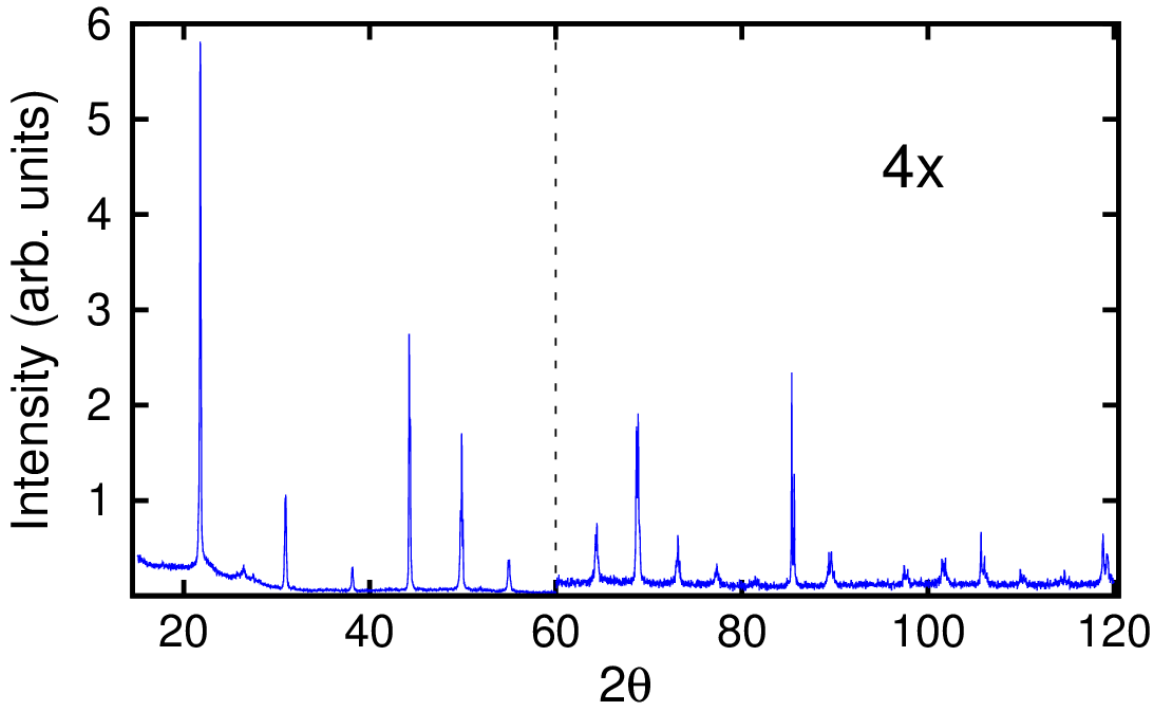

Figure A.5: The raw laboratory x-ray diffraction pattern of cubic $YbZrF_7$ (sample **E**) is shown in blue. High angle peaks are magnified.

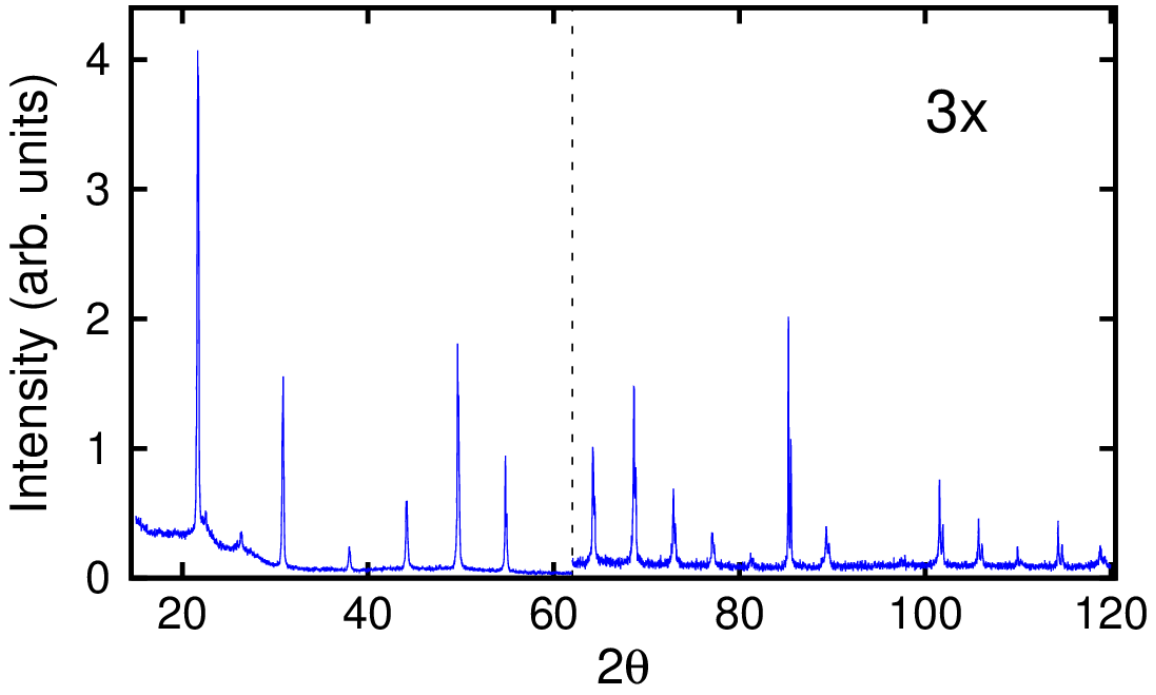

Figure A.6: The raw laboratory x-ray diffraction pattern of cubic $YbZrF_7$ (sample **F**) is shown in blue. High angle peaks are modified.

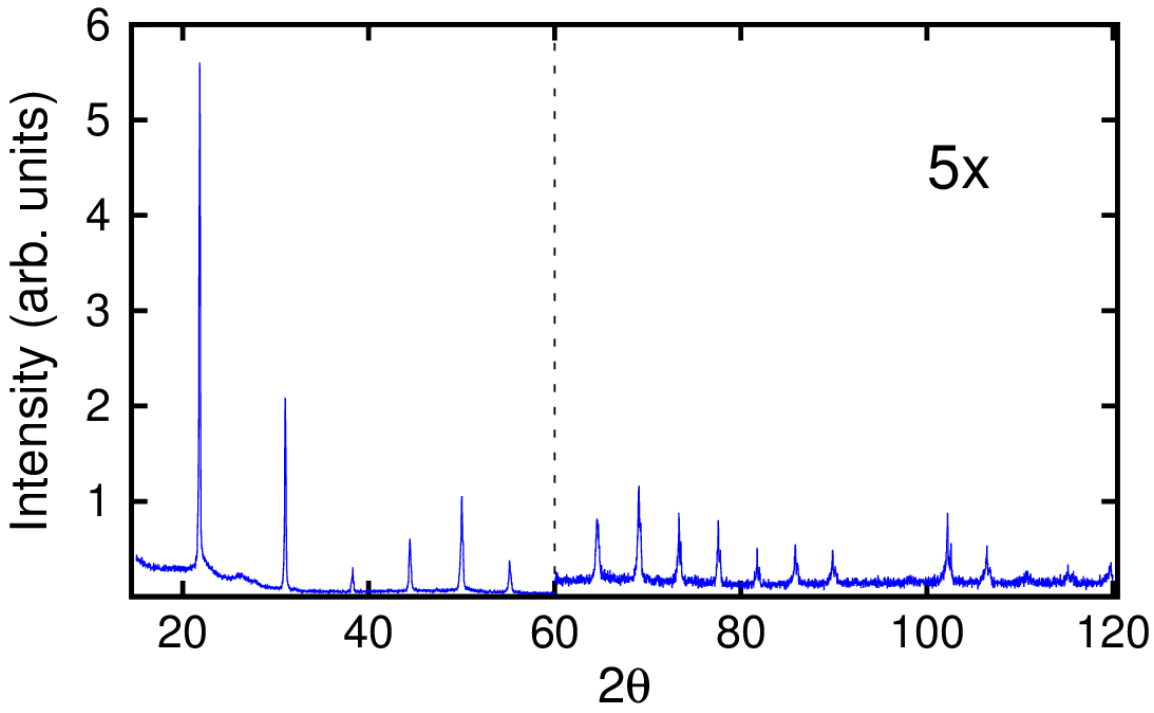

Figure A.7: The raw laboratory x-ray diffraction pattern of cubic $YbZrF_7$ (sample **G**) is shown in blue. High angle peaks are magnified.

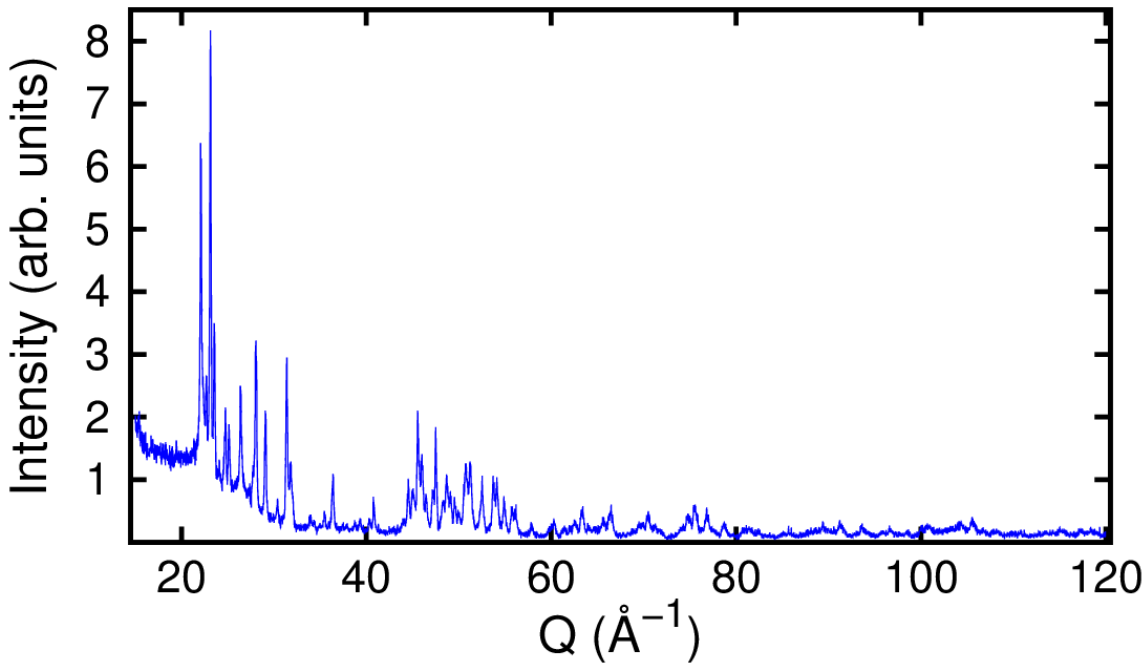

Figure A.8: The raw laboratory x-ray diffraction pattern of monoclinic $YbZrF_7$ (sample **H**) is shown in blue. High angle peaks are modified.

Table A.3: Laboratory Powder X-Ray Diffraction GSAS Model Fitting Settings for Cubic $YbZrF_7$ Data Analysis

Sample ID	Method	# Cycles Per Run	Background Function	Data Limits (2θ)	Scale Factor
A	Rietveld	30	Shifted Chebyschev (SC) (20 terms)	0.000 – 89.700	26.961
B	Rietveld	30	SC (20 terms)	0.000 – 119.990	28.419
C	Rietveld	30	SC (20 terms)	0.000 – 119.990	50.306
D	Rietveld	30	SC (20 terms)	0.000 – 119.990	26.824
E	Rietveld	30	SC (20 terms)	0.000 – 119.990	22.233
F	Rietveld	30	SC (20 terms)	0.000 – 119.990	22.104
G	Rietveld	30	SC (20 terms)	0.000 – 119.990	21.715

Table A.4: Laboratory Powder X-Ray Diffraction GSAS Fitting Profile Refinements for Cubic $YbZrF_7$ Data Analysis (Part I)

Sample ID	GU	GV	GW	GP
A	0.000000E+00	-0.165965E+01	0.498021E+01	0.000000E+00
B	0.000000E+00	0.000000E+00	0.177089E+01	0.000000E+00
C	0.000000E+00	-0.180478E+02	0.434047E+02	0.000000E+00
D	0.804840E+03	-0.519732E+03	0.907977E+02	0.000000E+00
E	0.773503E+03	-0.492761E+03	0.703911E+02	0.000000E+00
F	0.102034E+03	-0.170246E+03	0.781134E+02	0.000000E+00
G	0.000000E+00	0.000000E+00	0.103873E+02	0.000000E+00

Table A.5: Laboratory Powder X-Ray Diffraction GSAS Fitting Profile Refinements for Cubic $YbZrF_7$ Data Analysis (Part II)

Sample ID	LX	LY	S/L	H/L
A	0.629469E+01	0.000000E+00	0.500000E-03	0.500000E-03
B	0.900469E+01	0.986964E+00	0.500000E-03	0.500000E-03
C	0.000000E+00	0.000000E+00	0.500000E-03	0.500000E-03
D	0.774889E+01	0.126496E+02	0.500000E-03	0.500000E-03
E	0.824763E+01	0.931467E+01	0.500000E-03	0.500000E-03
F	0.693371E+01	0.175508E+01	0.500000E-03	0.500000E-03
G	0.202041E+01	0.291854E+02	0.500000E-03	0.500000E-03

Table A.6: Laboratory Powder X-Ray Diffraction GSAS Fitting Profile Refinements for Cubic $YbZrF_7$ Data Analysis (Part III)

Sample ID	TRNS	SHFT	STEC	PTEC
A	0.000000E+00	0.864179E+00	0.000000E+00	0.000000E+00
B	0.000000E+00	-0.473222E+01	0.000000E+00	0.000000E+00
C	0.270979E+00	-0.292333E+01	0.000000E+00	0.000000E+00
D	0.000000E+00	-0.704820E+01	0.000000E+00	0.000000E+00
E	0.000000E+00	-0.915323E+01	0.297413E+01	0.000000E+00
F	0.000000E+00	0.382995E+00	0.000000E+00	0.000000E+00
G	0.000000E+00	-0.508160E+01	0.000000E+00	0.000000E+00

Table A.7: Laboratory Powder X-Ray Diffraction GSAS Fitting Profile Refinements for Cubic $YbZrF_7$ Data Analysis (Part IV)

Sample ID	SFEC	L11	L22	L33
A	0.000000E+00	0.000000E+00	0.000000E+00	0.000000E+00
B	0.000000E+00	0.000000E+00	0.000000E+00	0.000000E+00
C	0.000000E+00	0.000000E+00	0.000000E+00	0.000000E+00
D	0.000000E+00	0.000000E+00	0.000000E+00	0.000000E+00
E	0.000000E+00	0.000000E+00	0.000000E+00	0.000000E+00
F	0.000000E+00	0.000000E+00	0.000000E+00	0.000000E+00
G	0.000000E+00	0.000000E+00	0.000000E+00	0.000000E+00

Table A.8: Laboratory Powder X-Ray Diffraction GSAS Fitting Profile Refinements for Cubic $YbZrF_7$ Data Analysis (Part V)

Sample ID	L12	L13	L23	DAMPING
A	0.000000E+00	0.000000E+00	0.000000E+00	0
B	0.000000E+00	0.000000E+00	0.000000E+00	0
C	0.000000E+00	0.000000E+00	0.000000E+00	0
D	0.000000E+00	0.000000E+00	0.000000E+00	0
E	0.000000E+00	0.000000E+00	0.000000E+00	0
F	0.000000E+00	0.000000E+00	0.000000E+00	0
G	0.000000E+00	0.000000E+00	0.000000E+00	0

Table A.9: Initial Model Used for the GSAS Powder X-Ray Diffraction Fits for All Cubic $YbZrF_7$ Samples

	Fractional Coordinate (x)	**Fractional Coordinate (y)**	**Fractional Coordinate (z)**	**Multiplicity**	**Occupancy**	**U_{iso}**
Yb (1)	0.000000	0.000000	0.060000	6	0.0833	0.02166
Zr (1)	0.000000	0.000000	0.060000	6	0.0833	0.02166
F (1)	0.500000	0.052000	0.052000	12	0.2217	0.03926
F (2)	0.500000	0.289000	0.064000	24	0.0325	0.03825

Table A.10: Initial Unit Cell Lattice Constants for Monoclinic $YbZrF_7$ Prior to Fit (Sample **H**)

a (Å)	11.084	**α (°)**	90.000
b (Å)	5.613	**β (°)**	107.680
c (Å)	8.850	**γ (°)**	90.000

Table A.11: Initial Model Used in GSAS for Monoclinic $YbZrF_7$ (Sample **H**)

	Fractional Coordinate (x)	**Fractional Coordinate (y)**	**Fractional Coordinate (z)**	**Multiplicity**	**Occupancy**	**U_{iso} ($Å^2$)**
Yb (1)	0.23389	0.24247	0.42143	4	1.000	0.010
Zr (1)	0.04400	0.24443	0.77028	4	1.000	0.010
F (1)	0.13970	0.23298	0.62019	4	1.000	0.010
F (2)	0.94379	0.24011	0.91739	4	1.000	0.010
F (3)	0.35533	0.01506	0.62413	4	1.000	0.010
F (4)	0.82949	0.95956	0.08533	4	1.000	0.010
F (5)	0.76616	0.58286	0.79828	4	1.000	0.010
F (6)	0.95408	0.95738	0.67137	4	1.000	0.010
F (7)	0.57870	0.95897	0.86685	4	1.000	0.010

Report Number: 95619 GALBRAITH LABORATORIES, INC. Report Date: 2017-02-13

Laboratory Report

Report prepared for:
John Ticknor
Georgia Inst of Tech
901 Atlantic Dr
Atlanta, GA 30332
Phone: 706-573-8599
Email: joticknor@gatech.edu

Report prepared by:
Christy Love

Purchase Order:
Visa,Wilkinson,2/6/17

For further assistance, contact:
Christy Love
Report Coordinator
PO Box 51610
Knoxville, TN 37950 -1610
(865) 546-1335
christylove@galbraith.com

Sample: JT-01-74-1
Lab ID: 2017-D-5325 **Received:** 2017-02-06

Analysis	Method	Result	Basis	Sample Amount Used	Date (Time)
Ni : Nickel					
	GLI Procedure ME-70	0.558 %	As Received	104.01 mg	2017-02-09
Yb : Ytterbium					
	GLI Procedure ME-70	44.3 %	As Received	104.01 mg	2017-02-09
Zr : Zirconium					
	GLI Procedure ME-70	21.3 %	As Received	104.01 mg	2017-02-09

Signatures:

Published By:	Christy.Love	2017-02-13T21:03:12.947-05:00
Created By:	Christy.Love	2017-02-13T21:02:57.453-05:00

- Physical signatures are on file.
- "Published By" signature indicates authorized release of data.

Figure A.9: The laboratory report submitted by Galbraith Laboratories documents elemental analysis results [114].

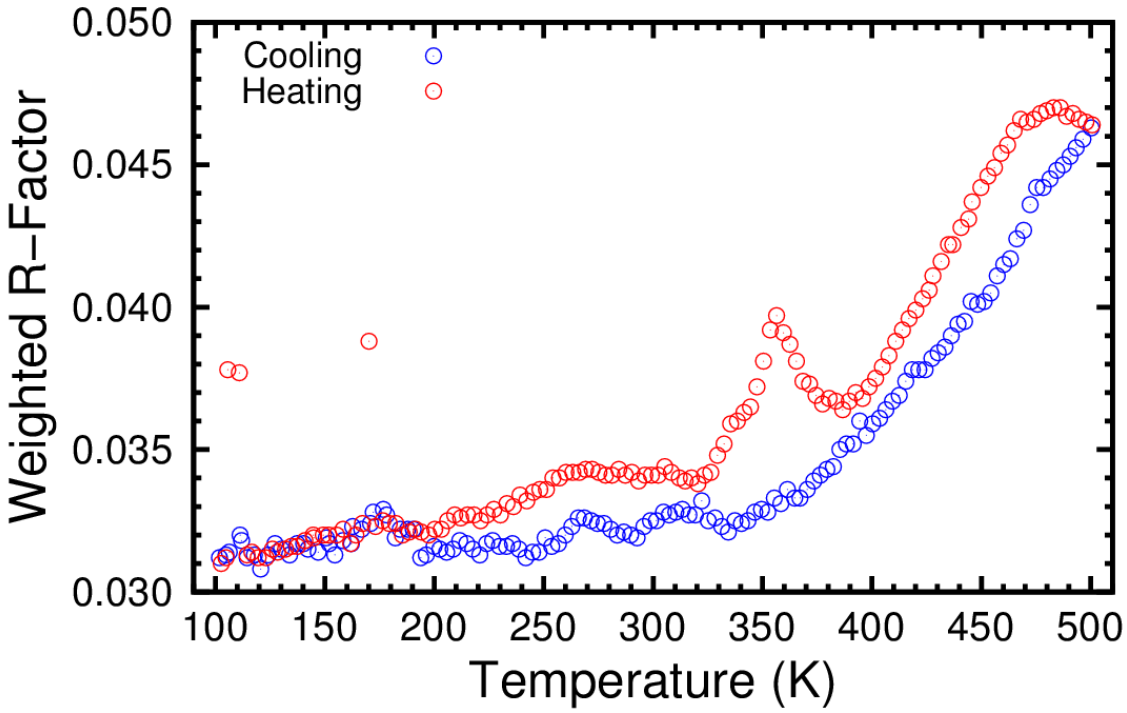

Figure A.10: The calculated weighted R-factors for each Rietveld fit are shown for CRYO-A data.

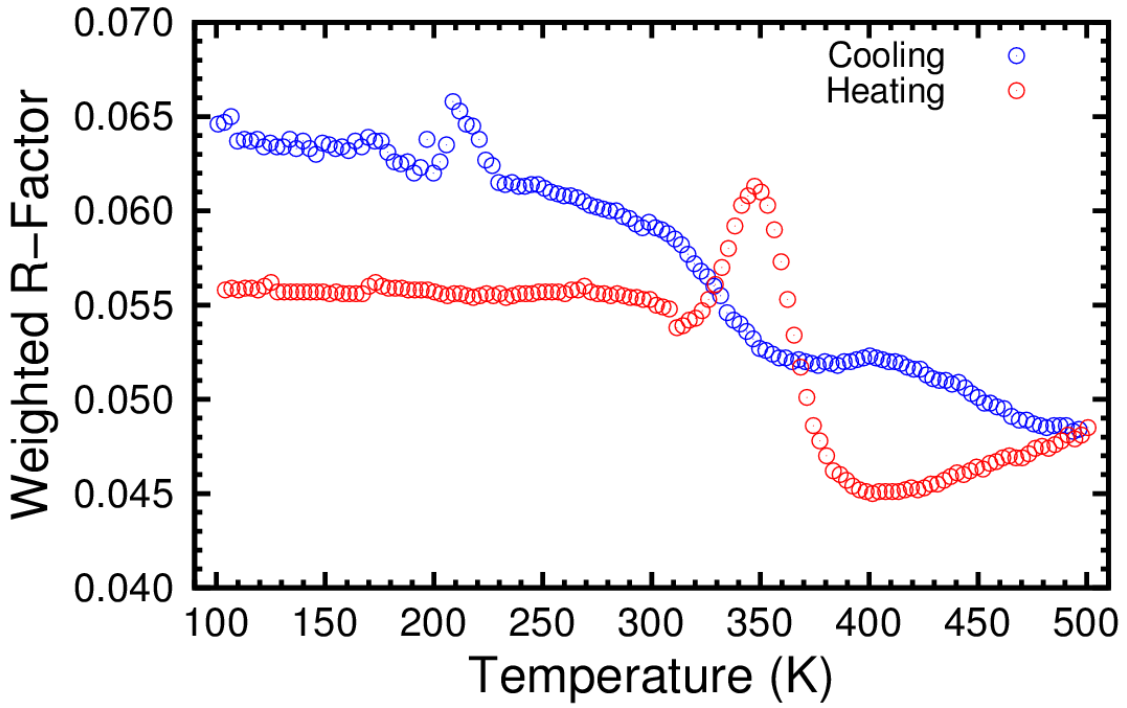

Figure A.11: The calculated weighted R-factors for each Rietveld fit are shown for CRYO-C_1 data.

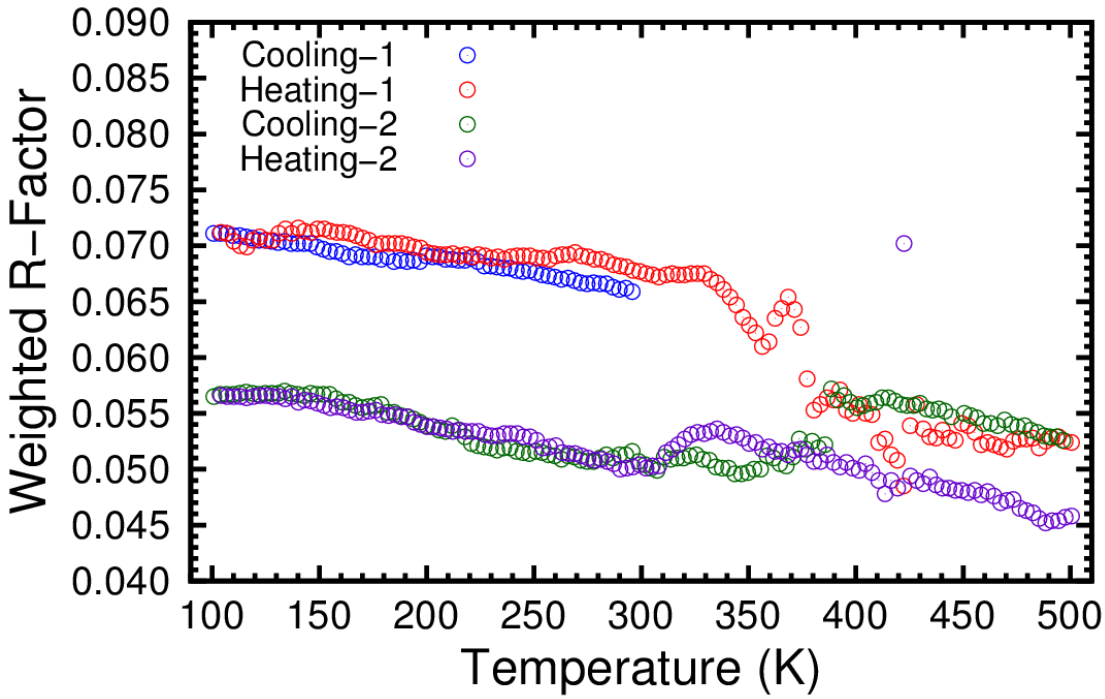

Figure A.12: The calculated weighted R-factors for each Rietveld fit are shown for CRYO-C_2 data.

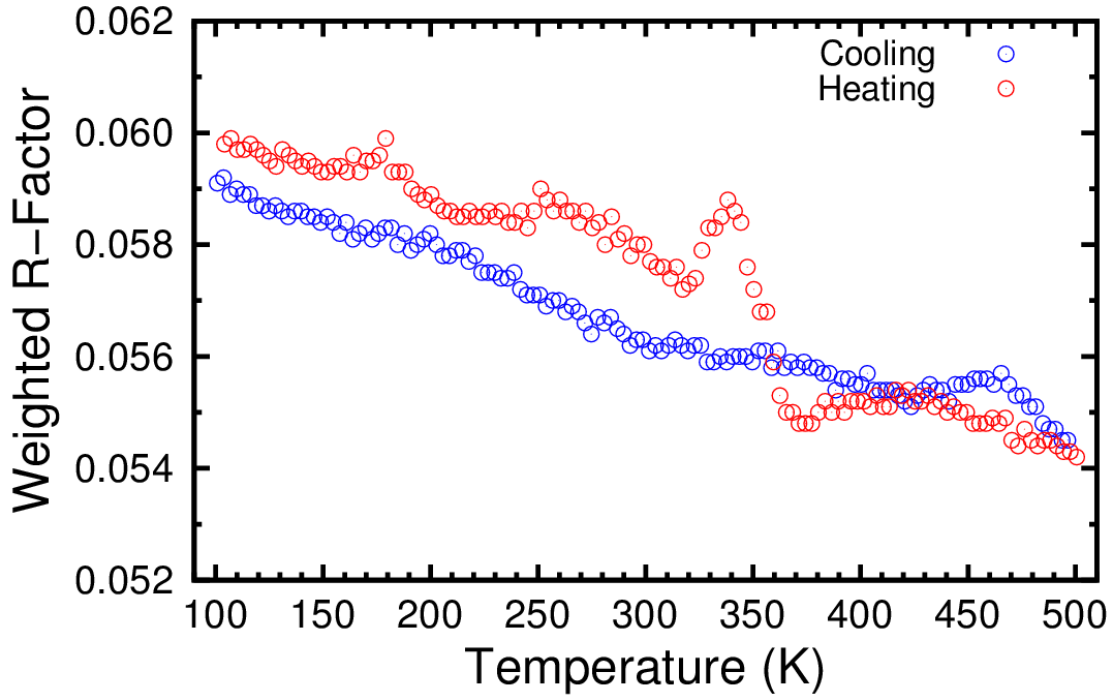

Figure A.13: The calculated weighted R-factors for each Rietveld fit are shown for CRYO-F data.

Table A.12: GSAS Refinements for Initial Rietveld Fit (100 K) of CRYO-A Variable Temperature Data

# of Cycles	30	**Scale Factor (Refined)**	21.583
Unit Cell	Refined	**GV (Refined)**	- 0.412887E+02
Data Limits (2θ)	8.000 – 40.000	**GW (Refined)**	0.175281E+02
Background Type	Shifted Chebyschev	**LX (Refined)**	0.479205E+00
Background Terms	20	**LY (Refined)**	0.229613E+02
Background Refined?	YES	**SHFT (Refined)**	0.158679E+00
Profile Damping	0	**Non-Refined Parameters (Set to Default Values)**	GU, GP, S/L, H/L, TRNS, STEC, PTEC, SFEC, L11, L22, L33, L12, L13, L23, X, F

Table A.13: GSAS Refinements for Initial Rietveld Fit (100 K) of CRYO-C_1 Variable Temperature Data ($YbZrF_7$)

# of Cycles	30	**Scale Factor (Refined)**	54.517
Unit Cell	Refined	**GV (Refined)**	-0.298076E+02
Data Limits (2θ)	8.000 – 38.000	**GW (Refined)**	0.134134E+02
Background Type	Shifted Chebyschev	**LX (Refined)**	0.104997E+01
Background Terms	20	**LY (Refined)**	0.141043E+02
Background Refined?	YES	**SHFT (Refined)**	0.719775E+00
Profile Damping	0	**Non-Refined Parameters (Set to Default Values)**	GU, GP, S/L, H/L, TRNS, STEC, PTEC, SFEC, L11, L22, L33, L12, L13, L23, X, F

Table A.14: GSAS Refinements for Initial Rietveld Fit (100 K) of CRYO-C_1 Variable Temperature Data (Silicon)

# of Cycles	30	**Phase Fraction $YbZrF_7$**	1.000
Unit Cell	Refined	**Phase Fraction Si**	0.87183E-01
Data Limits (2θ)	8.000 – 38.000	**GW (Refined)**	0.134243E+02
Background Type	Shifted Chebyschev	**GV (Refined)**	-0.123355E+02
Background Terms	20	**SHFT (Refined)**	0.169161E+01
Background Refined?	YES	**Non-Refined Parameters (Set to Default Values)**	LX, LY GU, GP, S/L, H/L, TRNS, STEC, PTEC, SFEC, L11, L22, L33, L12, L13, L23, X, F
Profile Damping	0		

Table A.15: GSAS Refinements for Initial Rietveld Fit (299 K) of CRYO-C_2 Variable Temperature Data ($YbZrF_7$)

# of Cycles	30	**Scale Factor (Refined)**	32.849
Unit Cell	Refined	**GV (Refined)**	-0.360986E+02
Data Limits (2θ)	8.000 – 38.000	**GW (Refined)**	0.150929E+02
Background Type	Shifted Chebyschev	**LX (Refined)**	0.440761E+00
Background Terms	20	**LY (Refined)**	0.224884E+02
Background Refined?	YES	**SHFT (Refined)**	0.331523E+00
Profile Damping	0	**Non-Refined Parameters (Set to Default Values)**	GU, GP, S/L, H/L, TRNS, STEC, PTEC, SFEC, L11, L22, L33, L12, L13, L23, X, F

Table A.16: GSAS Refinements for Initial Rietveld Fit (299 K) of CRYO-C_2 Variable Temperature Data (Silicon)

# of Cycles	30	**Phase Fraction $YbZrF_7$**	1.000
Unit Cell	Refined	**Phase Fraction Si**	0.54442
Data Limits (2θ)	8.000 – 38.000	**GW (Refined)**	0.138614E+02
Background Type	Shifted Chebyschev	**GV (Refined)**	-0.775917E+01
Background Terms	20	**SHFT (Refined)**	0.120537E+01
Background Refined?	YES	**Non-Refined Parameters (Set to Default Values)**	LX, LY GU, GP, S/L, H/L, TRNS, STEC, PTEC, SFEC, L11, L22, L33, L12, L13, L23, X, F
Profile Damping	0		

Table A.17: GSAS Refinements for Initial Rietveld Fit (100 K) of CRYO-F Variable Temperature Data ($YbZrF_7$)

# of Cycles	30	**Scale Factor (Refined)**	7.8944
Unit Cell	Refined	**GV (Refined)**	-0.130768E+02
Data Limits (2θ)	5.000 – 23.491	**GW (Refined)**	0.412593E+01
Background Type	Shifted Chebyschev	**LX (Refined)**	0.150815E-01
Background Terms	20	**LY (Refined)**	0.213709E+02
Background Refined?	YES	**SHFT (Refined)**	0.520400E+00
Profile Damping	0	**Non-Refined Parameters (Set to Default Values)**	GU, GP, S/L, H/L, TRNS, STEC, PTEC, SFEC, L11, L22, L33, L12, L13, L23, X, F

Table A.18: GSAS Refinements for Initial Rietveld Fit (100 K) of CRYO-F Variable Temperature Data (Silicon)

# of Cycles	30	**Phase Fraction $YbZrF_7$**	1.000
Unit Cell	Refined	**Phase Fraction Si**	0.43876
Data Limits (2θ)	5.000 – 23.491	**GW (Refined)**	0.320161E+01
Background Type	Shifted Chebyschev	**GV (Refined)**	0.136305E+01
Background Terms	20	**SHFT (Refined)**	0.761358E+00
Background Refined?	YES	**LX (Refined)**	0.675399E+00
Profile Damping	0	**Non-Refined Parameters (Set to Default Values)**	LY GU, GP, S/L, H/L, TRNS, STEC, PTEC, SFEC, L11, L22, L33, L12, L13, L23, X, F

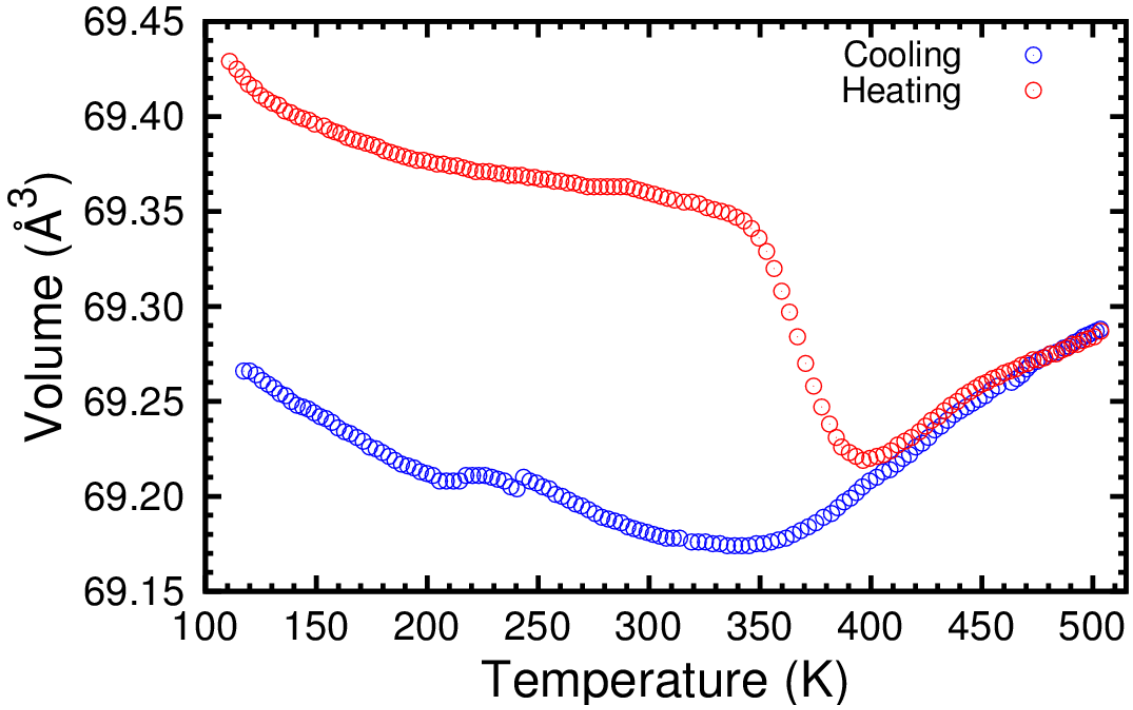

Figure A.14: Temperature calibrated CRYO-C_1 heating and cooling curves are displayed for $YbZrF_7$.

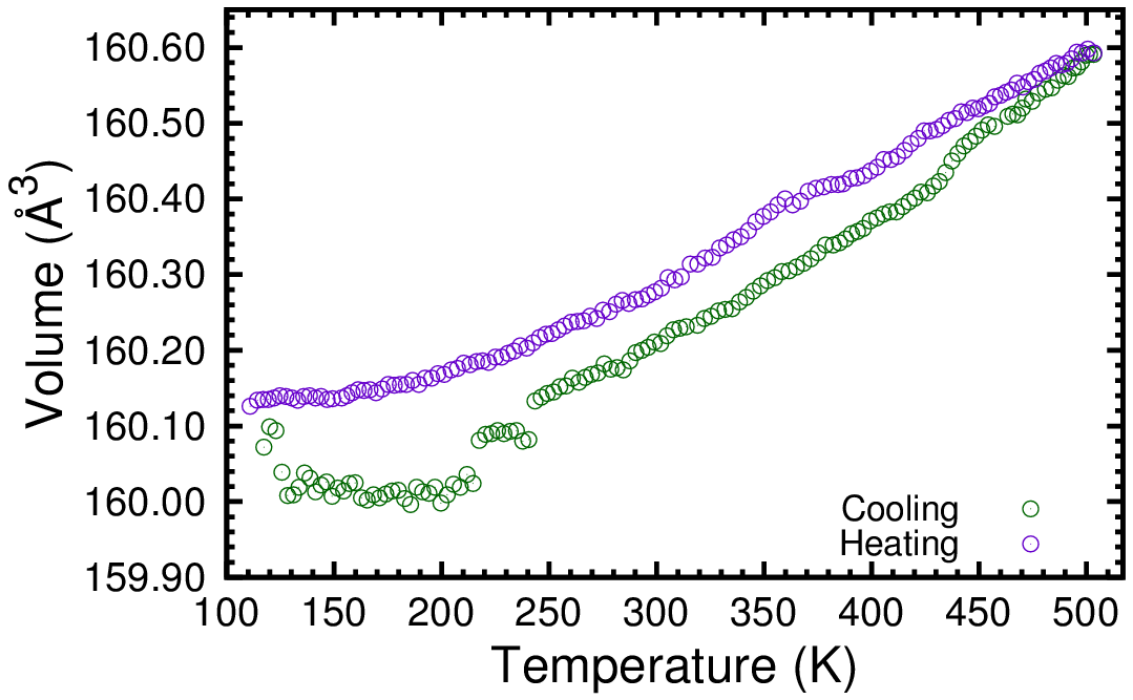

Figure A.15: Temperature calibrated CRYO-C_1 heating and cooling curves are displayed for silicon.

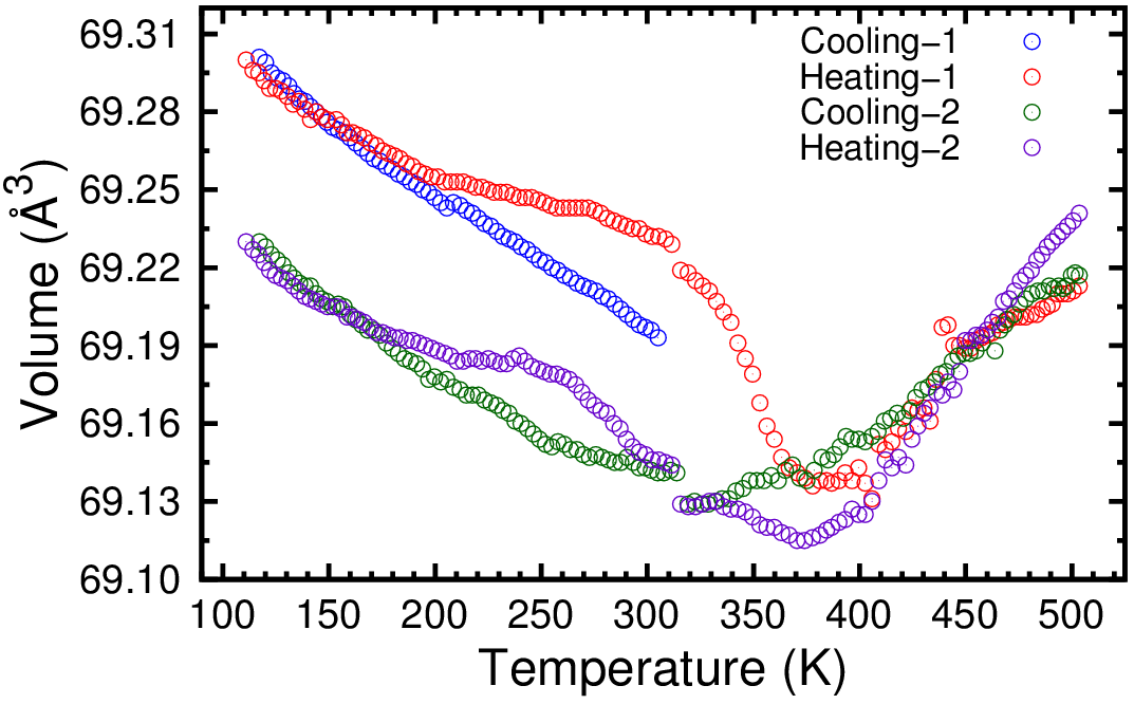

Figure A.16: Temperature calibrated CRYO-C_2 heating and cooling curves are displayed for $YbZrF_7$.

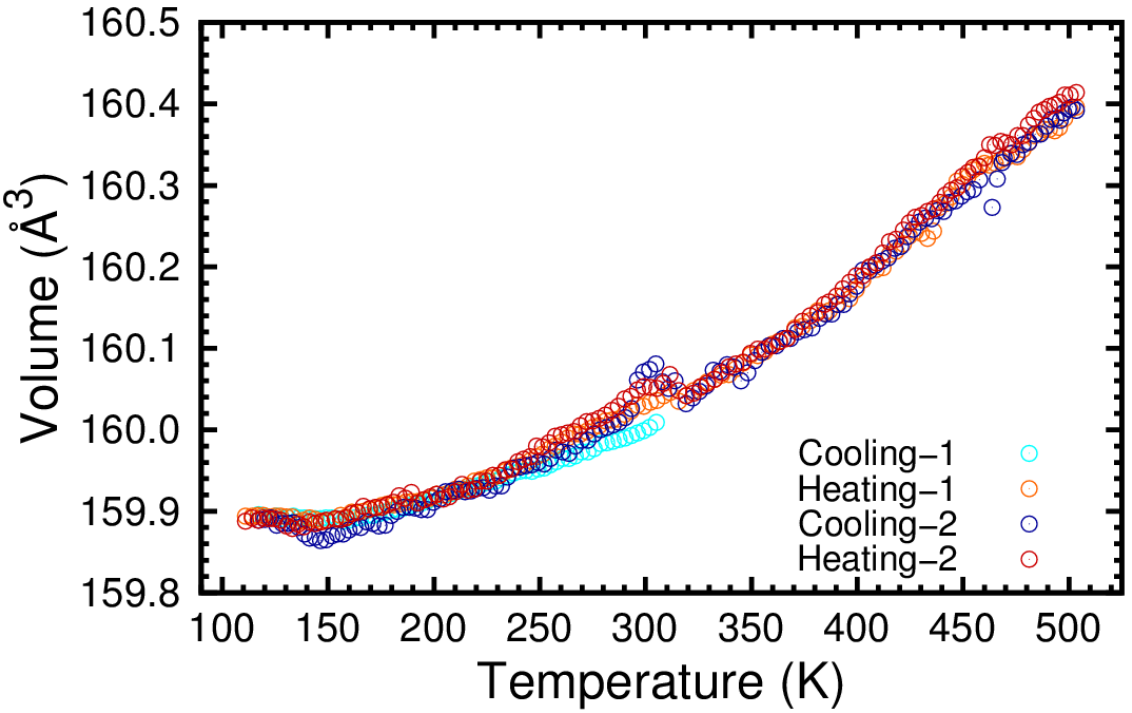

Figure A.17: Temperature calibrated CRYO-C_2 heating and cooling curves are displayed for silicon.

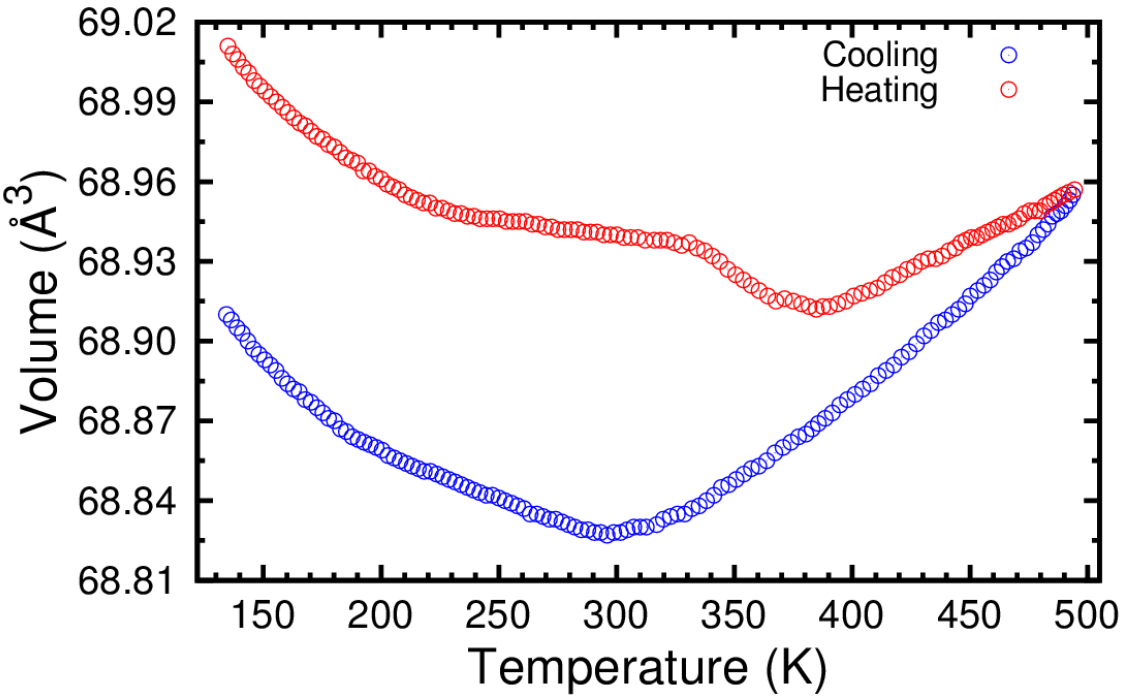

Figure A.18: Temperature calibrated CRYO-F heating and cooling curves are displayed for $YbZrF_7$.

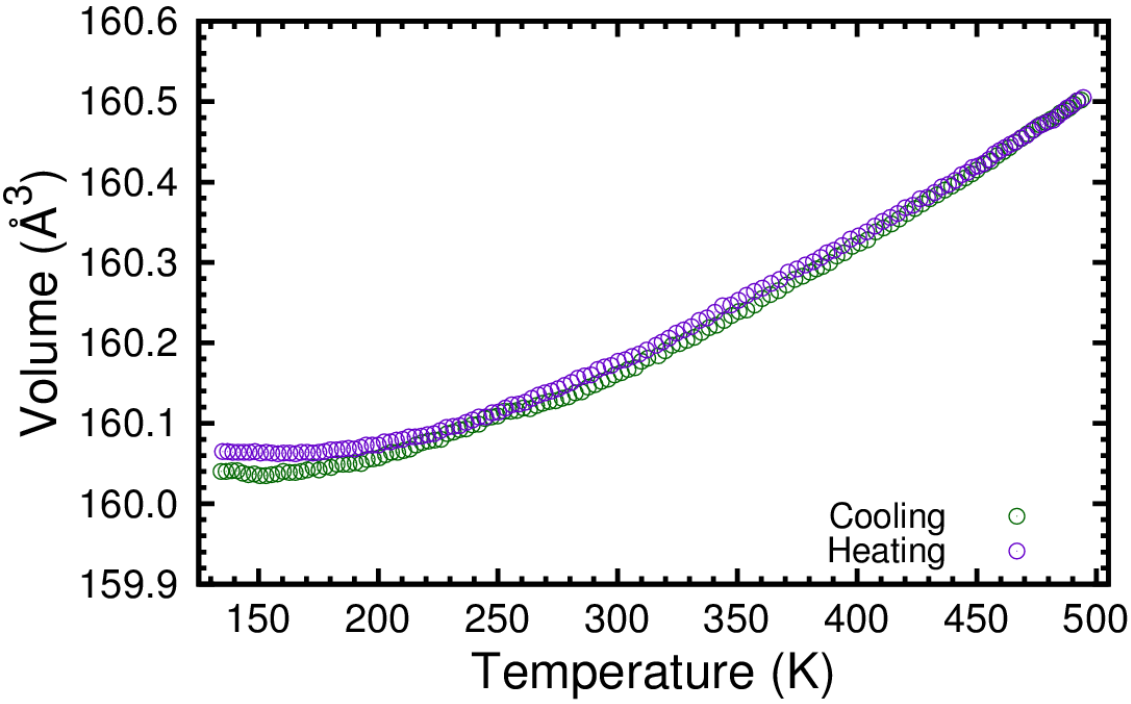

Figure A.19: Temperature calibrated CRYO-F heating and cooling curves are displayed for silicon.

Table A.19: GSAS Refinements for Initial Fit (0 GPa) of Variable Pressure Data ($YbZrF_7$)

# of Cycles	30	**Scale Factor (Refined)**	8.4678
Unit Cell	Refined	**GV (Refined)**	-0.344072E+02
Data Limits (2θ)	8.000 – 32.000	**GW (Refined)**	0.106137E+02
Background Type	Shifted Chebyschev	**LX (Refined)**	0.178422E+01
Background Terms	20	**LY (Refined)**	0.169338E+02
Background Refined?	YES	**SHFT (Refined)**	-0.629831E+00
Profile Damping	0	**Non-Refined Parameters (Set to Default Values)**	GU, GP, S/L, H/L, TRNS, STEC, PTEC, SFEC, L11, L22, L33, L12, L13, L23, X, F

Table A.20: GSAS Refinements for Initial Fit (0 GPa) of Variable Pressure Data (NaCl)

# of Cycles	30	**Phase Fraction $YbZrF_7$**	2.9137
Unit Cell	Refined	**Phase Fraction Si**	1.0000
Data Limits (2θ)	5.000 – 23.491	**GW (Refined)**	0.573469E+01
Background Type	Shifted Chebyschev	**LY (Refined)**	0.276842E+02
Background Terms	20	**SHFT (Refined)**	0.846375E+00
Background Refined?	YES	**Non-Refined Parameters (Set to Default Values)**	GV, GU, GP, S/L, H/L, TRNS, STEC, PTEC, SFEC, L11, L22, L33, L12, L13, L23, X, F
Profile Damping	0		

Table A.21: Modifications to Fitting Parameters for Each Sequential GSAS of Variable Pressure Data ($YbZrF_7$ and NaCl)

Sequential GSAS #	Modifications
1	None – all from initial fit
2	Background fit to a new function graphically (unrefined)
3	Background fit to a new function graphically (unrefined), GU ($YbZrF_7$) returned to default value

APPENDIX-B

COPYRIGHT PERMISSION

1. *Usage of Figure 1.4 from Chapter 1*

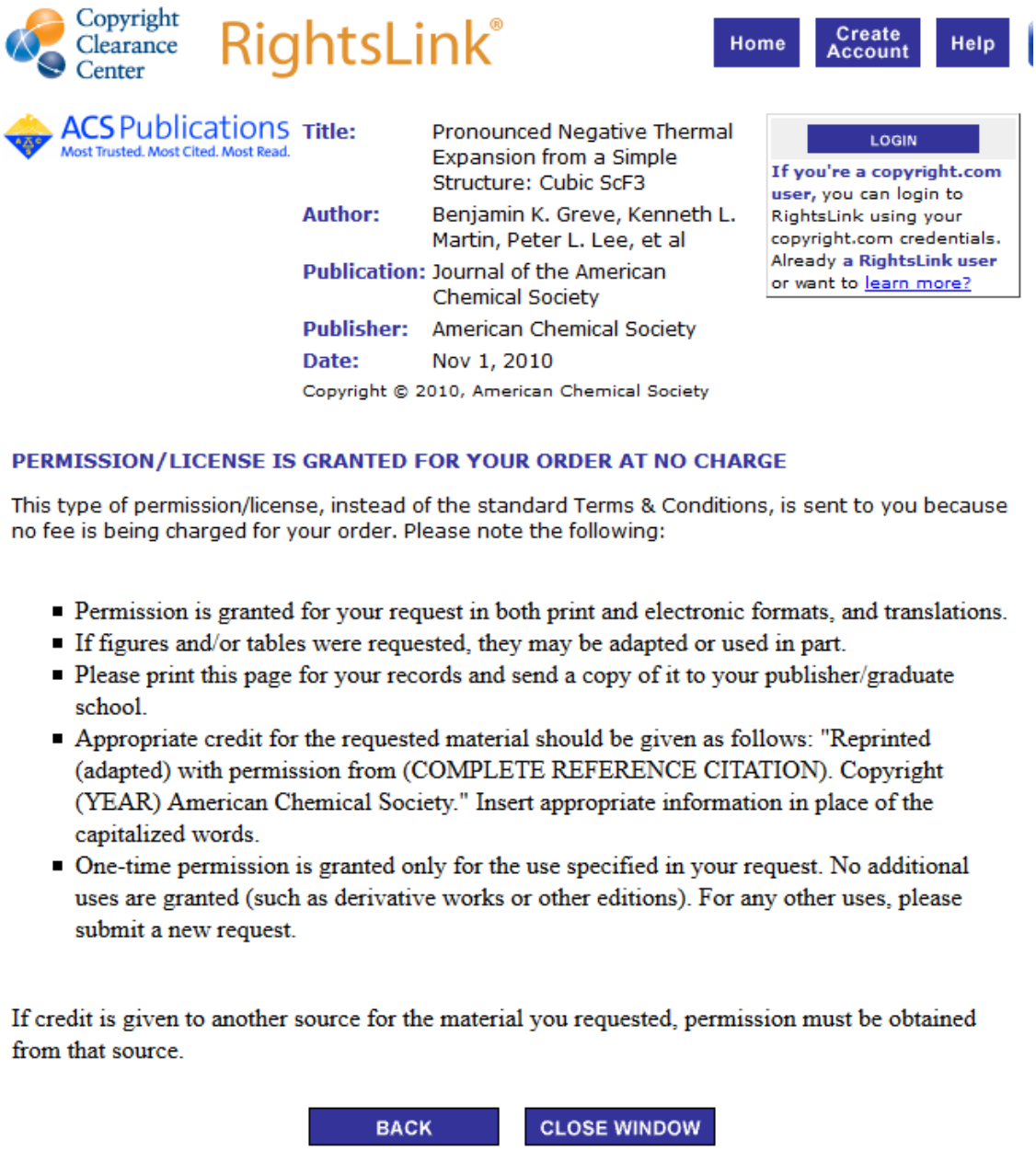

Copyright Clearance Center RightsLink®

Home | Create Account | Help

ACS Publications
Most Trusted. Most Cited. Most Read.

Title: Pronounced Negative Thermal Expansion from a Simple Structure: Cubic ScF3

Author: Benjamin K. Greve, Kenneth L. Martin, Peter L. Lee, et al

Publication: Journal of the American Chemical Society

Publisher: American Chemical Society

Date: Nov 1, 2010

Copyright © 2010, American Chemical Society

LOGIN

If you're a copyright.com user, you can login to RightsLink using your copyright.com credentials. Already **a RightsLink user** or want to learn more?

PERMISSION/LICENSE IS GRANTED FOR YOUR ORDER AT NO CHARGE

This type of permission/license, instead of the standard Terms & Conditions, is sent to you because no fee is being charged for your order. Please note the following:

- Permission is granted for your request in both print and electronic formats, and translations.
- If figures and/or tables were requested, they may be adapted or used in part.
- Please print this page for your records and send a copy of it to your publisher/graduate school.
- Appropriate credit for the requested material should be given as follows: "Reprinted (adapted) with permission from (COMPLETE REFERENCE CITATION). Copyright (YEAR) American Chemical Society." Insert appropriate information in place of the capitalized words.
- One-time permission is granted only for the use specified in your request. No additional uses are granted (such as derivative works or other editions). For any other uses, please submit a new request.

If credit is given to another source for the material you requested, permission must be obtained from that source.

BACK | CLOSE WINDOW

Copyright © 2017 Copyright Clearance Center, Inc. All Rights Reserved. Privacy statement. Terms and Conditions.
Comments? We would like to hear from you. E-mail us at customercare@copyright.com

2. *Usage of Figure 4.1 from Chapter 4*

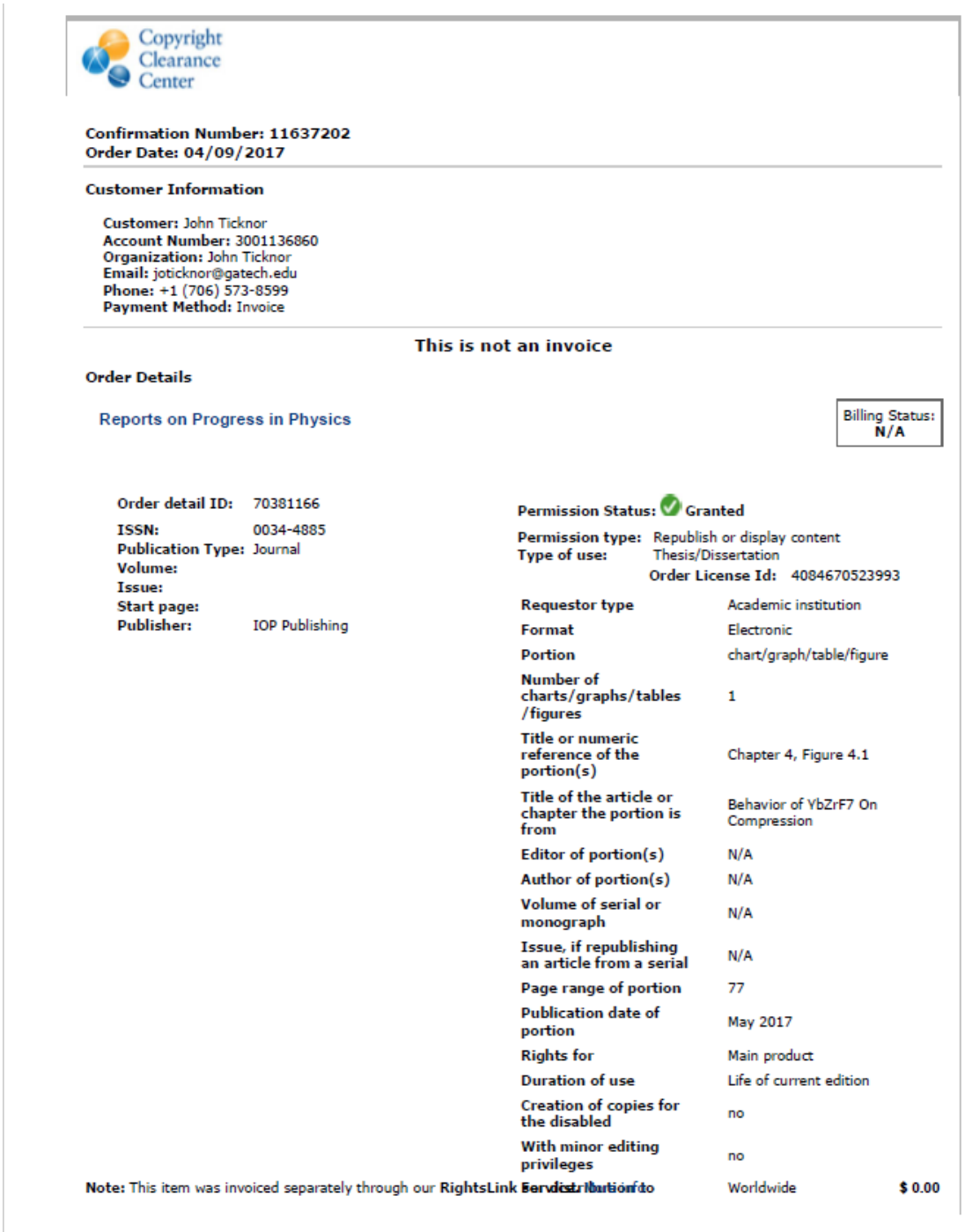

Copyright Clearance Center

Confirmation Number: 11637202
Order Date: 04/09/2017

Customer Information

Customer: John Ticknor
Account Number: 3001136860
Organization: John Ticknor
Email: joticknor@gatech.edu
Phone: +1 (706) 573-8599
Payment Method: Invoice

This is not an invoice

Order Details

Reports on Progress in Physics

Billing Status: **N/A**

Order detail ID: 70381166
ISSN: 0034-4885
Publication Type: Journal
Volume:
Issue:
Start page:
Publisher: IOP Publishing

Permission Status: Granted
Permission type: Republish or display content
Type of use: Thesis/Dissertation
Order License Id: 4084670523993

Requestor type	Academic institution
Format	Electronic
Portion	chart/graph/table/figure
Number of charts/graphs/tables /figures	1
Title or numeric reference of the portion(s)	Chapter 4, Figure 4.1
Title of the article or chapter the portion is from	Behavior of YbZrF7 On Compression
Editor of portion(s)	N/A
Author of portion(s)	N/A
Volume of serial or monograph	N/A
Issue, if republishing an article from a serial	N/A
Page range of portion	77
Publication date of portion	May 2017
Rights for	Main product
Duration of use	Life of current edition
Creation of copies for the disabled	no
With minor editing privileges	no
Distribution	Worldwide

Note: This item was invoiced separately through our RightsLink service. More info **$ 0.00**

REFERENCES

1. Ho, C. Y.; Taylor, R. E., *Thermal Expansion of Solids*. 1st ed.; ASM International: Materials Park, OH, 1998.

2. Xu, G.; Deng, P.; Wang, G. X.; Cao, L. F.; Liu, F., Measurement of Expansion Coefficients of Four Steel Types. *Ironmaking & Steelmaking* **2013,** *40* (8), 613-618.

3. Pucillo, G. P., Thermal Buckling and Post-Buckling Behaviour of Continuous Welded Rail Track. *Vehicle System Dynamics* **2016,** *54* (12), 1785-1807.

4. Hua, X. G.; Ni, Y. Q.; Ko, J. M.; Wong, K. Y., Assessment of Bridge Expansion Joints Using Long-Term Displacement and Temperature Measurement. *Journal of Performance of Constructed Facilities* **2007,** *21* (2), 143-151.

5. Mamdouh, M. E.; Amin, G., Temperature Variations in Concrete Bridges. *Journal of Structural Engineering* **1983,** *109* (10), 2355-2374

6. Schneider, G. A.; Petzow, G., *Thermal Shock and Thermal Fatigue Behavior of Advanced Ceramics*. Springer-Science Business Media, B.V.: Munich, Germany, 1992.

7. Lamon, J.; Pherson, D., Thermal Stress Failure of Ceramics under Repeated Rapid Heatings. *Journal of the American Ceramic Society* **1991,** *74* (6), 1188-1196.

8. Marsden, B. J.; Haverty, M.; Bodel, W.; Hall, G. N.; Jones, A. N.; Mummery, P. M.; Treifi, M., Dimensional Change, Irradiation Creep and Thermal/Mechanical Property Changes in Nuclear Graphite. *International Materials Reviews* **2016,** *61* (3), 155-182.

9. Wynne, R.; Daneu, J. L.; Fan, T. Y., Thermal Coefficients of the Expansion and Refractive Index in YAG. *Appl. Opt.* **1999,** *38* (15), 3282-3284.

10. Chen, P. C.; Romeo, R. C., Ultra Lightweight Precision Optics Technology. In *Optical Design, Materials, Fabrication, and Maintenance*, Dierickx, P., Ed. Spie-Int Soc Optical Engineering: Bellingham, 2000; Vol. 4003, pp 396-405.

11. Ozaki, T.; Ikeda, C.; Isoda, M.; Tsuneta, S., *A New High Thermal-Conductivity Composite Material for High-Precision Space Optics*. Spie - Int Soc Optical Engineering: Bellingham, 1996; Vol. 2804, p 22-31.

12. Hassan, I., Thermal Expansion of Cancrinite. *Mineral. Mag.* **1996,** *60* (403), 949-956.

13. Hovis, G. L.; Medford, A.; Conlon, M.; Tether, A.; Romanoski, A., Principles of Thermal Expansion in the Feldspar System. *American Mineralogist* **2010,** *95* (7), 1060-1068.

14. Jackson, J. M.; Palko, J. W.; Andrault, D.; Sinogeikin, S. V.; Lakshtanov, D. L.; Wang, J. Y.; Bass, J. D.; Zha, C. S., Thermal Expansion of Natural Orthoenstatite to 1473 K. *European Journal of Mineralogy* **2003,** *15* (3), 469-473.

15. Rios, J. L. J.; Rabin, Y., Thermal Expansion of Blood Vessels in Low Cryogenic Temperatures Part I: A New Experimental Device. *Cryobiology* **2006,** *52* (2), 269-283.

16. Hannay, N. B.; Smyth, C. P., The Dipole Moment of Hydrogen Fluoride and the Ionic Character of Bonds. *Journal of the American Chemical Society* **1946,** *68* (2), 171-173.

17. *Jmol: An Open-Source Java Viewer for Chemical Structures in 3D. http://www.jmol.org/*

18. Weller, M.; Overton, T.; Rourke, J.; Armstrong, F., *Inorganic Chemistry*. 6th ed.; Oxford University Press: Oxford, United Kingdom, 2014.

19. McQuarrie, D. A., *Quantum Chemistry*. 2nd ed.; University Science Books: Mill Valley, CA, 2008.

20. Atkins, P.; Paula, J., *Atkins' Physical Chemistry*. 10th ed.; Oxford University Press: Oxford, United Kingdom, 2014.

21. Mortimer, R. G., *Physical Chemistry*. 3rd ed.; Elsevier Academic Press: Burlington, MA, 2008.

22. Slack, G. A.; Bartram, S. F., Thermal Expansion of Some Diamondlike Crystals. *Journal of Applied Physics* **1975,** *46* (1), 89-98.

23. *CRC Handbook of Chemistry and Physics*. 94 ed.; CRC Press: Boca Raton, FL, 2013.

24. Becker, K., Die Kristallstruktur und der Lineare Wärmeausdehnungskoeffizient der Wolframcarbide. *Zeitschrift für Physik* **1928,** *51*, 481.

25. *Ullmann's Polymers and Plastics: Products and Processes*. Wiley-VCH: Weinheim, Germany, 2016; Vol. 1.

26. Mallamace, F.; Corsaro, C.; Mallamace, D.; Vasi, S.; Vasi, C.; Stanley, H. E., Thermodynamic Properties of Bulk and Confined Water. *Journal of Chemical Physics* **2014,** *141* (18).

27. Morelock, C. R. Thermal Expansion, Compressability, and Local Structure of Fluorides and Oxyfluorides With the Rhenium Trioxide Structure. Georgia Institute of Technology, Georgia Institute of Technology, 2014.

28. Sumithra, S.; Umarji, A. M., Negative Thermal Expansion in Rare Earth Molybdates. *Solid State Sciences* **2006,** *8* (12), 1453-1458.

29. Lind, C., Two Decades of Negative Thermal Expansion Research: Where Do We Stand? *Materials* **2012,** *5* (6), 1125.

30. Bekkedahl, N., Volume Dilatometry. *J Res Natl Bur Stand* **1949,** *43* (2), 145-56.

31. Naofumi, Y.; Remi, A.; Masahiro, O., A Calibration Method for Measuring Thermal Expansions With a Push-Rod Dilatometer. *Measurement Science and Technology* **2001,** *12* (12), 2121.

32. Beaucage, T.; da Cunha, M. P.; Matthews, L., Optical Differential Dilatometry for the Determination of the Coefficients of Thermal Expansion of Single Crystal Solids. In *2006 IEEE Ultrasonics Symposium, Vols 1-5, Proceedings*, 2006; pp 788-+.

33. Raether, F.; Springer, R.; Beyer, S., Optical Dilatometry for the Control of Microstructure Development During Sintering. *Material Research Innovations* **2001,** *4* (4), 245-250.

34. Fitzpatrick, M. E.; Hutchings, M. T.; Withers, P. J., Separation of Macroscopic, Elastic Mismatch and Thermal Expansion Misfit Stresses in Metal Matrix Composite Quenched Plates from Neutron Diffraction Measurements. *Acta Materialia* **1997,** *45* (12), 4867-4876.

35. Pathak, P. D.; Vasavada, N. G., Thermal Expansion of NaCl, KCl and CsBr by X-Ray Diffraction and the Law of Corresponding States. *Acta Crystallographica Section A* **1970,** *26* (6), 655-658.

36. Patnode, W.; Scheiber, W. J., The Density, Thermal Expansion, Vapor Pressure, and Refractive Index of Styrene, and the Density and Thermal Expansion of Polystyrene. *Journal of the American Chemical Society* **1939,** *61* (12), 3449-3451.

37. White, G. K., Thermal Expansion of Reference Materials: Copper, Silica and Silicon. *Journal of Physics D: Applied Physics* **1973,** *6* (17), 2070.

38. Sleight, A. W., Negative Thermal Expansion Materials. *Current Opinion in Solid State & Materials Science* **1998,** *3* (2), 128-131.

39. Stepanov, I. A., Compression of Substances with Negative Thermal Expansion. *Materials Letters* **2015,** *161*, 365-367.

40. Xie, Y. M.; Yang, X.; Shen, J.; Yan, X.; Ghaedizadeh, A.; Rong, J.; Huang, X.; Zhou, S., Designing Orthotropic Materials for Negative or Zero Compressibility. *International Journal of Solids and Structures* **2014,** *51* (23–24), 4038-4051.

41. Takenaka, K., Negative Thermal Expansion Materials: Technological Key for Control of Thermal Expansion. *Science and Technology of Advanced Materials* **2012,** *13* (1), 013001.

42. Arvanitidis, J.; Papagelis, K.; Margadonna, S.; Prassides, K.; Fitch, A. N., Temperature-Induced Valence Transition and Associated Lattice Collapse in Samarium Fulleride. *Nature* **2003,** *425* (6958), 599-602.

43. Yamada, I.; Etani, H.; Murakami, M.; Hayashi, N.; Kawakami, T.; Mizumaki, M.; Ueda, S.; Abe, H.; Liss, K. D.; Studer, A. J.; Ozaki, T.; Mori, S.; Takahashi, R.; Irifune, T., Charge-Order Melting in Charge-Disproportionated Perovskite CeCu3Fe4O12. *Inorganic Chemistry* **2014,** *53* (21), 11794-11801.

44. Yamada, I.; Marukawa, S.; Murakami, M.; Mori, S., "True" Negative Thermal Expansion in Mn-Doped LaCu3Fe4O12 Perovskite Oxides. *Applied Physics Letters* **2014,** *105* (23).

45. Yamada, I.; Shiro, K.; Oka, K.; Azuma, M.; Irifune, T., Direct Observation of Negative Thermal Expansion in SrCu3Fe4O12. *Journal of the Ceramic Society of Japan* **2013,** *121* (1418), 912-914.

46. Ibarra, M. R.; Algarabel, P. A.; Marquina, C.; Blasco, J.; García, J., Large Magnetovolume Effect in Yttrium Doped La-Ca-Mn-O Perovskite. *Physical Review Letters* **1995,** *75* (19), 3541-3544.

47. Takenaka, K.; Ichigo, M.; Hamada, T.; Ozawa, A.; Shibayama, T.; Inagaki, T.; Asano, K., Magnetovolume Effects in Manganese Nitrides with Antiperovskite Structure. *Science and Technology of Advanced Materials* **2014,** *15* (1), 015009.

48. Martin, N.; Deutsch, M.; Itié, J. P.; Rueff, J. P.; Rössler, U. K.; Koepernik, K.; Fomicheva, L. N.; Tsvyashchenko, A. V.; Mirebeau, I., Magnetovolume Effect, Macroscopic Hysteresis, and Moment Collapse in the Paramagnetic State of Cubic MnGe Under Pressure. *Physical Review B* **2016,** *93* (21), 214404.

49. Barrera, G. D.; Bruno, J. A. O.; Barron, T. H. K.; Allan, N. L., Negative Thermal Expansion. *Journal of Physics: Condensed Matter* **2005,** *17* (4), R217.

50. Grima, J. N.; Farrugia, P. S.; Gatt, R.; Zammit, V., A System with Adjustable Positive or Negative Thermal Expansion. *Proceedings of the Royal Society a-Mathematical Physical and Engineering Sciences* **2007,** *463* (2082), 1585-1596.

51. Chen, J.; Gao, Q.; Sanson, A.; Jiang, X.; Huang, Q.; Carnera, A.; Rodriguez, C. G.; Olivi, L.; Wang, L.; Hu, L.; Lin, K.; Ren, Y.; Lin, Z.; Wang, C.; Gu, L.; Deng, J.;

Attfield, J. P.; Xing, X., Tunable Thermal Expansion in Framework Materials Through Redox Intercalation. *Nature Communications* **2017,** *8*, 14441.

52. Chen, J.; Hu, L.; Deng, J.; Xing, X., Negative Thermal Expansion in Functional Materials: Controllable Thermal Expansion by Chemical Modifications. *Chemical Society Reviews* **2015,** *44* (11), 3522-3567.

53. Shan, X. R.; Huang, R. J.; Han, Y. M.; Huang, C. J.; Liu, X. P.; Lu, Z. G.; Li, L. F., La(Fe, Si, Co) (13)/Cu Conductive Composites with Tailoring Thermal Expansion. *Journal of Alloys and Compounds* **2016,** *662*, 505-509.

54. Jorgensen, J. E.; Jorgensen, J. D.; Batlogg, B.; Remeika, J. P.; Axe, J. D., Order Parameter and Critical Exponent for the Pressure-Induced Phase Transitions in ReO3. *Physical Review B* **1986,** *33* (7), 4793-4798.

55. Jorgensen, J. E.; Staun Olsen, J.; Gerward, L., Phase Transitions in ReO3 Studied by High-Pressure X-Ray Diffraction. *Journal of Applied Crystallography* **2000,** *33* (2), 279-284.

56. Putz, H.; Brandenburg, K. *Diamond - Crystal and Molecular Structure Visualization*, Bonn, Germany.

57. Greve, B. K.; Martin, K. L.; Lee, P. L.; Chupas, P. J.; Chapman, K. W.; Wilkinson, A. P., Pronounced Negative Thermal Expansion from a Simple Structure: Cubic ScF3. *Journal of the American Chemical Society* **2010,** *132* (44), 15496-15498.

58. Chatterji, T.; Hansen, T. C.; Brunelli, M.; Henry, P. F., Negative Thermal Expansion of ReO3 in the Extended Temperature Range. *Applied Physics Letters* **2009,** *94* (24), 241902.

59. Chatterji, T.; Zbiri, M.; Hansen, T. C., Negative Thermal Expansion in ZnF2. *Applied Physics Letters* **2011,** *98* (18), 181911.

60. Ding, P.; Liang, E. J.; Yu, J.; Du, Z. Y., Electronic Structure, Bonding and Phonon Modes in the Negative Thermal Expansion Materials of Cd(CN) 2 and Zn(CN) 2. *Journal of Physics: Condensed Matter* **2008,** *20* (27), 275224.

61. Hancock, J. C.; Chapman, K. W.; Halder, G. J.; Morelock, C. R.; Kaplan, B. S.; Gallington, L. C.; Bongiorno, A.; Han, C.; Zhou, S.; Wilkinson, A. P., Large Negative Thermal Expansion and Anomalous Behavior on Compression in Cubic ReO3-Type AIIBIVF6: CaZrF6 and CaHfF6. *Chemistry of Materials* **2015,** *27* (11), 3912-3918.

62. Hester, B. R.; Hancock, J. C.; Lapidus, S. H.; Wilkinson, A. P., Composition, Response to Pressure, and Negative Thermal Expansion in MIIBIVF6 (M = Ca, Mg; B = Zr, Nb). *Chemistry of Materials* **2017,** *29* (2), 823-831.

63. Wang, T.; Xu, J.; Hu, L.; Wang, W.; Huang, R.; Han, F.; Pan, Z.; Deng, J.; Ren, Y.; Li, L.; Chen, J.; Xing, X., Tunable Thermal Expansion and Magnetism in Zr-Doped ScF3. *Applied Physics Letters* **2016,** *109* (18), 181901.

64. Morelock, C. R.; Greve, B. K.; Cetinkol, M.; Chapman, K. W.; Chupas, P. J.; Wilkinson, A. P., Role of Anion Site Disorder in the Near Zero Thermal Expansion of Tantalum Oxyfluoride. *Chemistry of Materials* **2013,** *25* (9), 1900-1904.

65. Wilkinson, A. P.; Josefsberg, R. E.; Gallington, L. C.; Morelock, C. R.; Monaco, C. M., History-Dependent Thermal Expansion in NbO2F. *Journal of Solid State Chemistry* **2014,** *213*, 38-42.

66. Laval, J. P.; Abaouz, A., Crystal Chemistry of Anion-Excess ReO3-Related Phases. *Journal of Solid State Chemistry* **1992,** *100* (1), 90-100.

67. Laval, J. P., Crystal Chemistry of Anion-Excess ReO3-Related Phases. III.(1) Gamma-ZrF4, a High-Pressure form of Zirconium Tetrafluoride, and a Comparison of MX4 Structure Types. *Acta Crystallographica Section C-Structural Chemistry* **2014,** *70*, 742-U44.

68. Nazabal, V.; Poulain, M.; Olivier, M.; Pirasteh, P.; Camy, P.; Doualan, J. L.; Guy, S.; Djouama, T.; Boutarfaia, A.; Adam, J. L., Fluoride and Oxyfluoride Glasses for Optical Applications. *Journal of Fluorine Chemistry* **2012,** *134*, 18-23.

69. MacFarlane, D. R.; Newman, P. J.; Voelkel, A., Methods of Purification of Zirconium Tetrafluoride for Fluorozirconate Glass. *Journal of the American Ceramic Society* **2002,** *85* (6), 1610-1612.

70. Poulain, M.; Lucas, J., Rare-Earth Fluorozirconates LnZrF7. *Materials Research Bulletin* **1972,** *7* (4), 319-&.

71. Graudejus, O.; Schrötter, F.; Müller, B. G.; Hoppe, R., Zur Kristallstruktur von SmZrF7 mit einem Anhang über EuSnF7 und YSnF7. *Zeitschrift für anorganische und allgemeine Chemie* **1994,** *620* (5), 827-832.

72. Poulain, M.; Tofield, B. C., The Structure of Cubic YbZrF7. *Journal of Solid State Chemistry* **1981,** *39* (3), 314-328.

73. Sobolev, B. P., *The Rare Earth Trifluorides*. Institut d'Estudis Catalans: Barcelona, Spain, 2000.

74. Poulain, M.; Poulain, M.; Lucas, J., Structure Cristalline de SmZrF7. Relations Structurales avec le Type ReO3. *Journal of Solid State Chemistry* **1973,** *8* (2), 132-141.

75. Manhique, A. Optimisation of Alkali-Fusion Process from Zircon Sands: A Kinetic Study of the Process. University of Pretoria, Pretoria, 2003.

76. Tyagi, N.; Ghanti, E.; Gupta, N.; Lalla, N. P.; Nagarajan, R., Synthesis of Nanocrystalline Mixed Metal Fluorides in Non-Aqueous Medium. *Bulletin of Materials Science* **2009,** *32* (6), 583-587.

77. Kasturi, S.; Sivakumar, V.; Jeon, D. Y., Europium-Activated Rare Earth Fluoride (LnF(3):Eu3+-Ln=La, Gd) Nanocrystals Prepared by Using Ionic Liquid/NH4F as a Fluorine Source via Hydrothermal Synthesis. *Luminescence* **2016,** *31* (5), 1138-1145.

78. Wang, X.; Zhuang, J.; Peng, Q.; Li, Y., Hydrothermal Synthesis of Rare-Earth Fluoride Nanocrystals. *Inorganic Chemistry* **2006,** *45* (17), 6661-6665.

79. Wanklyn, B. M., The Flux Growth of Crystals of Some Fluorides (AlF3, CrF3, NiF2, KNiF3, CoF2 and KCoF3). *Journal of Crystal Growth* **1969,** *5* (4), 279-283.

80. Kemnitz, E.; Wuttke, S.; Coman, S. M., Tailor-Made MgF2-Based Catalysts by Sol-Gel Synthesis. *European Journal of Inorganic Chemistry* **2011,** (31), 4773-4794.

81. Riman, R. E.; Dejneka, M.; Eamsiri, J.; Snitzer, E.; Mailhot, A.; Leaustic, A., Synthesis of Halide Glasses by Reactive Processing of Sol-gel Materials. *Journal of Sol-Gel Science and Technology* **1994,** *2* (1), 849-853.

82. Lepoutre, S.; Boyer, D.; Potdevin, A.; Dubois, M.; Briois, V.; Mahiou, R., Structural Investigations of Sol–gel-derived LiYF4 and LiGdF4 Powders. *Journal of Solid State Chemistry* **2007,** *180* (11), 3049-3057.

83. Glusker, J. P.; Trueblood, K. N., *Crystal Structure Analysis*. 2nd ed.; Oxford University Press: New York, NY, 1985.

84. Smart, L. E.; Moore, E. A., *Solid State Chemistry: An Introduction*. 4th ed.; CRC Press: Boca Raton, FL, 2012.

85. Stout, G. H.; Jensen, L. H., *X-Ray Structure Determination: A Practical Guide*. 2nd ed.; John Wiley & Sons, Inc.: New York, NY, 1989.

86. Lee, M., *X-Ray Diffraction for Materials Research: From Fundamentals to Applications*. CRC Press: Boca Raton, FL, 2016.

87. Ahtee, M., *Lattice Constants of Some Binary Alkali Halide Solid Solutions*. Suomalainen Tiedeakatemia: 1969.

88. Suryanarayana, C.; Norton, M. G., *X-Ray Diffraction: A Practical Approach*. 1st ed.; Springer Science + Business Media: New York, NY, 1998.

89. Tilley, R. J. D., *Understanding Solids: The Science of Materials*. 2nd ed.; John Wiley & Sons: West Sussex, United Kingdom, 2013.

90. Tilley, R. J. D., *Crystals and Crystal Structures*. 1st ed.; John Wiley & Sons: Chichester, England, 2006.

91. Woolfson, M. M., *An Introduction to X-Ray Crystallography*. 2nd ed.; Cambridge University Press: Cambridge, United Kingdom, 1997.

92. Basinski, Z. S.; Hume-Rothery, W.; Sutton, A. L., The Lattice Expansion of Iron. *Proceedings of the Royal Society of London. Series A. Mathematical and Physical Sciences* **1955,** *229* (1179), 459-467.

93. Fathima, A. L.; Sivananthan, S.; Somasundari, C. V.; Neelakandapillai, N., X-ray Diffraction and Micro Hardness Measurement on KClXBr1-X Single Crystals Doped with ZnO Grown from Aqueous Solution. *Articles of Physics Research* **2012,** *3* (5), 407-410.

94. Hu, L.; Chen, J.; Fan, L.; Ren, Y.; Rong, Y.; Pan, Z.; Deng, J.; Yu, R.; Xing, X., Zero Thermal Expansion and Ferromagnetism in Cubic Sc1–xMxF3 (M = Ga, Fe) over a Wide Temperature Range. *Journal of the American Chemical Society* **2014,** *136* (39), 13566-13569.

95. Liu, L.-g.; Bassett, W. A., Effect of Pressure on the Crystal Structure and the Lattice Parameters of BaO. *Journal of Geophysical Research* **1972,** *77* (26), 4934-4937.

96. Yang, X.; Takeichi, N.; Shida, K.; Tanaka, H.; Kuriyama, N.; Sakai, T., Novel Mg–Zr–A–H (A = Li, Na) Hydrides Synthesized by a High Pressure Technique and their Hydrogen Storage Properties. *Journal of Alloys and Compounds* **2011,** *509* (4), 1211-1216.

97. Inorganic Crystal Structure Database. http://icsd.fiz-karlsruhe.de.

98. Fluck, E., Inorganic Crystal Structure Database (ICSD) and Standardized Data and Crystal Chemical Characterization of Inorganic Structure Types (TYPIX) - Two Tools for Inorganic Chemists and Crystallographers. *Journal of Research of the National Institute of Standards and Technology* **1996,** *101* (3), 217-220.

99. ICDD, P. D. F., International Centre for Diffraction Data. *Powder Diffraction File"(Newtown Square, PA 19073, USA)* **1997**.

100. Filipponi, A.; Borowski, M.; Bowron, D. T.; Ansell, S.; Di Cicco, A.; De Panfilis, S.; Itie, J.-P., An Experimental Station for Advanced Research on Condensed Matter Under Extreme Conditions at the European Synchrotron Radiation Facility-BM29 Beamline. *Review of Scientific Instruments* **2000,** *71* (6), 2422-2432.

101. Mathis, Y. L.; Gasharova, B.; Moss, D., Terahertz Radiation at ANKA, the New Synchrotron Light Source in Karlsruhe. *Journal of Biological Physics* **2003,** *29* (2-3), 313-318.

102. Moncton, D. E., The Advanced Photon Source: Performance and Results from Early Operation. *Journal of Synchrotron Radiation* **1998,** *5*, 155-157.

103. Tavares, P. F.; Leemann, S. C.; Sjostrom, M.; Andersson, A., The MAX IV Storage Ring Project. *Journal of Synchrotron Radiation* **2014,** *21*, 862-877.

104. Chernyshev, V. V., Structure Determination from Powder Diffraction. *Russian Chemical Bulletin* **2001,** *50* (12), 2273-2292.

105. Will, G., *Powder Diffraction: The Rietveld Method and the Two Stage Method to Determine and Refine Crystal Structures from Powder Diffraction Data*. 1st ed.; Springer Science + Business Media: Heidelberg, Germany, 2006.

106. McCusker, L. B.; Von Dreele, R. B.; Cox, D. E.; Louer, D.; Scardi, P., Rietveld Refinement Guidelines. *Journal of Applied Crystallography* **1999,** *32* (1), 36-50.

107. Albinati, A.; Willis, B. T. M., The Rietveld Method in Neutron and X-Ray Powder Diffraction. *Journal of Applied Crystallography* **1982,** *15* (4), 361-374.

108. Bish, D. L.; Howard, S. A., Quantitative Phase Analysis Using the Rietveld Method. *Journal of Applied Crystallography* **1988,** *21* (2), 86-91.

109. Epple, M., Applications of Temperature-Resolved Diffraction Methods in Thermal Analysis. *Journal of Thermal Analysis* **1994,** *42* (2), 559-593.

110. Chierotti, M. R.; Rossin, A.; Gobetto, R.; Peruzzini, M., Interaction Between a Transition-Metal Fluoride and a Transition-Metal Hydride: Water-Mediated Hydrofluoric Acid Evolution Following Fluoride Solvation. *Inorganic Chemistry* **2013,** *52* (21), 12616-12623.

111. Toby, B. H., CMPR–a Powder Diffraction Toolkit. *Journal of Applied Crystallography* **2005,** *38* (6), 1040-1041.

112. Larson, A. C.; Von Dreele, R. B., GSAS. *General Structure Analysis System. LANSCE, MS-H805, Los Alamos, New Mexico* **1994**.

113. Toby, B. H., EXPGUI, a Graphical User Interface for GSAS. *Journal of Applied Crystallography* **2001,** *34* (2), 210-213.

114. Love, C. *ME-70 Inductively Coupled Plasma Atomic Emission Spectroscopy GLI Method Summary*; Knoxville, TN, 2017.

115. Chupas, P. J.; Chapman, K. W.; Kurtz, C.; Hanson, J. C.; Lee, P. L.; Grey, C. P., A Versatile Sample-Environment Cell for Non-Ambient X-Ray Scattering Experiments. *Journal of Applied Crystallography* **2008,** *41* (4), 822-824.

116. Smith, D. Y., Anomalous X-Ray Scattering: Relativistic Effects in X-Ray Dispersion Analysis. *Physical Review A* **1987,** *35* (8), 3381-3387.

117. Toby, B. H.; Von Dreele, R. B., What's New in GSAS-II. *Powder Diffraction* **2014,** *29* (S2), S2-S6.

118. Okada, Y.; Tokumaru, Y., Precise Determination of Lattice Parameter and Thermal Expansion Coefficient of Silicon Between 300 and 1500 K. *Journal of Applied Physics* **1984,** *56* (2), 314-320.

119. Többens, D.; Stüßer, N.; Knorr, K.; Mayer, H.; Lampert, G. In *E9: the New High-Resolution Neutron Powder Diffractometer at the Berlin Neutron Scattering Center*, Materials Science Forum, Trans Tech Publ: 2001; pp 288-293.

120. Bukvetskij, B.; Garashina, L., Crystallochemical Investigation of Rhombic Samarium-, Holmium- and Ytterbium Trifluorides. *Koordinatsionnaya Khimiya* **1977,** *3* (7), 1024-1029.

121. Zachariasen, W., Crystal Chemical Studies of the 5f-Series of Elements. XII. New Compounds Representing Known Structure Types. *Acta Crystallographica* **1949,** *2* (6), 388-390.

122. Hsu, L. S.; Hsu, C. T., Stress-Strain Behavior of Steel-fiber High-Strength Concrete Under Compression. *Structural Journal* **1994,** *91* (4).

123. Sakino, K.; Nakahara, H.; Morino, S.; Nishiyama, I., Behavior of Centrally Loaded Concrete-Filled Steel-Tube Short Columns. *Journal of Structural Engineering* **2004,** *130* (2), 180-188.

124. Wang, Y.-T.; Cai, J.; Long, Y.-L., Hysteretic Behavior of Square CFT Columns with Binding Bars. *Journal of Constructional Steel Research* **2017,** *131*, 162-175.

125. Alexander, T. B.; James, W. H., The Surface of Venus. *Reports on Progress in Physics* **2003,** *66* (10), 1699.

126. Adkins, C. J., *An Introduction to Thermal Physics*. Cambridge University Press: Cambridge, United Kingdom, 1987.

127. Guoyin, S.; Ho Kwang, M., High-Pressure Studies with X-Rays Using Diamond Anvil Cells. *Reports on Progress in Physics* **2017,** *80* (1), 016101.

128. Jayaraman, A., Diamond Anvil Cell and High-Pressure Physical Investigations. *Reviews of Modern Physics* **1983,** *55* (1), 65-108.

129. Birch, F., Equation of State and Thermodynamic Parameters of NaCl to 300 kbar in the High-Temperature Domain. *Journal of Geophysical Research* **1986,** *91* (B5), 4949-4954.

130. Toby, B. H.; Von Dreele, R. B., GSAS-II: the Genesis of a Modern Open-Source all Purpose Crystallography Software Package. *Journal of Applied Crystallography* **2013,** *46* (2), 544-549.

131. Cherginets, V. L.; Baumer, V. N.; Galkin, S. S.; Glushkova, L. V.; Rebrova, T. P.; Shtitelman, Z. V., Solubility of Al2O3 in Some Chloride−Fluoride Melts. *Inorganic Chemistry* **2006,** *45* (18), 7367-7371.

132. Angel, R. J.; Gonzalez-Platas, J.; Alvaro, M., EosFit7c and a Fortran Module (Library) for Equation of State Calculations. *Zeitschrift Fur Kristallographie* **2014,** *229* (5), 405-419.

133. Gonzalez-Platas, J.; Alvaro, M.; Nestola, F.; Angel, R., EosFit7-GUI: a New Graphical User Interface for Equation of State Calculations, Analyses and Teaching. *Journal of Applied Crystallography* **2016,** *49* (4), 1377-1382.

134. Meade, C.; Jeanloz, R., Static Compression of Ca(OH)2 at Room Temperature: Observations of Amorphization and Equation of State Measurements to 10.7 GPa. *Geophysical Research Letters* **1990,** *17* (8), 1157-1160.

135. Birch, F., Finite Elastic Strain of Cubic Crystals. *Physical Review* **1947,** *71* (11), 809-824.

136. Morelock, C. R.; Greve, B. K.; Gallington, L. C.; Chapman, K. W.; Wilkinson, A. P., Negative Thermal Expansion and Compressibility of Sc1–xYxF3 (x≤0.25). *Journal of Applied Physics* **2013,** *114* (21), 213501.

137. Hefang, H.; Mackenzie, J. D., The Effect of Oxide Impurity on the Physical Properties of Fluorozirconate Glass. *Journal of Non-Crystalline Solids* **1986,** *80* (1), 495-502.

138. Zhang, L.; Fan, T.; Wang, P. W., Effect of Oxide Dopant on the Structure of Fluorozirconate Glasses Studied by X-Ray Photoelectron Spectroscopy. *J. Mater. Sci.* **1995,** *30* (6), 1445-1448.

139. Poulain, M., Halide Glasses. *Journal of Non-Crystalline Solids* **1983,** *56* (1), 1-14.

140. Didenko, N. A.; Gaivoronskaya, K. A.; Voit, E. I.; Gerasimenko, A. V.; Kavun, V. Y., Synthesis and Studies of Magnesium Hexafluorozirconates MgZrF6 · nH2O (n = 5, 2, 0). *Russian Journal of Inorganic Chemistry* **2010,** *55* (9), 1339-1346.

141. Sepe, M. P., *Thermal Analysis of Polymers*. Rapra Technology, LTD: 1997; Vol. 8.

142. Duval, C., *Inorganic Thermogravimetric Analysis*. 2nd ed.; Elsevier Publishing Company: New York, NY, 1963.

143. Greenspan, L., Humidity Fixed Points of Binary Saturated Aqueous Solutions. *Journal of research of the national bureau of standards* **1977,** *81* (1), 89-96.

144. Abate, L. J.; Wilhelm, H. A., Sublimation of Zirconium Tetrafluoride. **1951**.

145. Kemnitz, E.; Menz, D.-H., Fluorinated Metal Oxides and Metal Fluorides as Heterogeneous Catalysts. *Progress in Solid State Chemistry* **1998,** *26* (2), 97-153.

146. Tucker, M. G.; Goodwin, A. L.; Dove, M. T.; Keen, D. A.; Wells, S. A.; Evans, J. S. O., Negative Thermal Expansion in ZrW2O8 Mechanisms, Rigid Unit Modes, and Neutron Total Scattering. *Physical Review Letters* **2005,** *95* (25), 255501.

147. Reeder, R. J.; Michel, F. M., Chapter Twenty - Application of Total X-Ray Scattering Methods and Pair Distribution Function Analysis for Study of Structure of Biominerals. In *Methods in Enzymology*, James, J. D. Y., Ed. Academic Press: 2013; Vol. Volume 532, pp 477-500.

148. Dexpert-Ghys, J.; J. L. Ribeiro, S.; Dugat, P.; Avignant, D., Crystal Structures and Luminescence Properties of La3Zr4F25 and [small alpha]-LaZr3F15. *Journal of Materials Chemistry* **1998,** *8* (4), 1043-1050.

149. Martineau, C.; Legein, C.; Body, M.; Péron, O.; Boulard, B.; Fayon, F., Structural Investigation of α-LaZr2F11 by Coupling X-Ray Powder Diffraction, 19F Solid State NMR and DFT Calculations. *Journal of Solid State Chemistry* **2013,** *199*, 326-333.

150. Laval, J. P.; Gervais, J. F.; Fournès, L.; Grannec, J.; Gravereau, P.; Abaouz, A.; Yacoubi, A., Cationic Distribution in α-MZr3F15 Series (M = Y, In, Ln, Tl). *Journal of Solid State Chemistry* **1995,** *118* (2), 389-396.

151. Tofield, B. C.; Poulain, M.; Lucas, J., Non-Stoichiometry in Anion-Excess ReO3 Phases; the Structure of Zr0.8Yb0.2F3.2O0.3(MX3.5) by Powder Neutron Diffraction. *Journal of Solid State Chemistry* **1979,** *27* (2), 163-178.